

DUAL BEAM DETECTION TECHNIQUE TO STUDY MAGNETO-OPTICAL KERR
EFFECT

By

Shankar Chandra Acharya, Msc
A thesis submitted to the Graduate Council of
Texas State University in partial fulfillment
of the requirements for the degree of
Master of Science
with a Major in Physics
May 2019

Committee Members:

Wilhelmus J Geerts, Chair

Nikoleta Theodoropoulou

Alexander Zakhidov

COPYRIGHT

By

Shankar Chandra Acharya

2019

FAIR USE AND AUTHOR'S PERMISSION STATEMENT

Fair Use

This work is protected by the Copyright Laws of the United States (Public Law 94-553, section 107). Consistent with fair use as defined in the Copyright Laws, brief quotations from this material are allowed with proper acknowledgement. Use of this material for financial gain without the author's express written permission is not allowed.

Duplication Permission

As the copyright holder of this work I, Shankar Chandra Acharya, authorize duplication of this work, in whole or in part, for educational or scholarly purposes only.

ACKNOWLEDGEMENTS

First of all, I would like to thank my supervisor Dr. Wilhelmus J Geerts for his constant support and guidance. I feel grateful to have worked under such an inspiring researcher who has given me this opportunity to learn and explore scientific knowledge. I would also like to thank my committee members Dr. Nikoleta Theodoropoulou and Dr. Alexander Zakhidov for their constructive feedback which have contributed to my thesis project. I am grateful for my family and friends for their motivation and encouragement all these years of my studies. My mother and father have supported me during the difficult times and inspired me throughout my research. This material is based upon work supported by, or in part by, the U. S. Army Research Laboratory and the U. S. Army Research Office under contract/grant number W911NF1510394. Hinds Instruments and Thorlabs Inc. have to be thanked for lending us equipment. Nate England of Engineering and Collin Pane of Engineering Technology are thanked for helping with machine shop tasks. Furthermore, I would like to acknowledge travel support of the department of Physics, the College of Science, and the graduate college of Texas State University through the course of my thesis project. This allowed me to present part of the results presented in this thesis at the TSAPS spring-2018 meeting at Tarleton State University in Stephenville and at the 2018 International Conference on Magnetism in San Francisco.

TABLE OF CONTENTS

	Page
ACKNOWLEDGEMENTS	iv
LIST OF TABLES	vii
LIST OF FIGURES	viii
LIST OF SYMBOLS	xiii
CHAPTER	
1. INTRODUCTION	1
1.1 Motivation of the Study	1
1.2 Magneto Optical Kerr Effect	4
1.3 Spin Orbit Interaction	5
1.4 MOKE Geometries	7
1.5 Overview on Single Beam Modulated MOKE and Dual Beam Modulated MOKE	9
1.6 Scope of the Thesis	10
2. MAGNETO OPTICAL KERR THEORY	12
2.1 Polarization of an Electromagnetic Waves	12
2.2 Jones Vectors of Polarized Light and Special Polarizations.....	15
2.3 Jones Matrices.....	18
2.4 MOKE Setup Employing Polarizer and Analyzer	30
2.5 MOKE Setup Employing a PEM	35

2.6 Apparatus for Dual MOKE Measurements.....	44
2.6.1 Polarizer and Analyzer.....	45
2.6.2 Light Source.....	47
2.6.3 Photo-Detectors.....	48
3. DUAL BEAM DETECTOR TECHNIQUE	53
3.1 Optics Alignment of Dual Beam MOKE Setup.....	56
3.2 Multiple Interference Effects in PEM.....	60
3.3 LabVIEW Programing	71
3.4 Implementation of External Triggering	72
3.5 Noise of Laser on the Detectors.....	73
3.6 Test Stability of PEM-100	74
4. EXPERIMENTAL RESULTS AND DISCUSSION	80
4.1 Test as a Function of Analyzer Angle.....	80
4.2 Test as a Function of PEM Tilt Angle	84
4.3 Test as a Function of Retardation	96
5. TEST OF DBM SETUP WITH NICKEL OXIDE AND NICKEL IRON OXIDE SERIES.....	102
6. DISCUSSION OF RESULTS AND FURTHER RESEARCH.....	109
APPENDIX SECTION.....	111
REFERENCES	119

LIST OF TABLES

Table	Page
1 NEP, Transimpedance, Responsivity, noise, signal to noise ratio for active area for different detectors from Thorlabs Inc. under different noise setting of lock ins.	52
2 S/N ratio for different combination of PEM and detector with field and sample as a function of PEM tilt angle.....	94
3 Corresponding θ_k in degrees per Oe. for NiO (film and substrate).	116
4 Corresponding θ_k in degrees per Oe. for NiO (substrate).	116
5 Corresponding θ_k in degrees per Oe. for NiFeO (film and substrate).	117
6 Corresponding θ_k in degrees per Oe. for NiFeO (substrate).	117

LIST OF FIGURES

Figure	Page
1.1 Effect of exchange splitting and spin orbit interaction on the allowed optical transitions [11]	6
1.2 Different MOKE geometries [45].....	8
2.1 Polarization of an ellipse.....	15
2.2 Jones vector of circularly and linearly polarized light.....	18
2.3 Jones matrix mathematics operation.....	19
2.4 Family of polarizing prisms [46]	23
2.5 Photo elastic modulator [HINDS Instruments].....	24
2.6 Simplest form of PEM-90 from HINDS.....	25
2.7 Retardation of PEM [47].....	26
2.8 Multiple interference effect in PEM [43].....	28
2.9 Phasor diagram for S and P component of light in the case of multiple interference effect.....	29
2.10 Experimental set-up used for Kerr Measurement	30
2.11 Polarization Modulation Technique for Kerr Measurement [48]	36
2.12 Polarization Modulation for Kerr Measurement [33]	37
2.13 The single beam detector setup using PEM and Glan-Taylor prism	38
2.14 Bessel functions $J_0(x)$, $J_1(x)$, $J_2(x)$	44

2.15 Glan-Taylor Prism [49].....	46
2.16 Wollaston prism [50]	47
2.17 Detector Responsivity (PDA-55) [Thorlabs]	49
3.1 Dual Beam Detector Magneto Optical Kerr Set-Up.....	55
Figure 3.2 Stages used and Schematic diagram on two detector	
MOKE analyzer detector unit	56
3.3 The DC signals on both channels as a function of analyzer for a P-polarized (top) and an S-polarized (bottom) incident beam	58
3.4 Signal for channel 1, (top) and channel 2, (bottom) as a function of the analyzer angle for PEM tilt 0 and 0.4	60
3.5 Single detector MOKE using PEM.....	61
3.6 LabVIEW automation for Data Acquisition	71
3.7 Step down response of PEM-100, Stepping down from 3.14 to 1.571 wavelength retardation, PEM tilt at 5.5 degrees, and with PDA-55 detector	75
3.8 Step up response of PEM-100, Stepping down from 3.14 to 1.571 wavelength retardation, PEM tilt at 5.5 degrees, and with PDA-55 detector	76
3.9 Step down response of PEM-100, Stepping down from 3.14 to 1.571 wavelength retardation, PEM tilt at 0 degrees, and with PDA-55 detector	77
3.10 Step up response of PEM-100, Stepping down from 3.14 to 1.571 wavelength retardation, PEM tilt at 0 degrees, and with PDA-55 detector	78

4.1 2ω intensity signals and corresponding noises as a function of analyzer angles for PEM-90, PDA-55, and quarter wave retardation.....	81
4.2 DC intensity signals and corresponding noises as a function of analyzer angles for PEM-90, PDA-55, and quarter wave retardation.....	81
4.3 Test as a function of Analyzer with PEM-90, PDA-55 detectors.....	82
4.4 Zoomed in plots of 2ω and dc signals of each channel and their corresponding noises as a function of the analyzer angle.....	84
4.5 Signals as a function of PEM tilt, PEM-90, PDA-55, no glass substrate, no field, and quarter wave retardation	85
4.6 DC signals as a function of PEM tilt, PEM-90, PDA-55, no glass substrate, no field, and quarter wave retardation	87
4.7. DC and 2ω noise correlation of channel 1 as a function of PEM-90 tilt, PDA-55, quarter wavelength retardation, no substrate and field.....	88
4.8 DC and 2ω noise correlation of channel 2 as a function of PEM-90 tilt, PDA-55, quarter wave retardation, no substrate and field.....	88
4.9 The 2ω signals and corresponding noises as a function of PEM-100 tilt angle, NiFeO sample, no field, quarter wave retardation and PDA-100-A2	90
4.10 2ω signals as a function of PEM-100, PDA-100-A2, NiFeO sample, no field, and a quarter wave retardation	91

4.11 Variation of 2ω intensity and corresponding noises as a function PEM tilt, PEM-100, PDA-100-A2, NiFeO sample, and quarter wave retardation	92
4.12 Variation of dc intensity and corresponding noises as a function PEM tilt, PEM-100, PDA-100-A2, NiFeO sample, and quarter wave retardation.....	93
4.13 The MO signals of NiFeO sample as a function of PEM tilt angle using PEM-100, PDA-100-A2, and at quarter wave retardation	95
4.14 Test as a function of retardation on glass slide using PEM-90, PDA-55, and normal incidence of PEM	97
4.15 Noise of individual channel, difference channel and sum channel at positive field as a function of retardation depth, PEM-90, PDA-55, a glass slide and PEM at normal incidence	98
4.16 2ω intensity of each channels at positive and negative field of 3.4KOe and dc noises at positive field as a function of retardation using PEM-90, PDA-55, a glass slide, and at larger PEM tilt of 4.5 degrees.....	99
4.17 The 2ω signals at positive field and the MO signals as a function of the PEM tilt for PEM-90, PDA-55, and at larger PEM tilt of 4.5 degrees	100
4.18 2ω intensity and corresponding noises as a function of retardation depth at positive field, PEM-100, PDA-100-A2, NiFeO sample	101
5.1 Measured 2ω intensity signals for NiO samples for different oxygen flow.....	104

5.2 MOKE in volts for difference channel for different samples of NiO at different oxygen flow during deposition.....	105
5.3 MOKE in volts for difference channel for different samples of NiO at different oxygen flow during deposition	106
5.4 MO data of RF co-sputtered NiO thin films as a function of the oxygen concentration in the sputter gas in percentage measured using the dual beam and single beam methods. Included error bars indicate spread of the measurement results.....	107
5.5 MO data for RF-sputtered NiO as a function of the oxygen flow measured by dual beam method (grey) and measured by single beam method (red) including measurement errors caused by substrate subtraction.....	108

LIST OF SYMBOLS

- ω' : Angular frequency of an electromagnetic light.
- ω : Angular frequency of the Photo-elastic modulator (PEM)
- f : Modulation frequency of the PEM.
- i : Square root of minus one.
- $J_0(x), J_1(x)$, and $J_2(x)$: Bessel functions 1st kind with argument x .
- \emptyset : Phase amplitude.
- δ_0 : Initial phase amplitude of PEM.
- δ_1 : Phase shift if light travels through unstrained PEM.
- δ_{po} : PEM's modulated phase amplitude for P polarized light.
- δ_{so} : PEM's modulated phase amplitude for S polarized light.
- ϕ_p, ϕ_s : Optical path lengths
- t : Time.
- r : Reflection coefficient SiO₂-air interface.
- $r_{pp}, r_{ss}, r_{sp}, r_{ps}$: Sample's Fresnel reflection coefficients for linearly polarized light.
- r_+, r_- : Sample's Fresnel reflection coefficients for circularly polarized light.
- q_{11}, q_{12} : PEM's photo elastic constants.
- σ : Poisson's constant.
- β : Analyzer angle.

θ_k : Polar Kerr rotation.

n_0 : Refraction index.

η_k : Polar Kerr ellipticity.

t' : Transmission coefficient.

1. INTRODUCTION

1.1 Motivation of the Study

The Magneto-Optical (MO) [1] measurement method is often used to study magnetic properties of thin films and multilayers. In traditional vibrating sample magnetometry (VSM) a sample is first magnetized in a uniform magnetic field. It is then sinusoidally vibrated through the use of a piezo-electric transducer or a loudspeaker such that its magnetic stray field induces a flux change in the pickup coils. Because of Faraday's induction law, this results in an induced voltage which is proportional to the sample's magnetic moment. Unlike the traditional VSM measurement method, Magneto-optical Kerr effect (MOKE) is an indirect technique where one measures an optical property that is proportional to the magnetic moment. The sample is placed in between the pole pieces of an electromagnet to be magnetized. Linearly polarized light is passed through the sample or reflected off it before it goes through an analyzer and is detected by a photodiode or photomultiplier. Change in optical properties is then recorded in terms of intensity variations measured with the detector. Although it is an indirect measurement technique, it has various advantages compared to the traditional VSM including a higher sensitivity [2], and being a non-contact method allowing to conveniently measure hysteresis curves remotely through a vacuum window, through a security fence in case of a high voltage transformer, or in a hard disk assembly line not requiring direct contact with the disc reducing contamination issues.

The MO Kerr effect has many applications including [3]:

A. It is used in magneto-optical drives to store information. When a linearly polarized laser beam is directed at a specific point on the magnetic disc, the plane of polarization of the reflected beam is slightly rotated with respect to the plane of polarization of the incident beam. The rotation depends on the direction of the magnetic moment in the disk and can be interpreted by the electronics as a zero or one [4]. Systems have been developed and commercialized to store computer data (MO data), or music (Sony minidisk system).

B. The MO Kerr effect is used to measure the magnetic properties of ferromagnetic materials. MOKE offers information on coercive field and the shape of the magnetic hysteresis curve. Angle dependent oblique MOKE can provide information on the magnetic anisotropy of the sample [5]. Taking into consideration the fact that Rev. John Kerr did not imagine how important magneto-optics would be, it helped bring about new development such as application of optics to study magnetic media. As light is used to probe the magnetic moment, this technique does not require contact, which makes the MO technique as mentioned above for certain applications more attractive than the traditional VSM method. For those applications, a non-contact method is cleaner, easier to implement, and safer.

C. The MO effects are used in optical isolators and modulators.

Faraday and Kerr effects both are referred to as magneto-optical properties [6]. Faraday Effect is when light passes through a transparent material exposed to a strong electromagnetic field, its polarization changes depending on the strength of the field [38].

Magneto-Optical Kerr Effect is a property where light reflects off a strongly magnetized

surface modifying the state of polarization of the light beam [1]. The polarization plane of the reflected light deflects slightly from the incident beam. Also, the ellipticity of the reflected beam differs from the ellipticity of the Magneto-Optical effects are caused by the non-zero off-diagonal components in the dielectric tensor. Ferromagnetic materials with large spin-orbit interactions have normally large MO effects. Since being an optical characterization technique, by studying the change in polarization of the laser light one can get an idea about the dielectric properties of the material. The dielectric properties can be deduced from the electronic band structure and the optical electronic transitions allowed. Two type of transitions need to be considered: (1) intraband electronic transitions between occupied and unoccupied states in a single band; (2) interband transitions between occupied states in the conduction band and unoccupied states in a higher band. Although one can measure the MO effects by placing the sample in between two almost crossed polarizers, one often employs a photo-elastic modulator (PEM) [5, 7] in a MO measurement setup. The use of a PEM will result in an increase of the signal to noise (S/N) ratio of the measured Kerr or Faraday signals. In a PEM a standing sound wave in the optical head adds a time dependent phase shift between two orthogonal components of the polarized laser beam by strain induced birefringence. This leads to the modulation of the intensity that is proportional to the MO properties of the materials studied. The PEM modulates the state of polarization of the light beam and enhances the sensitivity of the setup. Such a single beam detection method has shown to be sensitive to intensity, frequency, and beam direction fluctuations of the laser light source as well to temperature and frequency drifts of the modulator. The appendix D shows the Mathcad simulation of change in Fresnel reflection coefficients as a function of angle of incidence of the laser. To improve the MO

measurement method, a dual beam approach is explored. A dual beam has been employed previously for simple Kerr setups using almost crossed polarizers [8] but has not yet been used for a modulated Kerr set-up that uses a PEM.

1.2 Magneto Optical Kerr Effect

The discovery of the MO effect in 1945 by Michael Faraday marked the first observation of an interaction between light and magnetism [9], as well as the beginning of the field of magneto-optics. Faraday's findings were further expanded upon when in 1876 John Kerr discovered the corresponding effect in the reflection of polarized light from the pole of a magnet [1]. An introduction into MO effects shows that the phenomenon arises from the different interactions of the magnetized medium to right and left-handed circularly polarized light. Linearly polarized light, however, with a given plane of polarization, may be expressed as the superposition of two circularly polarized components, that is, it is a decomposition of right-handed and left-handed circularly polarized waves. The MO Kerr effect may also result in the reflected light wave becoming elliptically polarized, but unlike reflection from a non-magnetized surface, the plane of polarization may also undergo a rotation. The MO Kerr effect is manifested as a change in polarization or in the intensity of light that is reflected from the surface of a magnetized medium, the size of which depends upon the material, the saturation magnetization of the surface domains, the wavelength of the incident light, and the angle of incidence. The underlying description for the MO Kerr effect, as well as the Faraday Effect, lies in the dielectric optical tensors, which describes the optical and MO properties of a medium by the motion of its electrons. When a sample has a surface magnetization, off-diagonal terms

arise in the dielectric tensor, which ultimately causes the magneto-optical phenomenon [10].

1.3 Spin Orbit Interaction

To fully understand the MO effect, one must look at the electric transitions between individual energy states in an insulator or between energy bands in a conductor [11]. A quantum description of MO effects of solid materials must consider electric contributions from intra-band and inter-band electronic transitions. These are the transition between initially occupied and empty final energy states within an energy band or between energy bands. Since the transitions between some energy states are not permitted, the material in general will have different absorption coefficients for right and left circularly polarized light. This effect is responsible for the MO Kerr ellipticity. The material will also have different refraction indices for right and left circularly polarized light. This effect causes the MO Kerr rotation. Using the selection rules from quantum mechanics one can determine which transitions are highly likely and which transitions are unlikely (forbidden). A simplified version of allowed transitions is shown in figure below. The lines represent energy bands and not individual, separate energy levels.

Figure 1.1 shows a simplified energy diagram for the case of no spin (left 'a'), the presence of exchange splitting or an external field (center 'b'), and the presence of a field and or spin exchange interaction and spin orbit interaction (right 'c'). The degeneracy depends on the quantum numbers for each case. The orbital quantum number l takes all the values from 0 to $(n-1)$, while the magnetic quantum number m_l can take values of integers between \pm the

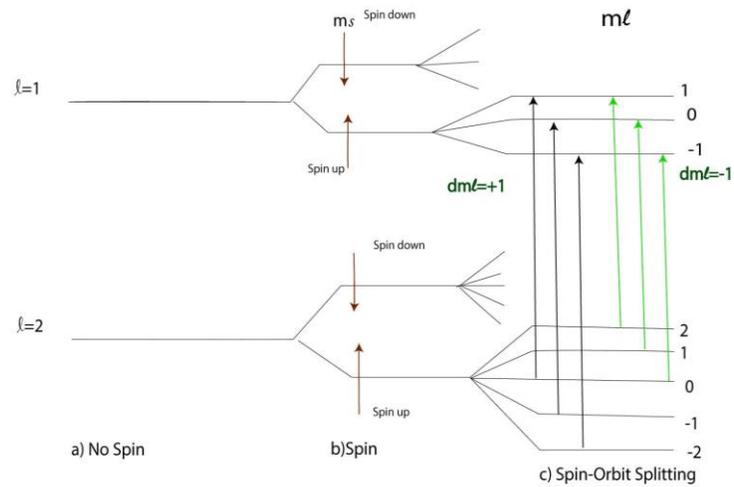


Figure 1.1 Effect of exchange splitting and spin orbit interaction on the allowed optical transitions [11]

values of orbital quantum number l and zero. That is $m_l = 0, \pm 1, \dots \pm l$. Part (a) represents two fully degenerate energy bands. These energy values depend on the principal quantum numbers. States with different l are assumed to have different energy levels. Part (b) represents the effect of an applied field for paramagnetic materials and the effect of exchange interaction for ferromagnetic materials. These levels take the magnetic spin quantum numbers m_s into account. Spin up and spin down bands have different energies. As for (b) no spin interaction is assumed, states with different m_l have the same energy so the bands in (b) are degenerate energy bands. Assuming no spin flipping, equal optical transitions between occupied and unoccupied states of available spin up and spin down levels are expected for the (b) case. Note that

the MO effects originate from different absorption for RCP and LCP light. Since RCP and LCP photons carry an angular momentum of \hbar and $-\hbar$. The selection rules for RCP (LCP) lights are: $\Delta m_l = m_{l,initial} - m_{l,final} = \pm 1$. Namely $\Delta l = \pm 1$ and $\Delta m = \pm 1$. As the photons do not interact with the electron spin, the Δs and Δm_s can be considered zero. The selection rules for l are; $\Delta l = l_{initial} - l_{final} = \pm 1$. And originates from the fact that the wave functions have parity $(-1)^l$ [10]. So, no MO effects are expected for the (b) case as for each possible RCP transition there is an LCP transition. For part (c) spin-orbit interaction is included. So, the degeneracy of bands is further removed since, bands with different m_l have a different energy level. The arrows represent the allowed optical transitions after using the optical transition selection rules. The absorption of RCP happens when $\Delta m = \pm 1$. A $\Delta m = -1$ transition describes the absorption for an LCP photon. From the figure above, it is clear that different energies for the RCP and LCP absorption occur. So, at a certain energy, the total absorption of RCP lights differs from that of LCP light. So, the presence of exchange interaction and spin-orbit interaction is the reason for the MO Kerr effects.

1.4 MOKE Geometries

Depending on the relative orientation of the Magnetization \mathbf{M} with respect to the plane of incidence of the light, one can distinguish between different MOKE effects, [12] see figure below. The Polar MOKE effect arises when the applied magnetic field on the sample has a direction perpendicular to the substrate. After reflection, two changes occur to the state of polarization of the light. One is the slight rotation of the plane of polarization of the light and two is the change in ellipticity of the light [13]. Both effects are considered to be linear

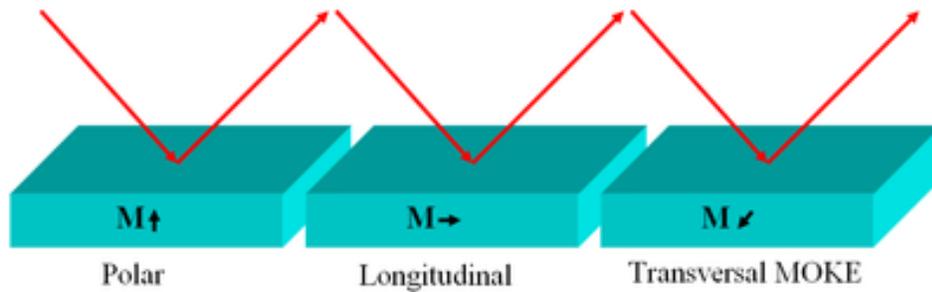


Figure 1.2 Different MOKE geometries [45]

proportional to the magnetization in the material. The polar Kerr effect depends on the angle of incidence of the beam and is maximum at perpendicular incidence and approaches zero at large angles.

For the longitudinal Kerr effect \mathbf{M} is parallel to the surface and is in the plane of incidence (see also figure 1.2 above). The longitudinal Kerr effect is zero at perpendicular incidence. Also, at very large angle the effect is small. Also, the longitudinal Kerr effect changes the SOP of the incident beam. For the transverse effect \mathbf{M} is parallel to the surface and is perpendicular to the plane of incidence.

In general, the polar MOKE gives the largest Kerr rotation. It is also the method which has been studied the most, due to its importance in magneto-optical recording technology.

Longitudinal MOKE is sensitive to the in-plane magnetization on the surface of the medium [14]. This geometry is useful when studying magnetic elements with shape anisotropy, where the physical dimension of the magnetic medium is small in one direction, e.g. a magnetic ultra-thin film. In particular, longitudinal MOKE has been extensively used to study magnetic domain interactions on the micro and Nano-scale, as well as magnetic thin film structures. Whereas polar and longitudinal MOKE both give

rise to a rotation of the polarization plane of the incident light. The transverse effect only results in a modulation of the intensity. This is due to the Kerr component of the reflected light being parallel to the normal Fresnel reflection component in the transverse geometry.

1.5 Overview on Single Beam Modulated MOKE and Dual Beam Modulated MOKE

In a conventional single beam MOKE setup, Glan-Taylor prisms are used [15-17]. Where linearly polarized light is incident normally on a sample in a magnetic field in a direction perpendicular to the plane of incidence. After reflection, in addition to the usual Fresnel amplitude component, a small orthogonal Kerr component appears that, in combination with the optical component, leads to elliptically polarized light slightly rotated with respect to the polarization plane of the incident beam. Rotation and ellipticity are summarized in a complex number, the complex Kerr rotation [1, 12]. The rotation and the ellipticity change upon reflection depend on the magnetic moment in the sample.

But in a Glan-Taylor prism only the P-polarized light is transmitted, and S-polarized light is either absorbed by a blackened side face or emitted through a clear side exit window.

The light exiting through the side window is poorly polarized. So, to monitor both S and P-polarized light after transmission through the sample, the Glan-Taylor prism has to be replaced by some polarizing beam splitter, such as a Wollaston prism that will split the beam reflected of the sample in two high quality orthogonal polarized beams. After the spitting of the beam in an e-ray and an o-ray each beam can be analyzed independently using two silicon detectors. An additional lock-in amplifier and voltmeter will be

required to detect both detector signals independently.

A single beam MOKE setup is sensitive to laser drifts, including drifts of the intensity, drifts of the wavelength, and drifts of the pointing direction. In addition, sample movements can cause the slight change in the incident angle of the laser beam and affect the measured signals. Those effects cause challenges for determining the MO properties, as MO Kerr signals are just a few milli volts. It is expected that the introduction of the dual beam detector technique reduces the effect of laser drifts as well as it is less sensitive to the sample movements.

1.6 Scope of the Thesis

The interaction of light with matter has recently received enhanced interest as it involves the electronic structure of the matter. In particular, in ferromagnetic materials, the interaction depends on the magnetic state of the medium, and this gives rise to MO effects.

Chapter 2 of this thesis introduces the reader to the polarization of electromagnetic waves, Jones vectors, how to describe polarized light and its interaction with optical components, and Jones matrices. The traditional MO Kerr study using two crossed polarizers and the study of MO Kerr using the polarization modulation technique will also be introduced in chapter 2. The apparatus for dual MOKE measurement will also be elaborated in detail in chapter 2.

In chapter 3 the dual beam detector technique is introduced. The optics alignment of the dual beam MOKE setup, and the multiple interference effect in the PEM are discussed using Jones matrix. The derived equations using the Jones matrix approach will be

checked for consistency with literature. Chapter 3 also reports on the LabVIEW programming performed to automate the data collection and to implement the external triggering so data is synchronously collected. In chapter 3 furthermore the time constants for measuring and sampling, the noise of laser and detectors, and the stability of the PEM are discussed.

The chapter 4 discusses the results of experiments performed to check the performance of the dual beam setup. Specifically measurement results of the signals of both channels as well as their difference (both dc and 2ω signals) as a function of analyzer orientation, PEM tilt angle and PEM retardation depth are presented. This chapter also compares the performance of the dual beam detector technique with the single beam measurement mode. The results are compared with the results of the Jones matrix calculations presented in chapter 3. Chapter 5 reports the measurement results on transitional metal oxides samples, including RF sputtered NiFe-Oxide and Ni-Oxide thin films. These materials are interesting for being applied in resistive RAM [18, 19]. Preliminary VSM measurements have shown that these materials sputtered under low oxygen flow have a net magnetic moment [20, 21]. This moment can be useful when studying the switching properties of RRAM.

The last chapter 6 of this thesis summarizes the results of all the experiments and makes suggestions for possible future research with the dual beam modulate MOKE setup.

2. MAGNETO OPTICAL KERR THEORY

The magneto optical effects are caused by the difference of the reflection of right and left circularly polarized light of magnetic materials. It originates from the exchange interaction and spin-orbit interaction of the involved materials. When polarized light is reflected from the surface of a Ferromagnetic material, the polarization of the reflected light differs from the polarization of the incident light. For linearly polarized incident light in general the reflected light is elliptically polarized. This effect is referred to as the MOKE. To describe the MO effects, that is the interaction of the electromagnetic wave with the ferromagnetic material, one need to use a technique that takes the state of polarization (SOP) of the light beam into consideration. Although various methods exist, in this thesis Jones matrices were used.

2.1 Polarization of an Electromagnetic Waves

The trajectory that the electric field vector of an electro-magnetic wave describes as a function of time at a certain location is known as the state of polarization of the wave. Many magneto-optical applications such as MOKE Microscopy, MO data, MOKE Magnetometry, etc. depend on the effect the material has on the state of polarization of light reflected off or transmitted through the material.

Depending on the light source, the electromagnetic-wave can be emitted without a particular polarization, which means that the wave is the superposition of randomly distributed polarizations. This wave is said to be randomly polarized or unpolarized [6]. An electromagnetic wave whose electric field vector has a periodicity in its temporal and spatial behaviour is said to be a polarized wave. Consider the following expression

for the electric field of an electromagnetic plane wave propagating along the positive z-axis:

$$\vec{E} = \hat{i}E_x + \hat{j}E_y \quad 2.1$$

$$E_x = E_{0x}e^{i(kz-\omega t+\phi_x)} = E'_{0x}e^{i\phi_x}e^{i(kz-\omega't)} \quad 2.2$$

$$E_y = E_{0y}e^{i(kz-\omega t+\phi_y)} = E'_{0y}e^{i\phi_y}e^{i(kz-\omega't)} \quad 2.3$$

Where k and ω' are the wave vector and angular frequency of propagation of an electromagnetic plane wave, and t is the time.

$$\vec{E} = [\hat{i}E_{0x} + \hat{j}E_{0y}]e^{i(kz-\omega't)} \quad 2.4$$

Note that E_{0x} and E_{0y} are complex numbers and they unambiguously describe the SOP of the light. In general, the equation 2.4 represents an elliptically polarized wave: at a given position in space, the electric field vector describes an ellipse. Two parameters characterize the ellipse: the angle between the major axis of the ellipse and the x-axis, and the ratio of the long and short axis of the ellipse. The latter is called the ellipticity and is defined as:

$$\varepsilon = \frac{E_{0x}}{E_{0y}} \quad 2.5$$

Two types of polarized lights are of particular importance. If the E – vector at a certain point in space describes a straight line the wave is said to be linearly polarized. The two orthogonal components along the ellipse degenerates in a straight line, the wave is said to be linearly polarized, characterized by a null phase difference between the components. The relative magnitude of both components determines the orientation of

electric field in the xy-plane. So, both E_{ox} and E_{oy} have the same argument but different modulus. For linearly polarized light whose plane of polarization makes an angle of α with the x-axis the SOP is described by the following equation:

$$\vec{E} = [\hat{i} \cos(\alpha) + \hat{j} \sin(\alpha)] e^{i(kz - \omega' t)} \quad 2.6$$

Note that one can multiply both components with a constant without changing the polarization of the wave. This component can be even complex. If the electric field vector at a certain point along the z-axis describes a circle, the wave is said to be circularly polarized. The state of polarization is characterized by a phase difference of $\pm \pi \frac{1}{2}$ between the two orthogonal components. Furthermore, the amplitude of each component is the same. i.e. $E'_{ox} = E'_{oy}$. Such that,

$$\vec{E} = [\hat{i} \pm \hat{j} i] e^{i(kz - \omega' t)} \quad 2.7$$

Where i represents the square root of minus one and \hat{i} and \hat{j} represent the unit vectors in the x and y directions. The plus sign is for left circularly polarized (LCP) wave and the minus sign for right circularly polarized wave (RCP) [22, 23]. Left and right are defined when looking into the laser beam towards the laser.

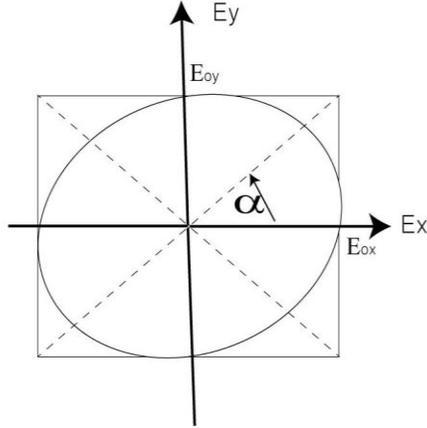


Figure 2.1 Polarization of an ellipse

For elliptically polarized light the two orthogonal components are in general not phase shifted by 90 degrees. However, if one describes the elliptically polarized light of the figure by the sum of linearly polarized light parallel to the long axis of the ellipse and linearly polarized light along the short axis of the ellipse, both components are exactly 90 degrees phase shifted with respect to each other.

2.2 Jones Vectors of Polarized Light and Special Polarizations

The Jones matrix method provides a mathematical description of the SOP of the light, as well as a means to calculate the effect that an optical device will have on input light of a given polarization state. The Jones vector, a 2x 1 matrix is just a simple shorthand way to represent the polarization state of the light [23, 24]. It is the first part of equation 2.4, i.e.

$$\vec{E} = [\hat{i}E_{ox} + \hat{j}E_{oy}]e^{i(kz - \omega't)} = \begin{pmatrix} E_{ox} \\ E_{oy} \end{pmatrix} e^{i(kz - \omega't)} \quad 2.8$$

Where $\begin{pmatrix} E_{ox} \\ E_{oy} \end{pmatrix}$ is the Jones vector and unambiguously describes the SOP of a light.

Note that the components of the Jones vector can be a complex number, so both amplitude and phase information is present. Oftentimes, however, it is not necessary to know the magnitude and phase of both components of the Jones vector. The argument difference between both components and the ratio of the moduli of both components of the Jones vector unambiguously determines the SOP. Therefore, Jones vectors can be normalized, and common phase factors can be neglected.

Most often the basis of the Jones vector is chosen to be the horizontal and vertical linearly polarized states. In such case the representation for these two states can be given as:

$$\vec{E}_h = \begin{pmatrix} E_x(t) \\ 0 \end{pmatrix} = \begin{pmatrix} E_{ox} e^{i(kz - \omega' t)} \\ 0 \end{pmatrix} \quad 2.9$$

$$\vec{E}_v = \begin{pmatrix} 0 \\ E_y(t) \end{pmatrix} = \begin{pmatrix} 0 \\ E_{oy} e^{i(kz - \omega' t)} \end{pmatrix} \quad 2.10$$

The normalized Jones vectors for both beams are $\vec{E}_{ho} = \begin{pmatrix} 1 \\ 0 \end{pmatrix}$ and $\vec{E}_{vo} = \begin{pmatrix} 0 \\ 1 \end{pmatrix}$

Where \vec{E}_{ho} and \vec{E}_{vo} represents horizontal linearly and vertical linearly polarized light.

The Jones matrix of the sum of two coherent light beams is given by the sum of their corresponding Jones vector components. So, the Jones vector of the sum of a horizontal and a vertical linearly polarized beams is given by:

$$\vec{E}_h + \vec{E}_v = \begin{pmatrix} 1 \\ 1 \end{pmatrix} \quad 2.11$$

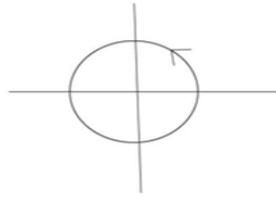
Note that this Jones vector represents light that is linearly polarized at 45 degrees angle with respect to the horizontal.

Two other common polarization states are right and left circular polarized light. In both cases the two components have equal amplitude, but for right circularly polarized light the phase of the y-component leads the x-component by $\frac{\pi}{2}$, while for left circularly polarized light it is the x-component that leads. Thus, the Jones vector representation for right-circularly polarized light (RCP) is:

$$\vec{E}_{RCP} = \begin{pmatrix} E_0 e^{i\phi} \\ E_0 e^{i(\phi - \frac{\pi}{2})} \end{pmatrix} \quad 2.12$$

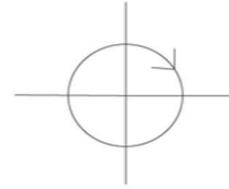
And after normalizing, $\vec{E}_{RCP} = \frac{1}{\sqrt{2}} \begin{pmatrix} 1 \\ -i \end{pmatrix}$ And similarly, the expression for left circularly polarized light is $\vec{E}_{LCP} = \frac{1}{\sqrt{2}} \begin{pmatrix} 1 \\ i \end{pmatrix}$. Examples of Jones vectors of different polarized light are provided in the figure 2.2 below.

Circular Polarization ($\Delta\phi=\pi/2$)



Left:

$$\vec{E}_0 = \frac{1}{\sqrt{2}} \begin{pmatrix} 1 \\ i \end{pmatrix}$$



Right:

$$\vec{E}_0 = \frac{1}{\sqrt{2}} \begin{pmatrix} 1 \\ -i \end{pmatrix}$$

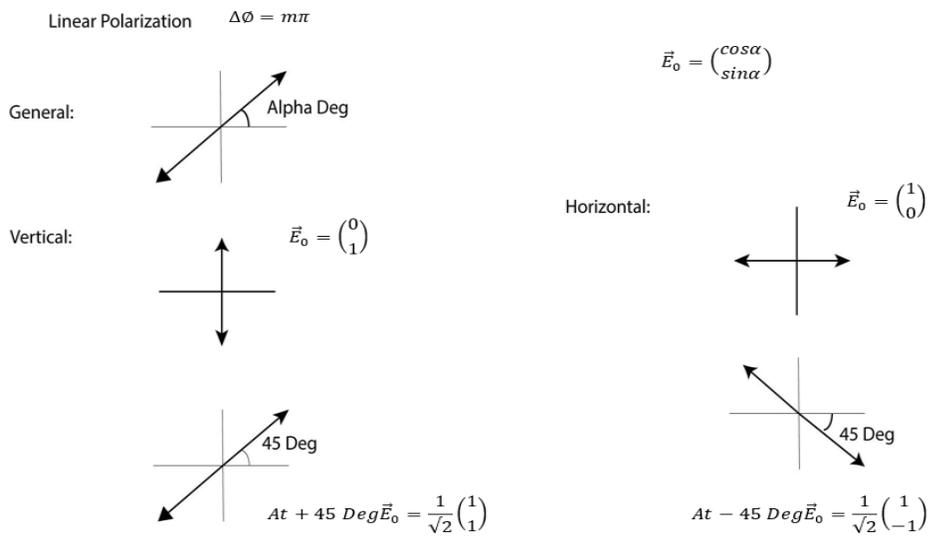


Figure 2.2 Jones vector of circularly and linearly polarized light

2.3 Jones Matrices

Now, if we consider a light beam represented by the Jones vector $\vec{E}_i = \begin{pmatrix} E_{xoi} \\ E_{yoi} \end{pmatrix}$ incident

on an optical device the light will interact with the device and the polarization state of the

light reflected or transmitted through the device can be written as $\vec{E}_t = \begin{pmatrix} E_{xot} \\ E_{yot} \end{pmatrix}$.

To describe the effect of optical components on the state of polarization (SOP) of the

light 2x2 matrices are used. Those matrices are called Jones matrices [24, 25, 26].

The Jones vector of the transmitted light is calculated from a multiplication of the Jones matrix of the optical component with the Jones vector of the incident light.

$$\begin{pmatrix} E_{xot} \\ E_{yot} \end{pmatrix} = \begin{pmatrix} a & b \\ c & d \end{pmatrix} \begin{pmatrix} E_{oxi} \\ E_{oyi} \end{pmatrix} \quad 2.13$$

Where $\begin{pmatrix} E_{oxi} \\ E_{oyi} \end{pmatrix}$ is the Jones vector of the light incident on the optical component and

$\begin{pmatrix} E_{xot} \\ E_{yot} \end{pmatrix}$ is the Jones vector of the light that is transmitted through the optical component.

Note that the first (second) column of the Jones matrix represents the Jones vector of the transmitted light if the incident light is linearly polarized along the x-direction (y-direction):

$$\begin{pmatrix} a & b \\ c & d \end{pmatrix} \begin{pmatrix} 1 \\ 0 \end{pmatrix} = \begin{pmatrix} a \\ c \end{pmatrix} \quad 2.14$$

$$\begin{pmatrix} a & b \\ c & d \end{pmatrix} \begin{pmatrix} 0 \\ 1 \end{pmatrix} = \begin{pmatrix} b \\ d \end{pmatrix}$$

Such that,

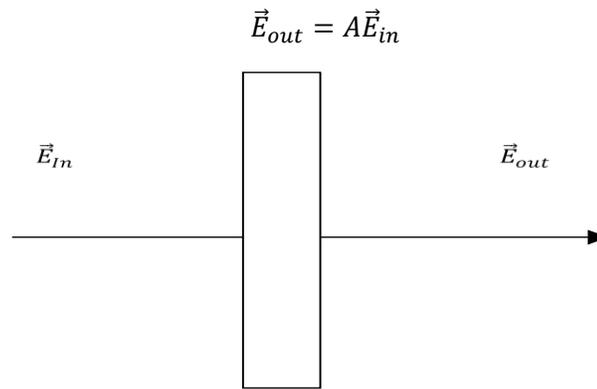


Figure 2.3 Jones matrix mathematics operation

This idea can be used to determine the Jones matrix of the optical component.

The coupling between this light vector of the incident light with an optical component in the set can be fully described by a set of 4 coefficients, i.e. a, b, c, and d.

The coupling can be given by the following pair of equations:

$$\vec{E}_{tx} = aE_{ix} + bE_{iy} \quad 2.15$$

$$\vec{E}_{ty} = cE_{ix} + dE_{iy} \quad 2.16$$

These two equations can be written using matrix notation as $E_t = J \vec{E}_i$. Where $J =$

$\begin{bmatrix} a & b \\ c & d \end{bmatrix}$ is the Jones matrix of an optical device.

Jones matrix of different optical components.

1. Wave plates

Wave plates are often used for MOKE studies. A waveplate or retarder is an optical device that alters the polarization state of light travelling through it. The most used waveplates are half waveplates, which shift the polarization direction of linearly polarized light. Other waveplates, quarter waveplates, convert linearly polarized lights into circularly polarized light and vice versa [27]. A quarter waveplate can also be used to produce elliptically polarized light. The behaviour of these waveplates depends on the thickness of the crystal, the wavelength of the light in use, and the anisotropy of the index of refraction of the waveplate's material. These waveplates are constructed out of a birefringent material (crystalline quartz or silica) for which the index of refraction is different for different SOP of the light passing through it. By the appropriate choice of the relationship between these parameters, it is possible to introduce a controlled phase shift between the two-polarization components of the light wave, thereby altering its

polarization. The waveplate or retarder increases the phase by $\phi/2$ along the fast (x-axis) and retards the phase by $-\phi/2$ along the slow (y-axis).

The Jones vector of the transmitted light through a waveplate can be written as:

$$\begin{pmatrix} E_{xot} \\ E_{yot} \end{pmatrix} = \begin{pmatrix} e^{i\phi/2} & 0 \\ 0 & e^{-i\phi/2} \end{pmatrix} \begin{pmatrix} E_{oxi} \\ E_{oyi} \end{pmatrix} \quad 2.17$$

2. Polarizer:

The Jones matrix of a polarizer with its transmission axis at θ degree with the horizontal is given by:

$$\begin{bmatrix} \cos^2\theta & \cos\theta\sin\theta \\ \cos\theta\sin\theta & \sin^2\theta \end{bmatrix} \quad 2.18$$

An ideal polarizer produces linearly polarized light from unpolarized light. Two ideal polarizers would eliminate all light if their transmission axes are perpendicular to each other. Polaroid sheet polarizers and prisms are mostly used for polarizers.

The Polaroid or the dichroic material preferentially absorbs linearly polarized light with a certain orientation, typically transmitting less than 1 % through a sheet of Polaroid. The Polaroid is a sheet of iodine impregnated polyvinyl alcohol [27,28]. A sheet of polyvinyl alcohol is heated and stretched in one direction. While softened, it has the effect of aligning the long polymeric molecules in the direction of stretch. When dipped in iodine, the iodine atoms attach themselves to the aligned chain. The electrons then can move easily along the aligned chains. The light waves that have an electric field vector parallel to these aligned chains are strongly absorbed because of the dissipative effects of the electron motion in the chains. Polaroid materials accomplish polarization by dichroism. Birefringence is an optical phenomenon that appears when the light passes through an optically anisotropic crystal: the incident light beam will split in two light beams as

orthogonal components of the polarized light experience different indices of refraction. The unpolarized light wave has the electric-field vector vibrating in all directions. When brought upon the birefringent material, the effect of birefringence causes the unpolarized light beam to separate into beams that travel in two slightly different directions. When emerging from the crystal both beams are spatially separated. Note that for the Glan-Thompson and Glan-Taylor prisms, one of the beams never emerges from the crystal. Examples for polarizers that utilize optical birefringence are the Glan-Taylor and the Wollaston prisms.

Cube polarizers are also used as beam-splitters. Polarized beam splitting cubes are manufactured by optically cementing two precision right angled prisms together along the hypotenuse length. The cube allows p-polarized light to pass un-deviated through the cube while s-polarized light is reflected at 90 degrees. The p-polarized light is the one which is parallel to the transmission axis of the light and s-polarized light is the one which is perpendicular to the transmission axis. The extinction ratio of cube beam splitters are just 1000:1 [29]. The extinction ratio of a Wollaston prism though is very high. The figure 2.4 below shows the family of polarizing prisms.

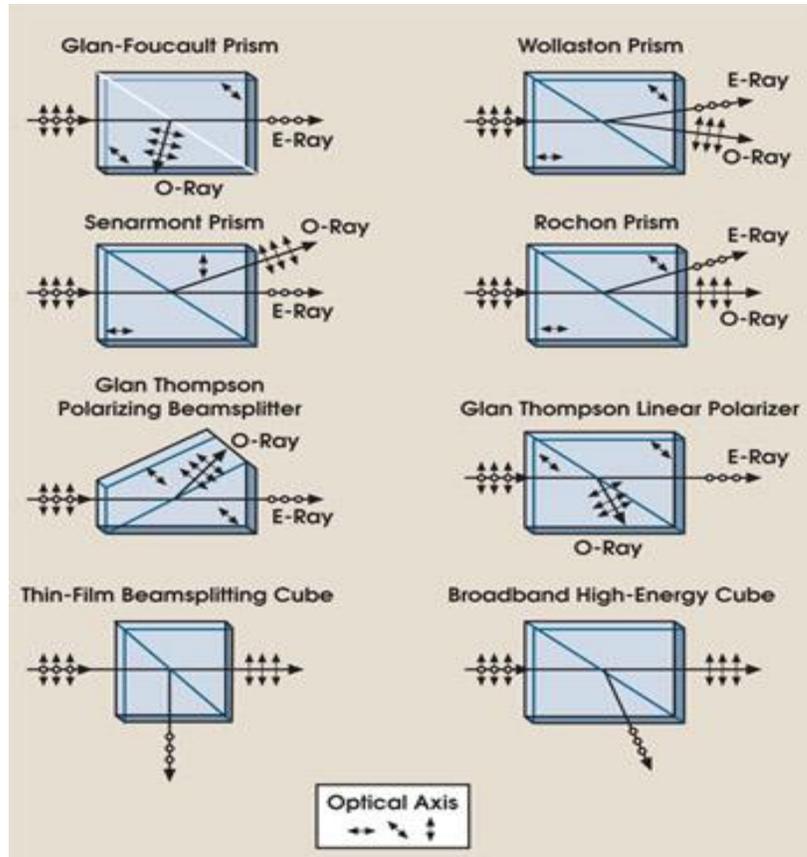
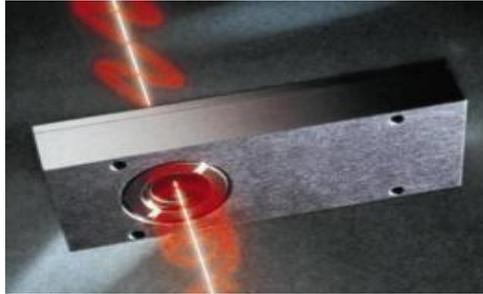


Figure 2.4 Family of polarizing prisms [46]

3. Photo- elastic Modulator:

The Photo-elastic modulator (PEM) is an optic device that works under the principle of the photo elasticity of light [30]. The PEM is a resonant device where the frequency of oscillation is determined by the optical head and transducer assembly. The electric transducer is tuned to the resonance frequency of optical head along its length. An alternating voltage is sent to the piezo-transducer to introduce a standing sound wave in the optical head causing compressive and tensile strain as a function of time in the optical head. This time varying strain modulates the refractive index for both S- and P- polarized



**Figure 2.5 Photo elastic modulator
[HINDS Instruments]**

light through birefringence [30, 31, 32]. When the transparent material is compressed or expanded, the speed with which a linearly polarized light travels through the material changes. Most Hinds PEMs use a crystalline quartz piezo-electric transducer to vibrate a fused silica optical head at its resonance frequency. The PEM-90 consists of a rectangular bar of fused silica attached with glue to the piezoelectric transducer. The bar vibrates along its long dimension at a frequency determined by the length of the bar and the speed of a longitudinal sound wave in the optical element material. The transducer is then tuned to the same frequency and is driven by an electronic circuit that controls the amplitude of vibration. The oscillating birefringence effect is at its maximum at the center of the fused silica bar. The electronic head and the PEM electronics control the amplitude of the oscillating crystal. To eliminate any ground loops through the electronic controls, the electronic head and optical head are electrically isolated.

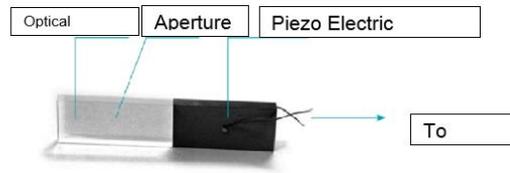


Figure 2.6 Simplest form of PEM-90 from HINDS

As the refraction index of the silica is modulated, the speed of light along the modulation axis changes. This change, in an oscillatory fashion, will cause a periodic phase shift between the horizontal and vertical components of the incident laser beams. If the light that is incident on the modulator is linearly polarized with equal horizontal (s) and vertical (p) components and the PEM is set to a retardation of a quarter wavelength, the transmitted light through the PEM will periodically change its state of polarization between LCP and RCP. If one considers the X component of light to be the axis of modulation, then in time the X component of light will lag the Y component of light during the compressive strain half cycle and lead the Y component of the light during the tensile strain half cycle. The phase difference between X and Y components of the light beam at any point in time defines the retardation.

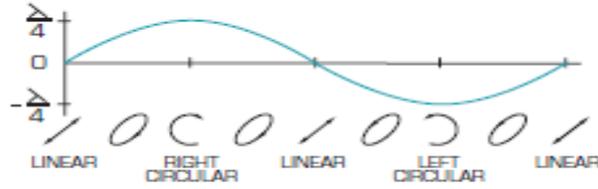


Figure 2.7 Retardation of PEM [47]

The time dependent phase delay between two perpendicular polarization axes will result in polarization being swept from linearly, to right circularly, to linearly, to left circularly polarized, and then back again. The full cycle is, LP-RCP-LP-RCP-LP-LCP-LP (figure 2.7). In the modulated MOKE measurements, the output is approximately sinusoidal in shape with a frequency of $2f$, f being the modulation frequency of the PEM.

The Jones matrix of the photo-elastic modulator is given by;

$$M = t'^2 \begin{bmatrix} e^{i\phi_p \frac{1}{2}} & 0 \\ 0 & e^{i\phi_s \frac{1}{2}} \end{bmatrix} \quad 2.19$$

Where, $\phi_p = e^{i(\delta_1 + \delta_{po} \sin(\omega t))}$ and $\phi_s = e^{i(\delta_1 - \delta_{so} \sin(\omega t))}$. $\omega = 2\pi f$. δ_1 is the phase shift if the light travels one time through the unstrained PEM, δ_{po} and δ_{so} are the time dependent phase amplitudes for p and s-polarized light for a light beam that travels one time through the optical head. The 't' is the transmission coefficient when the light enters the optical head and when it is leaving it, ϕ_p is the optical path length in radians of the p-component when traveling one time through the PEM and ϕ_s is the optical path length in radians of the s-component when traveling one time through the PEM. Both optical path length components contain a positive offset which value depends on the film

thickness of the PEM and a sinusoidal component which has an opposite sign for both p and s components of light. As the offset term is the same for both components it has no effect on the SOP and is normally ignored. For the PEM-90 the sinusoidal terms have different amplitudes for both components. For the dual axis PEM-100 both sinusoidal have the same amplitude. Ignoring the offset term, the Jones matrix of the PEM can be written by:

$$M = e^{i\delta_1} \begin{bmatrix} e^{i\frac{\delta_{p0}}{2}\sin(\omega t)} & 0 \\ 0 & e^{-i\frac{\delta_{s0}}{2}\sin(\omega t)} \end{bmatrix} \sim \begin{bmatrix} e^{i\frac{\delta_{p0}}{2}\sin(\omega t)} & 0 \\ 0 & e^{-i\frac{\delta_{s0}}{2}\sin(\omega t)} \end{bmatrix} \quad 2.20$$

Where δ_1 depends on the thickness of PEM and is the offset term that has no effect on the intensity and the SOP and ω is the angular frequency of the PEM which is 50KHz for the PEM-90. Note that the diagonal components of the Jones matrix of a biaxial PEM ($\delta_{p0} = \delta_{s0}$) are complex conjugated of each other.

4. Photo-elastic modulator with multiple interference effect included:

The multiple interference effect occurs because of the internal reflection of the laser inside the PEM's optic head [37-40]. This interference causes problems when measuring the MO Kerr signals. Figure 2.8 below shows the multiple reflection of the laser beam upto 4 times through the PEM's optical head.

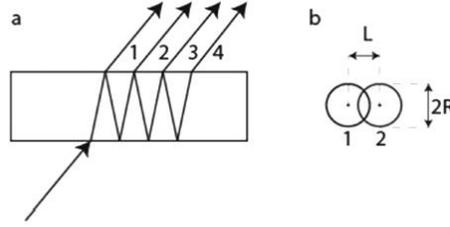


Figure 2.8 Multiple interference effect in PEM
[43]

Including the multiple interference, the Jones matrix of the PEM can be written as:

$$\begin{aligned}
 M &= t'^2 \begin{bmatrix} e^{i\phi_p \frac{1}{2}} \sum_{n=0}^{\infty} r^{2n} e^{i\phi_p n} & 0 \\ 0 & e^{i\phi_s \frac{1}{2}} \sum_{n=0}^{\infty} r^{2n} e^{i\phi_s n} \end{bmatrix} = & 2.21 \\
 & t'^2 \begin{bmatrix} e^{i\phi_p \frac{1}{2}} \frac{1}{1 - r^2 e^{i\phi_p}} & 0 \\ 0 & e^{i\phi_s \frac{1}{2}} \frac{1}{1 - r^2 e^{i\phi_s}} \end{bmatrix} \approx \\
 & t'^2 \begin{bmatrix} e^{i\phi_p \frac{1}{2}} (1 + r^2 e^{i\phi_p}) & 0 \\ 0 & e^{i\phi_s \frac{1}{2}} (1 + r^2 e^{i\phi_s}) \end{bmatrix}
 \end{aligned}$$

Where the expression for the geometrical series was used which is valid for $|z| < 1$.

Also a Taylor approximation was used to approximate the complex fraction. Note that these approximations are similar to assuming that only the first two transmitted beams interfere.

The term r is the internal Fresnel reflection coefficient for the fused quartz to air interface in the PEM's optical head, ϕ_p and ϕ_s are the optical path length of the light traveling one time through the PEM and consist of an offset term which depends on the PEM thickness and its optical properties and a sinusoidal term, i.e. $\phi_p = \delta_1 + \delta_{p0}\sin(\omega t)$ and $\phi_s = \delta_1 - \delta_{s0}\sin(\omega t)$. Substituting these expressions in the Jones matrix above gives:

$$M = e^{i\delta_1 t'^2} \quad 2.22$$

$$\begin{bmatrix} e^{i\frac{1}{2}\delta_{p0}\sin(\omega t)}(1 + r^2 e^{i(\delta_1 + \delta_{p0}\sin(\omega t))}) & 0 \\ 0 & e^{-i\frac{1}{2}\delta_{s0}\sin(\omega t)}(1 + r^2 e^{i(\delta_1 - \delta_{s0}\sin(\omega t))}) \end{bmatrix}$$

$$\approx e^{i\delta_1 t'^2} \begin{bmatrix} e^{i\frac{1}{2}\delta_{p0}\sin(\omega t)} T_p' & 0 \\ 0 & e^{-i\frac{1}{2}\delta_{s0}\sin(\omega t)} T_s' \end{bmatrix}$$

The components of the Jones matrix are no longer complex conjugated of each other. The figure 2.9 below shows the Phasor diagram for T_p' and T_s' without the pre-factor.

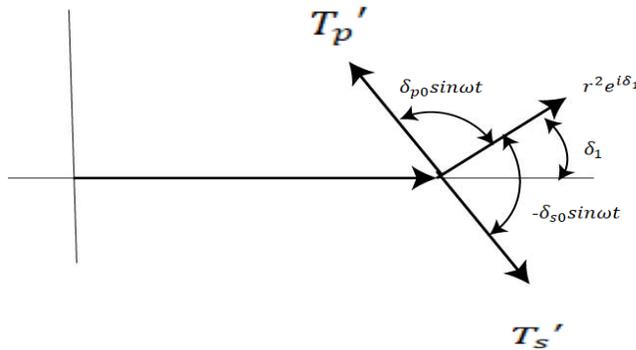


Figure 2.9 Phasor diagram for S and P component of light in the case of multiple interference effect

2.4 MOKE Setup Employing Polarizer and Analyzer

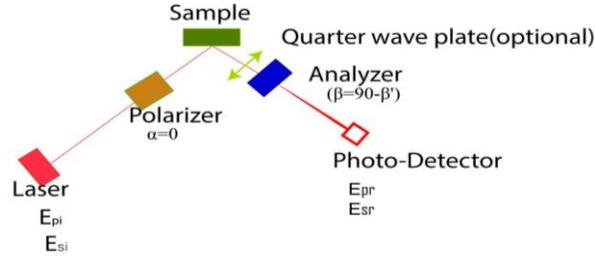


Figure 2.10 Experimental set-up used for Kerr Measurement

The traditional MO measurement setup is normally done using almost two crossed polarizers. A sketch of the setup is provided in the figure 2.10 above. We can use the Jones Matrix approach to see what happens to the intensity that is measured by the detector. For this purpose, it is assumed that the polarizer is oriented at 0 degrees. So, the Jones matrix for the polarizer with transmission axis at $\alpha = 0$ is given by:

$$P = \begin{bmatrix} \cos^2 \alpha & \sin \alpha \cos \alpha \\ \sin \alpha \cos \alpha & \sin^2 \alpha \end{bmatrix} = \begin{bmatrix} 1 & 0 \\ 0 & 0 \end{bmatrix} \quad 2.23$$

Furthermore, the polar MOKE measurement configuration is assumed with light at perpendicular incidence; so $r_{pp} = r_{ss}$. The Jones matrix for the sample kept in a magnetic field perpendicular to the substrate is given by:

$$S = \begin{bmatrix} r_{pp} & r_{ps} \\ r_{sp} & r_{ss} \end{bmatrix} \quad 2.24$$

Where the diagonal terms, $r_{pp} = |r_{pp}|e^{i\delta_{pp}}$ and $r_{ss} = |r_{ss}|e^{i\delta_{ss}}$, are independent of magnetization and are identified as usual Fresnel reflection coefficients. The off-diagonal cross terms account for the magneto-optic Kerr effect and are anti-symmetric, $r_{ps} =$

$-r_{sp} = |r_{ps}| e^{i\delta_{ps}} = -|r_{sp}| e^{-i\delta_{sp}}$. The off-diagonal components depend on the magnetic moment of the sample. The Jones matrix for the analyzer with its transmission axis at $\beta = 90 - \beta'$ where β' is a small angle (assuming MOKE setup employing two crossed polarizers is β' angle off for second polarizer) is given by:

$$A = \begin{bmatrix} \cos^2(90 - \beta') & \sin(90 - \beta')\cos(90 - \beta') \\ \sin(90 - \beta')\cos(90 - \beta') & \sin^2(90 - \beta') \end{bmatrix} \quad 2.25$$

Furthermore, if one assumes circularly polarized incident light on the polarizer the Jones vector of the incident light is:

$$\vec{E}_i = \begin{pmatrix} 1 \\ i \end{pmatrix} \quad 2.26$$

The electric field vector amplitude of the reflected beam E_r at the photo detector can be represented by a vector equation as:

$$\vec{E}_r = \begin{pmatrix} E_{pr} \\ E_{sr} \end{pmatrix} = A \cdot S \cdot P \cdot \begin{pmatrix} E_{pi} \\ E_{si} \end{pmatrix} \quad 2.27$$

Where $\begin{pmatrix} E_{pi} \\ E_{si} \end{pmatrix}$ is the Jones vector of the light incident on the polarizer and $\begin{pmatrix} E_{pr} \\ E_{sr} \end{pmatrix}$ is the Jones vector of the reflected light. E_p and E_s are the E-vector complex amplitudes in the direction parallel and perpendicular to the plane of incidence. And A, S, P represent the multiplication of the Jones matrices of the analyzer, sample, and the polarizer respectively.

$$\begin{pmatrix} E_{pr} \\ E_{sr} \end{pmatrix} = \begin{bmatrix} \cos^2\beta & \sin\beta\cos\beta \\ \sin\beta\cos\beta & \sin^2\beta \end{bmatrix} \begin{bmatrix} r_{pp} & r_{ps} \\ r_{sp} & r_{ss} \end{bmatrix} \begin{bmatrix} 1 & 0 \\ 0 & 0 \end{bmatrix} \begin{pmatrix} 1 \\ i \end{pmatrix} \quad 2.28$$

Now consider the term A.S.P only,

$$\begin{aligned} & \begin{bmatrix} \cos^2(90 - \beta') & \sin(90 - \beta')\cos(90 - \beta') \\ \sin(90 - \beta')\cos(90 - \beta') & \sin^2(90 - \beta') \end{bmatrix} \begin{bmatrix} r_{pp} & r_{ps} \\ r_{sp} & r_{ss} \end{bmatrix} \begin{bmatrix} 1 & 0 \\ 0 & 0 \end{bmatrix} \begin{pmatrix} 1 \\ i \end{pmatrix} \quad 2.29 \\ & = \begin{bmatrix} \cos^2(90 - \beta') & \sin(90 - \beta')\cos(90 - \beta') \\ \sin(90 - \beta')\cos(90 - \beta') & \sin^2(90 - \beta') \end{bmatrix} \begin{pmatrix} r_{pp} \\ r_{sp} \end{pmatrix} \end{aligned}$$

Now, let's assume that β' is small so, $\cos^2(90 - \beta') = \beta'^2$, $\sin^2(90 - \beta') \approx$

$$1, \sin(90 - \beta')\cos(90 - \beta') = \beta'$$

Such that,

$$\begin{bmatrix} \beta'^2 & \beta' \\ \beta' & 1 \end{bmatrix} \begin{pmatrix} r_{pp} \\ r_{sp} \end{pmatrix} = \begin{pmatrix} r_{pp}\beta'^2 + r_{sp}\beta' \\ r_{pp}\beta' + r_{sp} \end{pmatrix} = r_{pp} \begin{pmatrix} \beta'^2 + \frac{r_{sp}}{r_{pp}}\beta' \\ \beta' + \frac{r_{sp}}{r_{pp}} \end{pmatrix} \quad 2.30$$

Now, use $\frac{r_{sp}}{r_{pp}} = \theta_k + i\eta_k$. Where θ_k is the Kerr rotation and η_k , Kerr ellipticity. Note that

if the material only shows a MO Kerr rotation that an electric field in the x direction should also create a polarization in the y direction. If there is no ellipticity, the reflected light is linearly polarized, so the $r_{ps}E_0$ should be in phase with $r_{pp}E_0$. So the existence of an MO Kerr ellipticity means the induction of a perpendicular component that is out of phase with the normal component. As the intensity falling on the detector can be written as $I\alpha|E_r|^2$, the detector intensity is given by:

$$\begin{aligned} I\alpha|E_r|^2 &= \beta'^2 + ((\theta_k + i\eta_k)\beta')^2 + (\beta' + (\theta_k + i\eta_k))^2 \quad 2.31 \\ &= (\beta'^2 + 1)(\beta' + \theta_k + i\eta_k)^2 \\ &= (\beta'^2 + 1)(\beta'^2 + 2\beta'\theta_k + \theta_k^2 - \eta_k^2) \\ &= (\beta'^2 + 1)2\beta'\theta_k + \dots \text{higher order terms} \end{aligned}$$

For small β' the higher order terms can be ignored, and the intensity is proportional to the MO Kerr rotation.

A dual beam detection scheme can be constructed by replacing the analyzer with a beam splitter that does not affect the SOP of the beam reflected from the sample and including additional analyzers and detectors in each beam see figure 3.1 for a typical setup. For the dual beam detection technique, the analyzer of one of the channels will be set at $-\beta$ degrees and the other to β degrees. Using equation 2.30 for each channel, the intensity difference can now be written as:

$$\Delta I = I_1 - I_2 \tag{2.32}$$

$$\sim (\beta'^2 + 1)2\beta'\theta_k - ((-\beta')^2 + 1)(-2\beta'\theta_k) = 2(\beta'^2 + 1)2\beta'\theta_k$$

So, for one channel the intensity increases and for the other channel the intensity decreases with θ_k . Note that ΔI only contains the MO signal and that the offset is canceled out. Similar expressions can be obtained if one uses a circular co-ordinate system, using a spherical polarized co-ordinate system as done by W. Bas Zeper [33].

The Jones matrix for ferro-magnetic material, can be written as:

$$S = \begin{bmatrix} r_{RCP} & 0 \\ 0 & r_{LCP} \end{bmatrix} \tag{2.33}$$

Where r_{RCP} and r_{LCP} are the Fresnel reflection coefficients of RCP and LCP light in circular co-ordinates system. The transformation of Jones vector from Cartesian co-ordinates system to circular co-ordinates system can be written as:

$$\begin{pmatrix} 1 \\ 0 \end{pmatrix} \rightarrow \begin{pmatrix} 1 \\ 1 \end{pmatrix} \text{ And } \begin{pmatrix} 0 \\ 1 \end{pmatrix} \rightarrow \begin{pmatrix} 1 \\ -i \end{pmatrix}$$

So, the coordinate transformation matrix to transform from Cartesian to circular coordinates is given by:

$$T_{ca-ci} = \frac{1}{\sqrt{2}} \begin{bmatrix} 1 & i \\ 1 & -i \end{bmatrix} \quad 2.34$$

And the inverse of this matrix can be given by:

$$T_{ci-ca} = \frac{1}{\sqrt{2}} \begin{bmatrix} 1 & 1 \\ -i & i \end{bmatrix} \quad 2.35$$

Now the Jones matrix of the sample can be written as:

$$\begin{aligned} \begin{bmatrix} r_{pp} & r_{ps} \\ r_{sp} & r_{ss} \end{bmatrix} &= \frac{1}{2} \begin{bmatrix} 1 & 1 \\ -i & i \end{bmatrix} \begin{bmatrix} r_+ & 0 \\ 0 & r_- \end{bmatrix} \begin{bmatrix} 1 & i \\ 1 & i \end{bmatrix} = \frac{1}{2} \begin{bmatrix} 1 & 1 \\ -i & i \end{bmatrix} \begin{bmatrix} r_+ & r_+ i \\ r_- & -r_- i \end{bmatrix} \\ &= \frac{1}{2} \begin{bmatrix} r_+ + r_- & i(r_+ - r_-) \\ -i(r_+ - r_-) & r_+ + r_- \end{bmatrix} \end{aligned} \quad 2.36$$

Where $r_{pp} = r_+ + r_- = r_{ss}$ and $r_{ps} = -r_{sp} = i(r_+ - r_-)$. Only the off-diagonal components give rise to the Kerr effect and the diagonal terms are independent of the magnetization of the sample. Also, $r_+ = r'_+ e^{i\phi_+}$, $r_- = r'_- e^{i\phi_-}$ where ϕ_+ , ϕ_- are the phase shift of RCP and LCP light.

Now let's consider one off-diagonal component as:

$$\begin{aligned} r_{ps} &= i(r_+ - r_-) = ir'_+ e^{i\phi_+} - r'_- e^{i\phi_-} \\ &= ir'_+(\cos\phi_+ + isin\phi_+) - ir'_-(\cos\phi_- + isin\phi_-) \end{aligned} \quad 2.37$$

Now if we use approximation that ϕ_+ and ϕ_- are small, then

$$i(r_+ - r_-) = ir'_+ - r'_+ \phi_+ - ir'_- + r'_- \phi_- = i(r'_+ - r'_-) + r'_- \phi_- - r'_+ \phi_+ \quad 2.38$$

Now consider

$$\begin{aligned} r_{pp} &= r_+ + r_- = r'_+ e^{i\phi_+} - r'_- e^{i\phi_-} \\ &= r'_+(\cos\phi_+ + isin\phi_+) + r'_-(\cos\phi_- + isin\phi_-) \\ &= 2r'_+ \end{aligned} \quad 2.39$$

After the approximation that $r'_+ = r'_-$ and $\phi_+ = \phi_-$

Now,

$$\frac{r_{ps}}{r_{pp}} = i(r'_+ - r'_-) + \frac{1}{2}(\phi_- - \phi_+) = \theta_k + i\eta_k \quad 2.40$$

With θ_k is the Kerr rotation and η_k is the Kerr ellipticity. This equation shows that the Kerr rotation is half the difference in phase shift for RCP and LCP light, and the Kerr ellipticity is caused by different absorption of RCP and LCP light.

2.5 MOKE Setup Employing a PEM

The photo-elastic modulator consists of an anisotropic crystal mounted on a piezo-electric transducer [30] that vibrates with the given modulation frequency. The oscillating pressure from the piezo-electric crystal thus changes the optical axis of the birefringent crystal inducing a time dependent birefringence [30, 31]. This periodic strain alternately retards or advances the phase of the horizontal component of light. The amplitude of the standing wave in the PEM defines the amplitude of the retardation. If its amplitude corresponds to a quarter wavelength of the incident laser light, and the incoming light is linearly polarized at 45 degree with respect to the optical axis, the SOP of the transmitted through the modulator alternate between left handed and right-handed polarized light.

Polarization Modulation with PEM for CD

(courtesy Hinds Instr.)

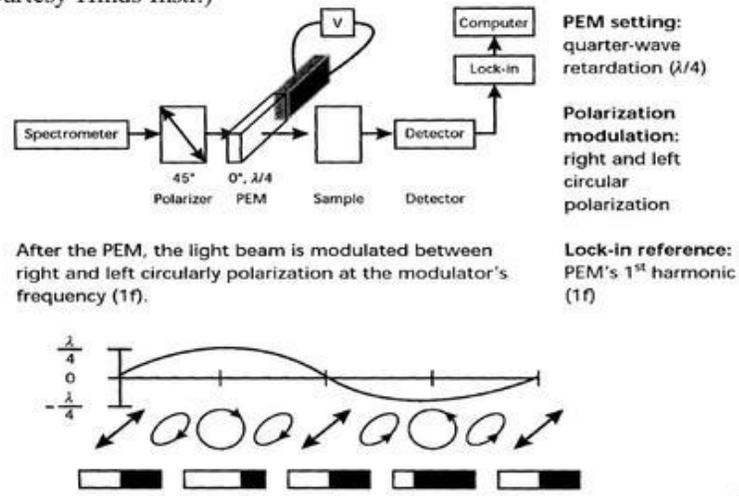


Figure 2.11 Polarization Modulation Technique for Kerr Measurement [48]

The above figure 2.11 shows the polarization modulation technique for the measurement of circular dichroism. A PEM is often used to measure the circular dichroism. For this measurement the polarizer is kept at 45 degrees. The PEM is kept between the polarizer and the sample. After the PEM the light beam is modulated between LCP and RCP at the PEM's modulation frequency $f = \frac{\omega}{2\pi}$. The setup of figure 2.11 only allows for the detection of the circular dichroism. If one also wants to determine the circular birefringence signal (Kerr rotation), an analyzer need to be added in front of the detector. The signals for such modified setup are shown in figure 2.12

Above figure 2.12 depicts the time dependence of the retardation and corresponding state of polarization, which varies from linear to left handed to linear to right handed to linear during every cycle of $1/f$ (see figure 2.12). If no MO effect is present, the x projection of the electric field vector on the detector (E_x), will produce a constant intensity on the

detector. If a Kerr rotation is present in the sample (c), all polarization states rotate through θ_k and E_x will vary with twice the modulation frequency f .

In the remaining part of this section the signal of the MOKE setup using PEM and analyzer is analyzed using Jones matrices. The figure 2.13 below shows the traditional single beam detector MOKE setup using a PEM.

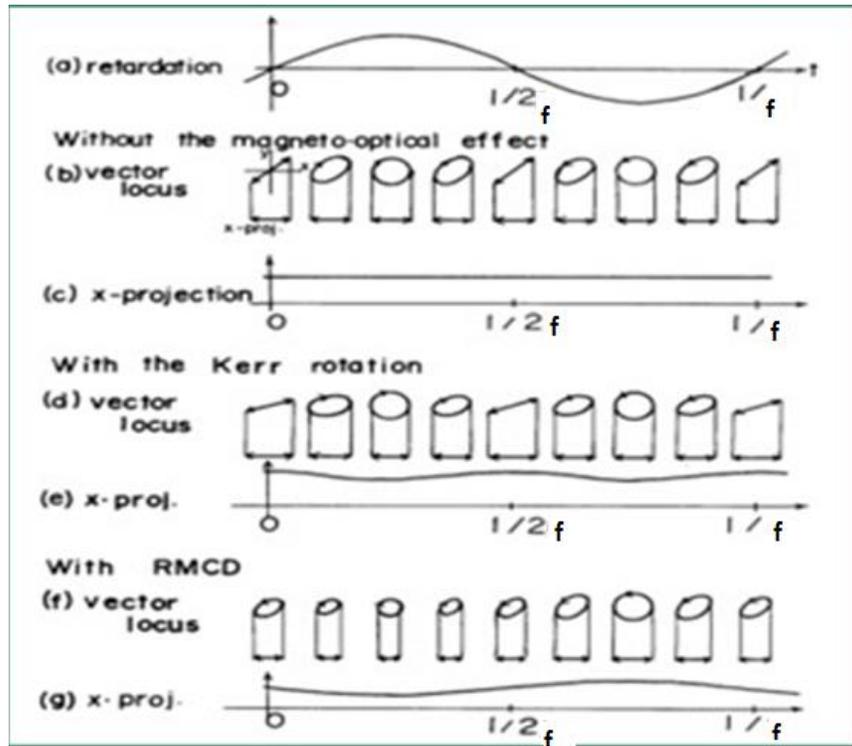


Figure 2.12 Polarization Modulation for Kerr Measurement [33]

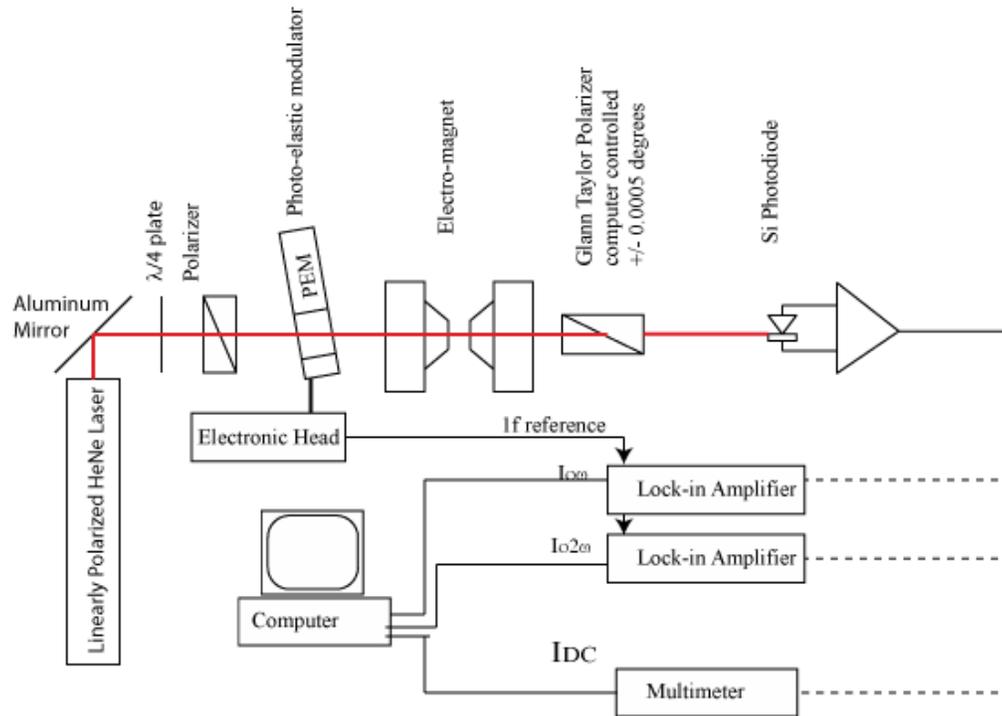


Figure 2.13 The single beam detector setup using PEM and Glan-Taylor prism

The above figure 2.13 shows the schematic drawing of the single beam detector technique for MO study. For polar Kerr measurements, measurements are normally done with the polarizer set to 45 degrees. So equal components for horizontal and vertical linearly polarized light are added in the incident beam. The Jones matrix of the polarizer is therefore given by:

$$P = \frac{1}{2} \begin{bmatrix} 1 & 1 \\ 1 & 1 \end{bmatrix} \quad 2.41$$

The Jones matrix of the photo-elastic modulator without the multiple interference effect is given by equation 2.22 as:

$$M = \begin{bmatrix} e^{i\phi\frac{1}{2}} & 0 \\ 0 & e^{-i\phi\frac{1}{2}} \end{bmatrix} \quad 2.42$$

Where ϕ is the retardation depth of the modulator which depends on the time and is given by the following expression:

$$\phi = \delta_0 \sin(\omega t) \quad 2.43$$

Where, δ_0 is the PEM's retardation amplitude. $\omega = 2\pi f$. f is the resonance frequency of the piezo electric transducer inside PEM's electronic head, and is also called the modulation frequency of the PEM. For PEM-90, $f = 50$ KHz and for PEM-100, $f = 43$ KHz.

The Jones matrix of the sample is given by:

$$S = \begin{bmatrix} r_{pp} & r_{ps} \\ r_{sp} & r_{ss} \end{bmatrix} \quad 2.44$$

Note that r_{pp} , r_{ps} , r_{sp} , and r_{ss} are also usual Fresnel reflection coefficients.

Where the diagonal terms $r_{pp} = |r_{pp}| e^{i\delta_{pp}}$ and $r_{ss} = |r_{ss}| e^{i\delta_{ss}}$, are independent of magnetization and are identified as usual Fresnel reflection coefficients.

The off-diagonal cross terms account for the MO Kerr effect and are anti-symmetric i.e.

$$r_{ps} = |r_{ps}| e^{i\delta_{ps}} = -r_{sp} = -|r_{sp}| e^{i\delta_{sp}}$$

The Jones matrix of the analyzer making an angle θ with transmission axis can be written as:

$$A = \begin{bmatrix} \cos^2\theta & \cos\theta\sin\theta \\ \cos\theta\sin\theta & \sin^2\theta \end{bmatrix} \quad 2.45$$

Where, θ is the orientation of the transmission axis of the analyzer with the horizontal.

The electric field vector amplitude of the reflected beam E_r at the photo detector can be represented by a vector equation as:

$$\vec{E}_r = \begin{pmatrix} E_{pr} \\ E_{sr} \end{pmatrix} = A.S.M.P. \begin{pmatrix} E_{pi} \\ E_{si} \end{pmatrix} \quad 2.46$$

Where $\begin{pmatrix} E_{pi} \\ E_{si} \end{pmatrix}$ is the Jones vector of the light incident on the polarizer and $\begin{pmatrix} E_{pr} \\ E_{sr} \end{pmatrix}$ is the Jones vector of the light incident on the detector. E_p and E_s are the E -vector amplitudes in the direction parallel and perpendicular to the plane of incidence. And A, S, M, and P represent the Jones matrices of the analyzer, sample (polar Kerr effect), modulator, and the polarizer respectively. Now the intensity signals falling on the detector can be written as $I\alpha|E_r|^2$

$$\begin{pmatrix} E_{pr} \\ E_{sr} \end{pmatrix} = A.S.M.P. \begin{pmatrix} E_{pi} \\ E_{si} \end{pmatrix} \quad 2.47$$

$$\begin{aligned} &= \frac{1}{2} \begin{bmatrix} \cos^2\theta & \cos\theta\sin\theta \\ \cos\theta\sin\theta & \sin^2\theta \end{bmatrix} \begin{bmatrix} r_{pp} & r_{ps} \\ r_{sp} & r_{ss} \end{bmatrix} \begin{bmatrix} e^{i\phi/2} & 0 \\ 0 & e^{-i\phi/2} \end{bmatrix} \frac{1}{2} \begin{bmatrix} 1 & 1 \\ 1 & 1 \end{bmatrix} \begin{pmatrix} 1 \\ -i \end{pmatrix} \\ &= \frac{1}{2} \begin{bmatrix} \cos^2\theta & \cos\theta\sin\theta \\ \cos\theta\sin\theta & \sin^2\theta \end{bmatrix} \begin{pmatrix} r_{pp}(1-i)e^{i\phi/2} + r_{ps}(1-i)e^{-i\phi/2} \\ r_{sp}(1-i)e^{i\phi/2} + r_{ss}(1-i)e^{-i\phi/2} \end{pmatrix} \end{aligned} \quad 2.48$$

$$= \frac{1}{2} \begin{pmatrix} a\cos^2\theta + b\cos\theta\sin\theta \\ a\cos\theta\sin\theta + b\sin^2\theta \end{pmatrix} \text{ where } a \quad 2.49$$

$$= r_{pp}(1-i)e^{i\phi/2} + r_{ps}(1-i)e^{-i\phi/2} \text{ and } b$$

$$= r_{sp}(1-i)e^{i\phi/2} + r_{ss}(1-i)e^{-i\phi/2}$$

$$= \frac{1}{2} \begin{pmatrix} aA + bB \\ aB + bA \end{pmatrix} \text{ where } A = \cos^2\theta, B = \cos\theta\sin\theta, C = \sin^2\theta \quad 2.50$$

Now,

$$I\alpha|E_r|^2 = \frac{1}{4} [p * p^* + q * q^*] \text{ where } p = aA + bB \text{ and } p^* = a^*A + b^*B \quad 2.51$$

So that,

$$\begin{aligned} p * p^* &= a \cdot a^* \cdot A^2 + a \cdot b^* \cdot AB + b \cdot a^* \cdot AB + b \cdot b^* \cdot B^2 \text{ and } q & 2.52 \\ &= aB + bC, q^* = a^*B + b^*C \end{aligned}$$

So that,

$$q * q^* = a \cdot a^* \cdot B^2 + a \cdot b^* \cdot BC + b \cdot a^* \cdot BC + b \cdot b^* \cdot C^2 \quad 2.53$$

Where,

$$\begin{aligned} a &= r_{pp}(1-i)e^{i\frac{\phi}{2}} + r_{ps}(1-i)e^{-i\frac{\phi}{2}} \text{ and } a^* & 2.54 \\ &= r_{pp}^*(1+i)e^{-i\frac{\phi}{2}} + r_{ps}^*(1+i)e^{i\frac{\phi}{2}} \end{aligned}$$

So that,

$$a \cdot a^* = r_{pp} \cdot r_{pp}^* \cdot 2 + 2 \cdot r_{pp} \cdot r_{ps}^* \cdot e^{i\phi} + 2 \cdot r_{ps} \cdot r_{pp}^* \cdot e^{-i\phi} + 2 \cdot r_{ps} \cdot r_{ps}^* \quad 2.55$$

Also, we have

$$\begin{aligned} b &= r_{sp}(1-i)e^{i\frac{\phi}{2}} + r_{ss}(1-i)e^{-i\frac{\phi}{2}} \text{ and } b^* & 2.56 \\ &= r_{sp}^*(1+i)e^{-i\frac{\phi}{2}} + r_{ss}^*(1+i)e^{i\frac{\phi}{2}} \end{aligned}$$

So that,

$$b \cdot b^* = 2 \cdot r_{sp} \cdot r_{sp}^* + 2 \cdot r_{sp} \cdot r_{ss}^* \cdot e^{i\phi} + 2 \cdot r_{ss} \cdot r_{sp}^* \cdot e^{-i\phi} + 2 \cdot r_{ss} \cdot r_{ss}^* \quad 2.57$$

Now,

$$a \cdot b^* = 2 \cdot r_{pp} \cdot r_{sp}^* + 2 \cdot r_{pp} \cdot r_{ss}^* \cdot e^{i\phi} + 2 \cdot r_{ps} \cdot r_{sp}^* \cdot e^{-i\phi} + 2 \cdot r_{ps} \cdot r_{ss}^* \quad 2.58$$

And,

$$b \cdot a^* = 2 \cdot r_{sp} \cdot r_{pp}^* + 2 \cdot r_{sp} \cdot r_{ps}^* \cdot e^{i\phi} + 2 \cdot r_{ss} \cdot r_{pp}^* \cdot e^{-i\phi} + 2 \cdot r_{ss} \cdot r_{ps}^* \quad 2.59$$

Now,

$$\begin{aligned}
I\alpha|E_r|^2 &= \frac{1}{4} [p^* p^* + q^* q^*] & 2.60 \\
&= \frac{1}{4} [a \cdot a^* \cdot A^2 + a \cdot b^* \cdot AB + b \cdot a^* \cdot AB + b \cdot b^* \cdot B^2 \\
&\quad + a \cdot a^* \cdot B^2 + a \cdot b^* \cdot BC + b \cdot a^* \cdot BC + b \cdot b^* \cdot C^2] \\
&= \frac{1}{4} [a \cdot a^* (A^2 + B^2) + (AB + BC)(a \cdot b^* + b \cdot a^*) \\
&\quad + b \cdot b^* (B^2 + C^2)]
\end{aligned}$$

Only the term with $e^{i\phi}$ and $e^{-i\phi}$ would give rise to magneto-optical signals. So, we only going to take consideration of those terms.

Let's assume,

$$\begin{aligned}
I_1 &= 2 \cdot [(A^2 + B^2)(r_{pp} \cdot r_{ps}^* \cdot e^{i\phi} + r_{ps} \cdot r_{pp}^* \cdot e^{-i\phi}) & 2.61 \\
&\quad + (AB + BC)(r_{pp} \cdot r_{ss}^* \cdot e^{i\phi} + r_{ps} \cdot r_{sp}^* \cdot e^{-i\phi} \\
&\quad + r_{sp} \cdot r_{ps}^* \cdot e^{i\phi} + r_{ss} \cdot r_{pp}^* \cdot e^{-i\phi}) \\
&\quad + (B^2 + C^2)(r_{sp} \cdot r_{ss}^* \cdot e^{i\phi} + r_{ss} \cdot r_{sp}^* \cdot e^{-i\phi})]
\end{aligned}$$

We have $\frac{r_{ps}}{r_{pp}} = \theta_k + i\eta_k$ so that if we just take real terms for the intensity

$$\begin{aligned}
I_1 &= 2 \cdot |r_{pp}|^2 \cdot [(A^2 + B^2)(2\theta_k \cdot \cos\phi + 2\eta_k \cdot \sin\phi) & 2.62 \\
&\quad + (AB + BC)(2\cos\phi + \text{smaller terms ...}) \\
&\quad - (B^2 + C^2)(2\theta_k \cdot \cos\phi - 2\eta_k \cdot \sin\phi)] \\
I_1 &= 2 \cdot |r_{pp}|^2 [(A^2 - C^2)(2\theta_k \cdot \cos\phi) + (A^2 + C^2)(2\eta_k \cdot \sin\phi) \\
&\quad + (AB + BC) \cdot 2\cos\phi]
\end{aligned}$$

The terms $\sin\phi$ and $\cos\phi$ can be expanded into Bessel functions $J_n(x)$ of the order 1:

$$\sin\phi = \sin(\delta_0 \cdot \sin(\omega t)) = 2J_1(\delta_0) \cdot \sin(\omega t) + \dots \quad 2.63$$

$$\cos\phi = \cos(\delta_0 \cdot \sin(\omega t)) = J_0(\delta_0) + 2J_2(\delta_0) \cdot \cos(2\omega t) + \dots \quad 2.64$$

Harmonic arises during polarization modulation technique. These harmonics are recorded using phase sensitive detector like lock in amplifier. Such that,

$$I_\omega = |r_{pp}|^2 \cdot 2\eta_k \cdot J_1(\delta_0) \quad 2.65$$

$$I_{2\omega} = |r_{pp}|^2 (\cos^4\theta - \sin^4\theta) \cdot 2\theta_k \cdot J_2(\delta_0) + |r_{pp}|^2 \cdot 2 \cdot J_2(\delta_0) \cos\theta \sin\theta \quad 2.66$$

$$I_{DC} = \frac{1}{2} |r_{pp}|^2 (1 + J_0(\delta_0) \cdot \sin(2\theta + 2\theta_k)) \quad 2.67$$

Where I_{DC} , I_ω and $I_{2\omega}$ are the dc and ac intensities. The dc intensity is the intensity of the light reflected off or transmitted through the sample. The 1ω intensity, and the 2ω intensity are the modulated intensities that are modulated at the PEM's modulator frequency and its harmonic. DC intensity is measured using multimeters and the AC is measured using lock-in amplifiers.

The equations 2.65, 2.66 and 2.67 are similar to expression in W. Bas Zeper [33] for I_ω (2.66) and $I_{2\omega}$ (2.67). If one assumes θ to be small then equation 2.66 becomes,

$$\begin{aligned} I_{2\omega} &= |r_{pp}|^2 (\cos 2\theta) \cdot 2\theta_k \cdot J_2(\delta_0) + |r_{pp}|^2 \cdot J_2(\delta_0) \sin 2\theta \quad 2.68 \\ &= |r_{pp}|^2 J_2(\delta_0) \cdot \sin(2\theta + 2\theta_k) \end{aligned}$$

The extension of this polarization modulation for Kerr measurements incorporating multiple interference effect for our dual beam MO set-up is given precisely in chapter 3.

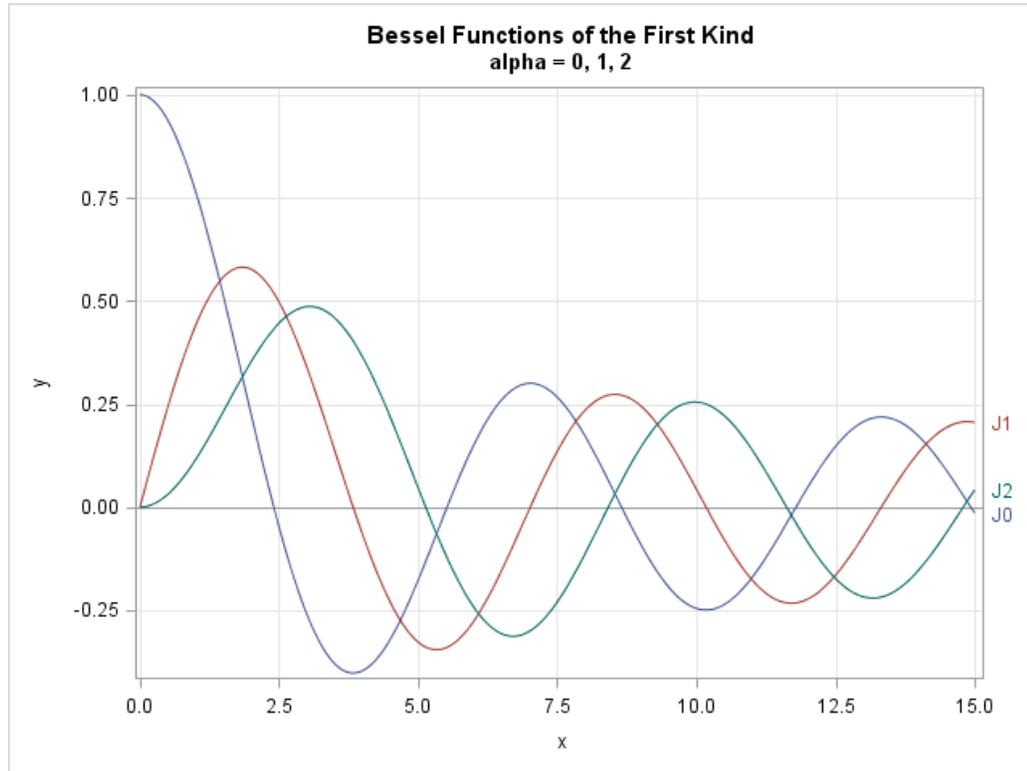


Figure 2.14 Bessel functions $J_0(x)$, $J_1(x)$, $J_2(x)$

The figure 2.14 above shows the Bessel functions of 1st kinds i.e. $J_0(x)$, $J_1(x)$, $J_2(x)$ and their nature. x is the argument of the Bessel function.

2.6 Apparatus for Dual MOKE Measurements

For dual beam MO study, a He-Ne laser beam (632.2 nm) is used as a light source. The optical components are an aluminum mirror, a Polaroid sheet polarizer, a quarter wave plate, a Glan-Taylor prism (MGTY515, Karl Lambrecht) mounted in a Newport URS-75 Servo motor stage, a single axis photo-elastic modulator (PEM-90) or a double axis photo-elastic modulator (PEM-100) from Hinds instruments, and photo detectors. The

PEM and its Jones matrix are already described in section 2.2. This section elaborates the Glan-Taylor prism, and the Wollaston prism as polarizer and analyzer. The section will also elaborate the He-Ne laser light, and the photo detectors as well as the noise source in the photo detectors.

2.6.1 Polarizer and Analyzer

This thesis used Glan-Taylor prism for polarizer and Wollaston prism as an analyzer. The Glan-Taylor polarizer was made by Karl Lambrecht Corporation model MGTYS15. They are made from optical calcite, which exhibits strong birefringence over a wide wavelength range [30]. They can be used at shorter wavelengths than cemented prisms with the spectral transmission range being from the ultraviolet to the near infrared (about 300 ~ 2500 nm). The extinction ratio of the Glan-Taylor prisms is better than 10^{-5} [34]. The ratio of the intensities of the minor principal transmittance to the major principal transmittance defines the extinction ratio. These principal transmittances happen at the orientations of the polarizer that causes the resulting intensity to be the maximum or minimum. The transmittance is maximum when the polarizer is oriented at 0 or 180 degrees and a min at 90 or 270 degrees. Calcite prisms shows birefringence and transmission down to around 214nm [35, 36]. The birefringent calcite has different refractive indices for both vertical linearly polarized and horizontal linearly polarized light. Only the vertical component of the light will transmit through the crystal while the horizontal component will be totally, internally reflected as it reaches the air gap. The opaque, the black surface that holds the crystal absorbs the reflected component of light. In an experiment the transmitted intensity follows the Malus cosine-square law when

polarized light is normally incident on an air spaced Glan-Taylor polarizing prism. The figure 2.15 below shows the Glan-Taylor prism.

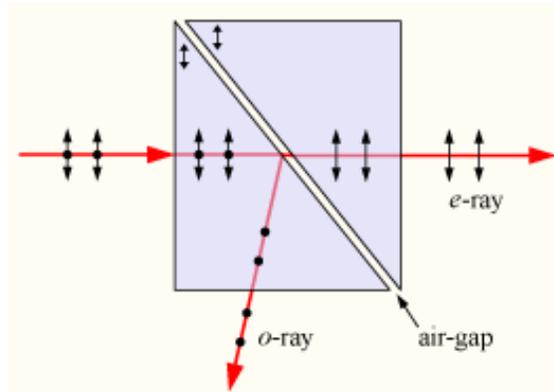


Figure 2.15 Glan-Taylor Prism [49]

For the analyzer the Glan-Taylor prism is replaced by a Wollaston Prism in the original setup. A Wollaston Prism of model WP10 from ThorLabs was used for this thesis project. A Wollaston prism polarizer consists of two right angle prisms made of a uniaxial crystal such as calcite, which is commonly used for Wollaston prisms [37]. The two pieces of uniaxial crystal are oriented such that the crystal axes are perpendicular to each other. Horizontal linearly polarized light propagates in the extraordinary index of refraction (n_e) in the first section and is refracted into the ordinary index of refraction (n_o) in the second section. Vertical linearly polarized light undergoes the opposite refraction and the two polarization states are thus separated. It allows for different dimensions in all three directions. Figure 2.16 below shows the Wollaston prism with two optical axis that are perpendicular to each other. Both beams created by using a Wollaston prism as a beam splitter are high quality linearly polarized beams and are polarized perpendicular to each other.

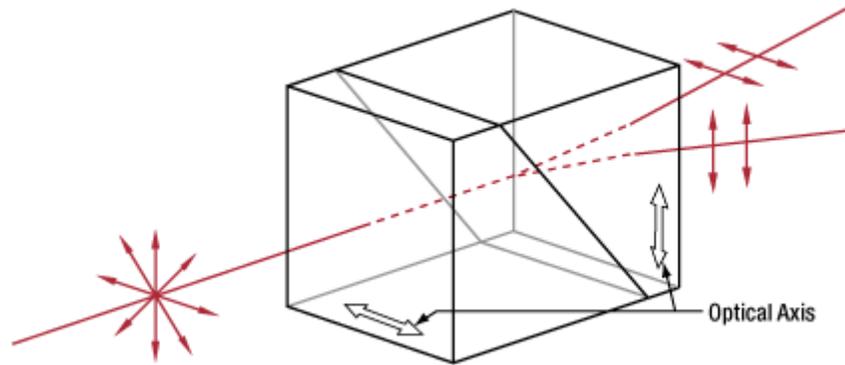


Figure 2.16 Wollaston prism [50]

2.6.2 Light Source

The light source used for this thesis project is an intensity stabilized linearly polarized He-Ne laser. A He-Ne laser consists of a hollow tube filled with 90 percent He and 10 percent Ne gases and fitted with inward-facing mirrors at the ends of the cavity [38]. The combined pressure of the two gases is approximately 1 Torr (1/760 atmospheres). A He-Ne laser works by exciting Neon atoms in the gas. The 632.8 nm optical light emitted by the laser is generated in the process when the Neon atoms decay from an excited state to an ordinary state. Helium and Neon are noble gases containing only one atom per molecule. Consequently, the states of a Helium and Neon molecule are relatively simple. The different states of a Ne molecule correspond to the different orbitals that electrons that surround the Ne atom. Radiation striking the Neon atoms causes the electrons circling these atoms to jump from one orbital to another [39]. An electrical discharge created by strong electric fields ionizes the He gas. Helium in its lowest energy state has an electron configuration of $1s^2$. After the ionized He^+ atoms recombine with their electrons some of the Helium atoms end up in the $1s2s$ -singlet state. Once in this state,

the He atoms are forbidden from spontaneously making radiative transitions to lower energy states by quantum selection rules.

However, an excited He atoms can decay through collisions with other atoms. The purpose of The He atoms are to act as a power source for the Ne atoms, kicking them up into an excited state. If an excited He atom collides with a Ne atom, there is a finite probability that during the time over which the two atoms are in close proximity with each other, the excited He atom can transfer its energy to the Ne atom. This requires that there is a vacant excited state for the Ne atom to jump to. Fortunately, Neon has an excited state whose excitation energy nearly matches the excitation energy of the He atom.

2.6.3 Photo-Detectors

The photo-detectors used for this thesis projects are PDA-55 silicon photo detectors and PDA-100-A2 silicon photo detectors made by Thorlabs Inc. The maximum output of the PDA-55 is 10 volts for high impedance loads (5V for 50 Ω loads). The gain of the PDA-55 detectors is adjusted so that the measured signal level out of the detector is below 10 volts (5 volts with a 50 Ω load) to avoid saturation. For maximum linearity performance when measuring focused beams, fiber outputs, or small diameter beams, one should not exceed a maximum intensity of 10mW/cm² with either type of detector. Because of the finite gain-bandwidth performance common to all opamp circuits, the bandwidth of the PDA-55 goes down with increased gain settings.

The PDA-55 gain is adjusted using a small slotted screwdriver to turn the internal, gain-setting rotary switch. An access hole labeled GAIN is provided on the rear panel of the

detector for this purpose. The gain is set to 0 dB, when the slot is aligned counterclockwise as far as it will go. Each clockwise click of the switch increases the gain by 10dB. It is to be noted that to not use excessive force when adjusting the gain switch. The PDA-55 is switched on by the POWER toggle switch located on the rear of the optical sensor. The light to voltage conversion can be estimated by factoring the wavelength-dependent responsivity of the silicon detector with the transimpedance gain as shown below:

$$\begin{aligned} & \text{(E. g. output in volts / watt)} && 2.69 \\ & = \text{transimpedance gain (V/A) x responsivity (A/W)} \end{aligned}$$

Where transimpedance of the photo detector is the current to voltage converter and responsivity of the photo detector is the measure of the electrical output per optical input.

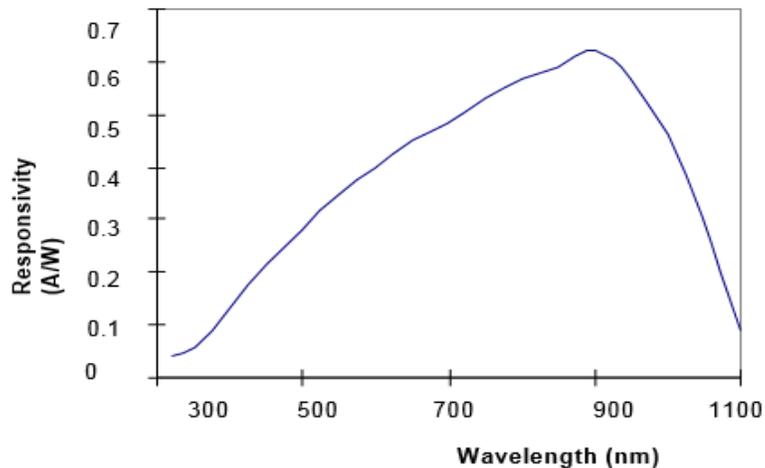


Figure 2.17 Detector Responsivity (PDA 55) [Thorlabs]

There are three contributions to the noise of the detector.

A. Johnson noise:

Johnson noise is generated by the thermal fluctuation. It is sometimes called thermal noise also. It results from the random motion of the electron in a conductor. The thermal

motion of electrons in a conductor give rise to a fluctuating voltage across the resistor.

This additional voltage is independent of the current flowing in the resistor. The Johnson noise is given by:

$$I_j = \left(\frac{4KBT}{R}\right)^{\frac{1}{2}} \quad 2.70$$

Where,

I_j = Johnson noise current.

K= Boltzmann constant (1.38e-23 JK).

T= Absolute temperature.

R= Resistance giving rise to noise, Ohms.

B= Bandwidth of the system, Hz.

B. Shot noise:

The term shot noise is derived from the fluctuations in the stream of electrons in a vacuum tube. Because of the random fluctuation of the electrons arriving at the anode, noise will be created. Shot noise is given by:

$$\text{Shot noise} \sim \sqrt{2eI_{ph}\Delta f} \quad 2.71$$

Where,

E= electronic charge.

I_{ph} = Photo current.

Δf = Band width of the system.

Shot noise is caused by two reasons:

I. Noise from dark-current in detector:

The intensity of photo-current can also contribute to shot noise. Double beam intensity

means double number of photons. The signal to noise ratio (SNR) increased by square root of 2 if one doubles the beam intensity.

II. Shot noise from the photo-current:

The intensity of photo-current can also contribute to shot noise. Double beam intensity means double number of photons. The signal to noise ratio (SNR) increased by square root of 2 if one doubles the beam intensity.

C. Detector noise:

The most common definition of the noise equivalent power (NEP) is the input signal power that results in a signal to noise ratio of 1 in a 1Hz output bandwidth. NEP is usually expressed in watts per square root of hertz and it expresses the sensitivity of the device. For photo-detectors it is desirable to have an NEP as low as possible, since a low NEP value corresponds to a lower noise floor and more sensitive detector. Low NEP is beneficial because even at higher input signal, it will lead to lower noise characteristic in the output signal. The Detector Noise equivalent power (NEP), Transimpedance, Responsivity, noise, signal to noise ratio for active area for different detectors from Thorlabs are tabulated below.

Table 1 NEP, Transimpedance, Responsivity, noise, signal to noise ratio for active area for different detectors from Thorlabs Inc. under different noise setting of lock ins.

Detector	NEP (Watt per square root of hertz)	Trans-impedance (Volt/Amp)	Responsivity (Ampere/Watt)	Noise (Volt/Square root Hertz)	S/N ratio per active area.
min sensitivity PDA-55	1.00E-11	7.50E+03	0.6	6.75E-08	1.04E+07 Used for thesis.
max sensitivity PDA-55	4.00E-12	7.50E+05	0.6	2.70E-06	2.59E+05
APD-130	2.00E-13	5.00E+04	25	3.75E-07	1.87E+06
PDA-100(20 dB)	3.36E-12	7.50E+03	0.72	3.10E-08	2.26E+07
PDA-100(10 dB)	6.75E-12	2.38E+03	0.72	1.98E-08	3.54E+07
PDA-36 (10 dB)	5.80E-12	2.38E+03	1.9	1.65E-08	4.24E+07
PDA-36 (20 dB)	3.40E-12	7.50E+03	1.9	3.05E-08	2.29E+07

D. 1/f noise:

In addition to Johnson noise there is a noise which arises from the fluctuation of resistance due to the current flowing through the resistor. This noise has the $1/f$ spectrum and cause the measurement extremely difficult at lower frequency. Most electronics has $1/f$ noise. It is not so relevant for MOKE setup as measurements are made at the modulation frequency where there is little $1/f$ noise.

3. DUAL BEAM DETECTOR TECHNIQUE

In the double beam detector technique, a Wollaston prism is used in place of the 2nd polarizer. So as the laser beam passes through the Wollaston prism, the beam is split into two beams and falls on two separate silicon detectors as shown in the figure below.

A He-Ne laser beam (632.2 nm) is used as a light source. The optical components are an aluminum mirror, a quarter wave plate, a Glan-Taylor prism (MGTY515, Karl Lambrecht) mounted in a Newport URS-75 Servo motor stage, a single axis photo-elastic modulator (PEM-90) or double axis photo-elastic modulator (PEM-100) from Hinds instruments, the sample, a Wollaston prism mounted in a Newport URS-75 Servo motor Stage and two Thorlabs PDA-55 photo detectors all mounted on top of a vibration isolation table. The PEM-90 is mounted horizontally on a non-magnetic optical post that can be rotated by a computer controllable Newport URS-75 servo motor stage to change the PEM tilt angle with respect to the laser beam. All three motorized stages have encoders on them with a resolution of 0.5 mdegrees. The PDA-55 Thorlabs photo detectors include pre-amplifiers. Their outputs are monitored by a 5 GHz/s-50 MHz Tektronix scope (TBS 1052B EDU). The sample is placed in between the poles of an electromagnet powered by a 100-watt Kepco power supply and furnished with a Hall probe. The maximum field that can be applied to the sample is +/-3400 Oersted. A PC running a LabVIEW program is used for data acquisition and to control the PEM tilt angle, the magnetic field, and the Polarizer and Analyzer angles. External triggering is used to guarantee that both lock-in amplifiers and multi-meters sample the detector signal at exactly the same time [40]. The horizontal linearly polarized light of the laser is converted into circularly polarized light by the quarter wave plate, so the light incident on

the polarizer is close to circularly polarized. The polarizer converts the state of polarization to linearly polarized light. This light passes through a single axis Hinds Photo-elastic modulator (PEM-90) or a double axis photo-elastic modulator (PEM-100). The beam transmitted through (or reflected by) the sample is split into two high quality beams that leave the prism at +/- 7 degrees. At 5 inches behind the Wollaston prism, the diverging beams are made parallel again by two optical wedges before they enter the detectors. Note that the Wollaston prism, wedges, and detectors are mounted together in a Newport URS75 high-resolution optical rotation stage which allows to rotate all components of the detector unit simultaneously. This motorized rotation stage is mounted on a manual stage that allows us to translate (two axes perpendicular to the beam, i.e. X and Y and tilt (θ_x , θ_y , and θ_z) the Wollaston prism with respect to the laser beam. A schematic diagram of the analyzer-detector unit is shown in figure below. A photo of the realized unit is also shown in Figure 3.1 below.

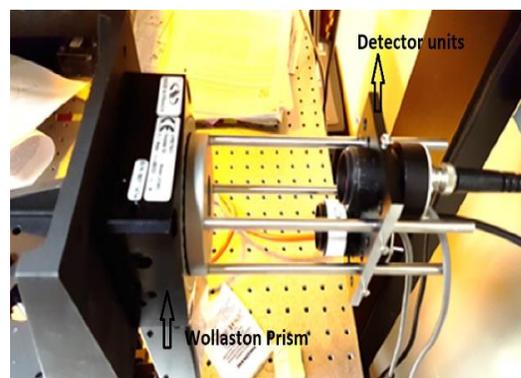
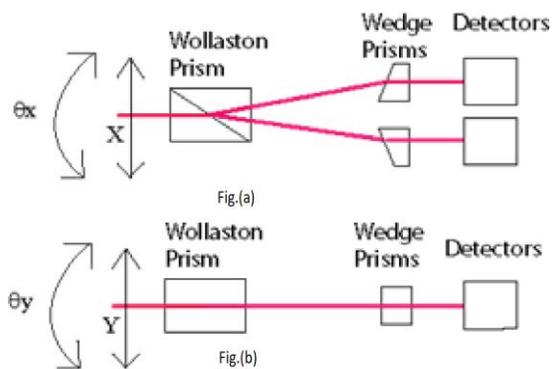
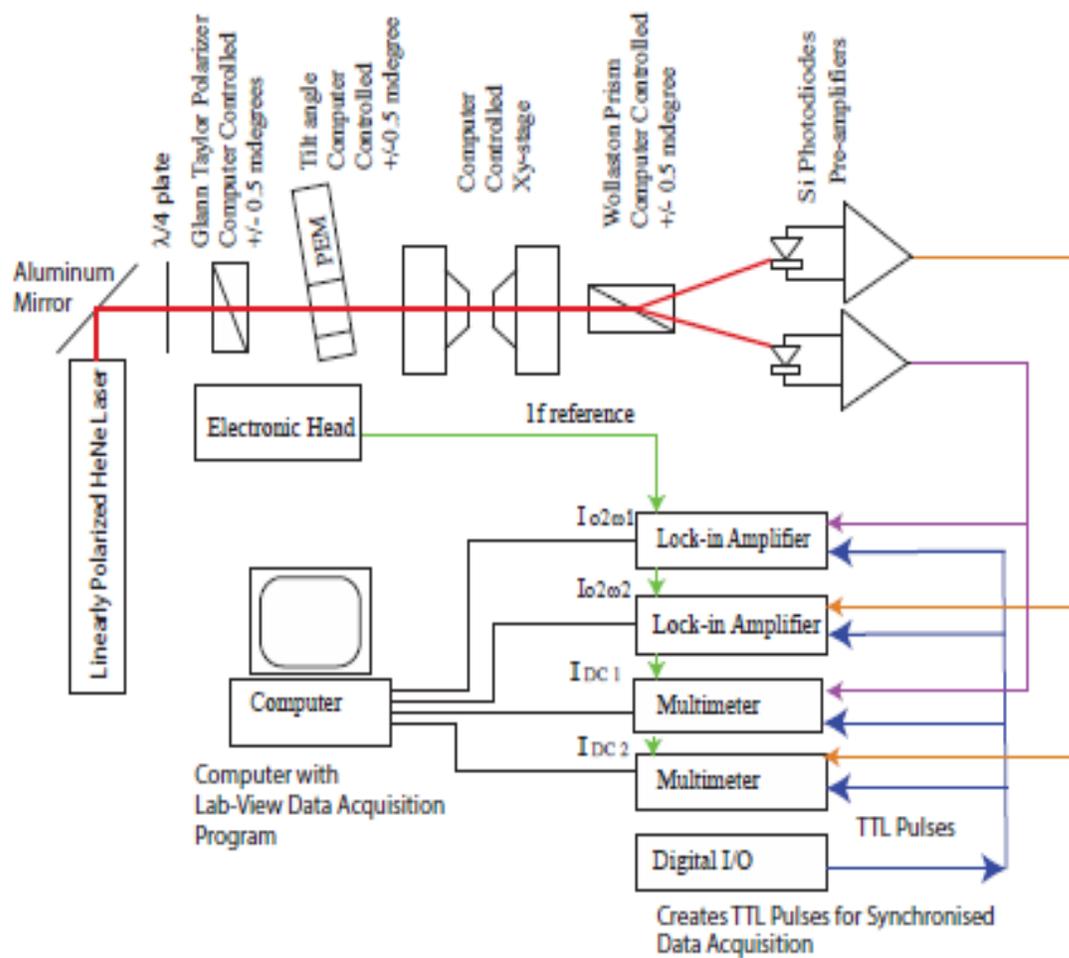


Figure 3.1 Dual Beam Detector Magneto Optical Kerr Set-Up

The figure 3.1 above shows the schematic diagram of the dual beam MO setup on top and analyzer detector unit on bottom left and the schematic diagram of the analyzer detector unit on bottom right. The entire assembly containing the stepmotors, Wollaston prism, wedges, detectors and alignment unit is referred to in this thesis as the analyzer-detector unit.

3.1 Optics Alignment of Dual Beam MOKE Setup

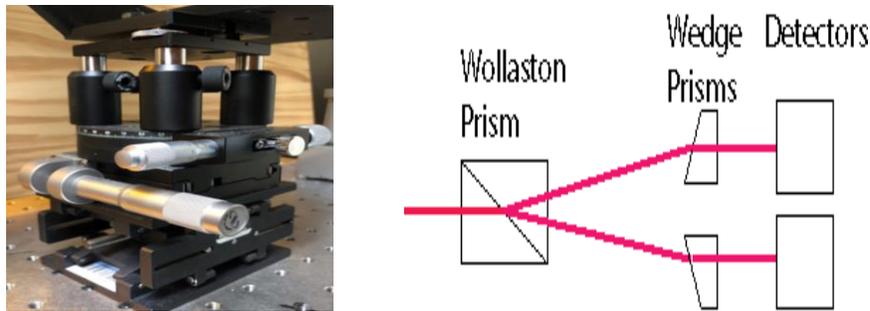


Figure 3.2 Stages used and Schematic diagram on two detector MOKE analyzer detector unit

The alignment of the detector-analyzer unit is crucial and has a huge impact on the measured signals. It is important that the angle between the beam reflected from the sample and the analyzer is independent of the analyzer angle. As there is a small angle between the rotation axis of the Wollaston prism and the surface normal of the Wollaston prism, it is not sufficient to adjust the analyzer-detector unit so the beam reflected of the Wollaston prism is parallel with the beam reflected of the sample. To allow for the alignment of the analyzer-detector unit, the unit was placed on an opto-mechanical mount that allows for the unit to be translated in both the x direction and y direction (perpendicular to the beam) and to be tilted in both the x, y, and z-directions. In order to

align the setup using, the following alignment recipe was put together:

The polarizer was first set at 45 degrees and the analyzer at 0 degrees to be able to observe the reflections of both split beams on the detectors. The translational stages of the analyzer-detector unit (see fig 3.2 left) are used to align the Wollaston prism with the laser beam that comes from the sample, so it is incident exactly at the center of the Wollaston prism. Next both detector units are covered by paper and the beam reflected from the Wollaston prism is aligned with the incident beam by tilting the stage. A small silicon coupon can be used as a mirror to double check whether the beam hits both the detector units at the center. Corrections necessary are made by adjusting the distance between the detectors and the Wollaston prism or by tilting the analyzer detector unit perpendicular to the beam. This coarse alignment of the setup is checked by rotating the analyzer from 0 to 180 degrees to check for constant DC signals on both detectors at 0 and 180 degrees. A small difference in intensity of 10 to 20 millivolt can still be observed because of a slight misalignment of the Wollaston prism in the rotation stage.

The rotation axis of the prism is not perfectly aligned with the surface normal of the prism. To correct for this and optimize the alignment, first the DC signals on channel 1 is recorded as a function of the tilt angle (θ_x) for 0- and 180-degrees analyzer orientation. The intersection of the two channel 1 curves typically results in the optimum alignment. The other tilting axis (θ_y) is adjusted in a similar way. So, the intensity is recorded for channel 2 as a function of the y-tilt, i.e. θ_y , at both 90 and 270 degrees. Then the y-tilt is adjusted to the intersection of both curves, i.e. the θ_y for which the intensity at 90 degrees and 270 degrees analyzer orientation give the same dc intensity on channel 2. After the alignment procedure, the DC signals on detector 1 differ less than 0.2 % for 0- and 180-

degrees orientation of the analyzer-detector unit. As both detectors have a slightly different quantum efficiency, the angle dependence of the intensity of one of the channel is adjusted in the software. Both DC channels also show a small offset of approximately 10 mV in each channel. This offset was subtracted by the data acquisition software as well.

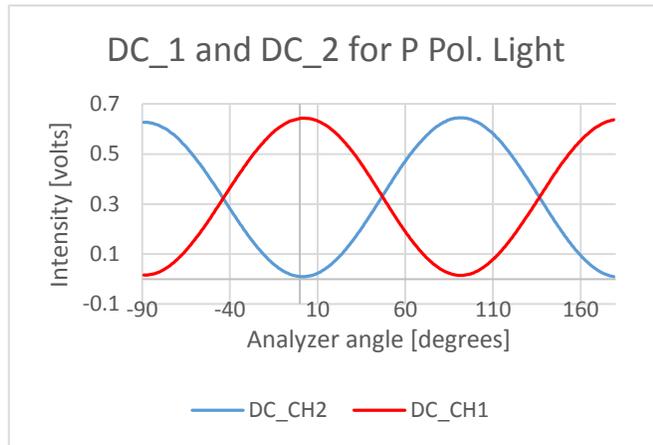
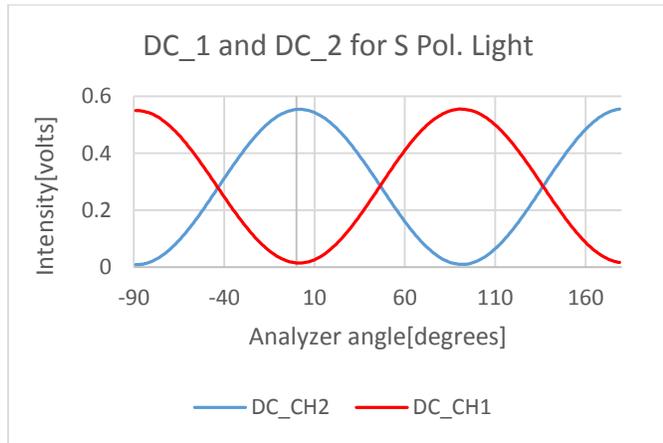


Figure 3.3 The DC signals on both channels as a function of analyzer for a P-polarized (top) and an S-polarized (bottom) incident beam

The alignment of the setup was checked by measuring the DC and 2ω signals as a function of the analyzer angle. Figure 3.3 shows the intensity of channel 1 and 2 as a function of the analyzer angle for p and s-polarized light using PEM-90 and PDA-55 detectors. No samples were placed and the retardation depth of the PEM was kept at a quarter wavelength. The polarizer was kept at 45 degrees. The p-polarized light in this setup is parallel to the long length of the PEM and thus for a tilted PEM parallel to the plane of incidence of the PEM. The detected sinusoidal angle dependence directly follows from Malus's law. The installation of the alignment fixtures on the analyzer-detector unit appeared to be crucial for obtaining these curves. Figure 3.4 shows the 2ω signals of channel 1 and channel 2 as a function of the analyzer angle for two different PEM tilt angles. A small phase shift was observed after tilting the PEM by 0.4 degrees which is due to the slight change of the transmitted laser beam direction with PEM tilt angle. Also, the 2ω signal appears to vary sinusoidally with the analyzer angle and is proof of a good alignment of the setup. A minimum is observed at 45 degrees, i.e. parallel to the polarization plane of the light incident on the PEM.

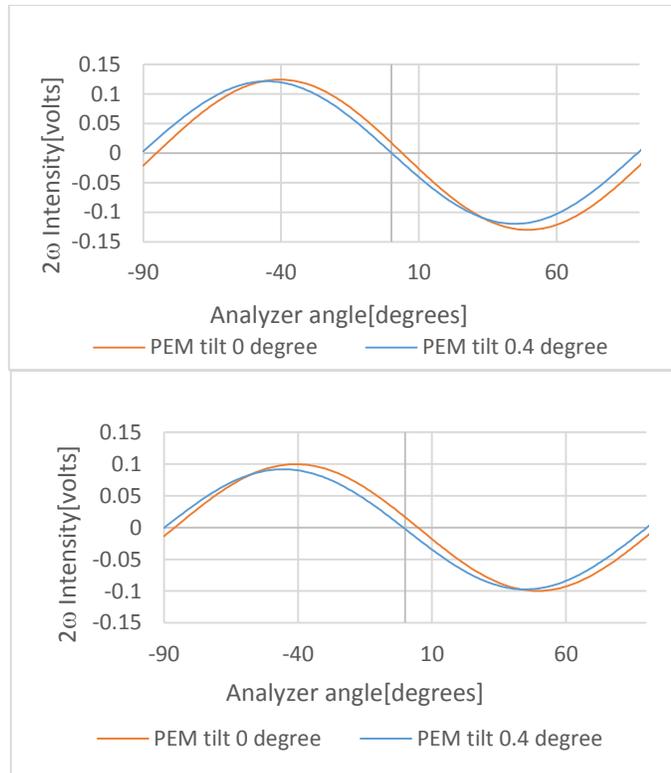


Figure 3.4 Signal for channel 1, (top) and channel 2, (bottom) as a function of the analyzer angle for PEM tilt 0 and 0.4

3.2 Multiple Interference Effects in PEM

When PEMs are used with lasers as light sources, the modulated interference effects may occur [41]. Interference occurs due to the reflection of light at the surfaces of the PEM optical head. These multiple times reflected beams will interfere and will also modulate the laser beam intensity. The modulation of both the thickness of the PEM and the refraction index of the PEM causes the optical path length to be modulated with the PEM's modulation frequency. Since the modulated interference frequencies are exactly

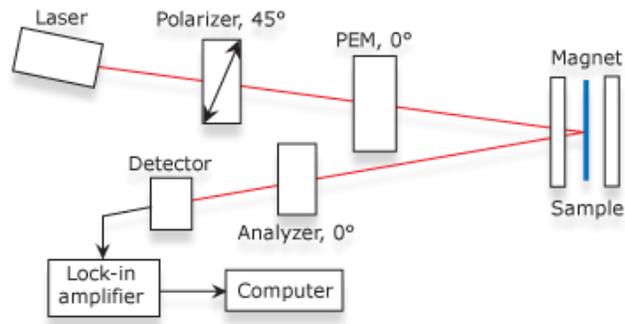


Figure 3.5 Single detector MOKE using PEM

the same as the polarization modulation frequencies being studied, they can be very troublesome [41, 42]. The interference effect in the PEM thus leads to large offset to DC, 1ω , and 2ω detector signals as shown by Talukder [43]. As these offsets depend strongly on wavelength, beam direction, and PEM thickness, the single beam setup becomes highly sensitive to temperature variations. The effect of the multiple interference effect can be avoided by using a PEM with special anti-reflection coating or using a PEM that has an optical prism that has a trapezoid shape [44]. It is also possible to tilt the PEM and use an aperture to remove the beams that travel through the PEM multiple times, although that also influences the PEM's optical aperture.

Gemeiner et al. incorporated the multiple interference effects in the PEM, in the Jones matrix description of a single beam setup [43]. Calculations were done for two separate cases: (1) circular birefringence and (2) circular dichroism. Using their results to calculate the signals for a dual beam setup suggests that the difference signal between both channels is independent of the Kerr rotation and also the multiple interference effect offset cancels out in the difference channels. Here the calculation is repeated with another

approach assuming the sample shows both MO Kerr effects (Kerr rotation and Kerr ellipticity), and it is shown that only the multiple interference effect cancels out when subtracting both signal channels. The Kerr rotation signal in the difference signal is double the Kerr rotation signal of a single axis setup.

Including the multiple interference effect and assuming that the PEM has a thickness that is an integer times the wavelength, the PEM Jones matrix is given by:

$$M = \begin{bmatrix} e^{i\theta\frac{1}{2}} (1 + r^2 e^{i\phi}) & 0 \\ 0 & e^{-i\theta\frac{1}{2}} (1 + r^2 e^{-i\phi}) \end{bmatrix} \quad 3.1$$

Where 'r' is the internal Fresnel reflection coefficients for the fused quartz to air interface in the optical head of the PEM. The components of the Jones matrix of equation 3.1 consist of two terms: one can consider the two terms originate from the interface of the beam that one times travel through the PEM and the beam that passes 3 times through the PEM's optic head. For the beam that goes 3 times through the PEM's optic head:

$$e^{i\theta\frac{1}{2}} (1 + r^2 e^{i\phi}) \quad 3.2$$

For the beam that goes infinite times through the PEM's optic head the 2nd term in above equation becomes:

$$(1 + r^2 e^{i\phi} + r^4 e^{2i\phi} + r^6 e^{3i\phi} + \dots) \quad 3.3$$

Since $r^2 e^{i\phi} \ll 1$, using sum of geometric series and expanding using binomial theorem gives,

$$(1 + r^2 e^{i\phi} + r^4 e^{2i\phi} + r^6 e^{3i\phi} + \dots) = \frac{1}{1 - r^2 e^{i\phi}} = 1 + r^2 e^{i\phi} \quad 3.4$$

The equation 3.4 shows that this Taylor approximation is similar to just adding the beam that directly goes through the modulator and beam that goes three times through the modulator and avoiding any higher order terms. The above Jones matrix for the modulator assumes that the 1st and 4th matrix element are complex conjugate of each

other.

The PEM Jones matrix $\begin{bmatrix} T_p' & 0 \\ 0 & T_s' \end{bmatrix}$ satisfies $T_p' = T_s'^*$ if no multiple interference effect is included for (PEM-100). If the multiple interference effect is included, the Jones matrix only satisfies $T_p' = T_s'^*$ if $\delta_1 = 2m\pi$ where m is an integer. The most general Jones matrix for the PEM that includes the multiple interference effect is given by (see also section 2.3):

$$\begin{pmatrix} e^{\frac{i\phi_p}{2}}(1 + r^2 e^{i\phi_p}) & 0 \\ 0 & e^{\frac{i\phi_s}{2}}(1 + r^2 e^{i\phi_s}) \end{pmatrix}. \quad 3.5$$

Where,

$$\phi_p = \delta_{0p} \sin(\omega t) + \delta_1 \quad 3.6$$

$$\phi_s = -\delta_{0s} \sin(\omega t) + \delta_1 \quad 3.7$$

So,

$$T_p' = e^{\frac{i\delta_0 \sin(\omega t)}{2}} e^{\frac{i\delta_1}{2}} (1 + r^2 e^{i\delta_1} e^{i\delta_0 \sin(\omega t)}) \quad 3.8$$

And

$$T_s' = e^{\frac{-i\delta_0 \sin(\omega t)}{2}} e^{\frac{i\delta_1}{2}} (1 + r^2 e^{i\delta_1} e^{-i\delta_0 \sin(\omega t)}) \quad 3.9$$

So we can write the Fresnel matrix as:

$$e^{\frac{i\delta_1}{2}} \begin{pmatrix} e^{\frac{i\delta_0 \sin(\omega t)}{2}} & 0 \\ 0 & e^{\frac{-i\delta_0 \sin(\omega t)}{2}} \end{pmatrix} \begin{pmatrix} (1 + r^2 e^{i\delta_0 \sin(\omega t)}) & 0 \\ 0 & (1 + r^2 e^{-i\delta_0 \sin(\omega t)}) \end{pmatrix} \quad 3.10$$

The first term $e^{\frac{i\delta_1}{2}}$ has no influence on intensity. The first square matrix is the same as the PEM's Jones matrix for the case with no multiple interference effect. So, the effect of the multiple interference effect is the last square matrix. So, including the multiple interference effect in the PEM gives a Jones matrix for which $T_p' \neq T_s'^*$.

Note that using equation 3.10 instead of equation 3.1 will make the calculation very complicated. If δ_1 is a multiple integer of 2π , the multiple interference offset is maximum in $I_{2\omega}$ and zero in I_ω . If δ_1 is a half integer of π , the multiple interference offset is maximum in I_ω and zero in $I_{2\omega}$. So, to estimate the largest multiple interference offset here 3.1 is used for the PEM's Jones matrix. It is furthermore assumed that $\phi_p = \phi_s$, so a dual axis PEM is used:

So, the intensity signals falling on the detector can be written as $I \sim |E_r|^2$

$$\begin{pmatrix} E_{pr} \\ E_{sr} \end{pmatrix} = A.S.M.P. \begin{pmatrix} E_{pi} \\ E_{si} \end{pmatrix} = \frac{1}{2} \begin{bmatrix} \cos^2\theta & \cos\theta\sin\theta \\ \cos\theta\sin\theta & \sin^2\theta \end{bmatrix} \begin{bmatrix} r_{pp} & r_{ps} \\ r_{sp} & r_{ss} \end{bmatrix} \quad 3.11$$

$$\begin{bmatrix} e^{i\frac{\delta_0}{2}}(1+r^2e^{i\phi}) & 0 \\ 0 & e^{-i\frac{\delta_0}{2}}(1+r^2e^{-i\phi}) \end{bmatrix} \frac{1}{2} \begin{bmatrix} 1 & 1 \\ 1 & 1 \end{bmatrix} \begin{pmatrix} 1 \\ -i \end{pmatrix}$$

So, from the same procedure:

$$I_\omega = |r_{pp}|^2 \cdot \eta_k \cdot (2J_1(\delta_0) + 4r^2J_1(2\delta_0) + 2r^4J_1(3\delta_0)) \quad 3.12$$

And

$$I_{2\omega} = |r_{pp}|^2 (\cos^4\theta - \sin^4\theta) \cdot \theta_k \cdot [2J_2(\delta_0) + 4r^2 \cdot J_2(2\delta_0) \quad 3.13$$

$$+ 2 \cdot r^4 J_2(3\delta_0)]$$

$$+ |r_{pp}|^2 [2J_2(\delta_0) + 4r^2 \cdot J_2(2\delta_0)$$

$$+ 2 \cdot r^4 J_2(3\delta_0)] \cos\theta \sin\theta + |r_{pp}|^2 2r^2 J_2(\delta_0)$$

And

$$I_{DC} = \frac{1}{2} |r_{pp}|^2 [1 + J_0(\delta_0)(2r^2 + \sin 2\theta + 2\theta_k \cos 2\theta) \quad 3.14$$

$$+ J_0(2\delta_0)(2r^2 \cdot \sin 2\theta + 4r^2 \cdot \theta_k \cdot \cos 2\theta)]$$

Where I_{DC} is the dc current of the laser reflected off or transmitted in magnetic medium.

Note that there is no multiple interference offset in the I_ω term. So, for dual beam modulated technique:

For channel 1, $\theta = 0$

$$I_{DC1} = \frac{1}{2} |r_{pp}|^2 [1 + J_0(\delta_0)(2r^2 + 2\theta_k) + J_0(2\delta_0)(4r^2 \cdot \theta_k)] \quad 3.15$$

$$I_{1\omega1} = \frac{1}{2} |r_{pp}|^2 \cdot \eta_k \cdot [2J_1(\delta_0) + 4r^2 J_1(2\delta_0)] \quad 3.16$$

$$I_{2\omega1} = \frac{1}{2} |r_{pp}|^2 [2J_2(\delta_0)(2r^2 + 2\theta_k) + 2J_2(2\delta_0) \cdot 4\theta_k \cdot r^2] \quad 3.17$$

For channel 2: $\theta = 90$,

$$I_{DC2} = \frac{1}{2} |r_{pp}|^2 [1 + J_0(\delta_0)(2r^2 + 2\theta_k) + J_0(2\delta_0)(-4r^2 \cdot \theta_k)] \quad 3.18$$

$$I_{1\omega2} = \frac{1}{2} |r_{pp}|^2 \cdot \eta_k \cdot [2J_1(\delta_0) + 4r^2 J_1(2\delta_0)] \quad 3.19$$

$$I_{2\omega2} = \frac{1}{2} |r_{pp}|^2 [2J_2(\delta_0)(2r^2 - 2\theta_k) + 2J_2(2\delta_0) \cdot -4\theta_k \cdot r^2] \quad 3.20$$

Here r^4 terms were dropped as $r^2 \ll 0$.

Such that,

$$\Delta I_{DC} = \frac{1}{2} |r_{pp}|^2 [J_2(\delta_0) + 2r^2 J_2(2\delta_0) \cdot 4\theta_k \cdot r^2] \quad 3.21$$

$$\Delta I_\omega = 0 \quad 3.22$$

$$\Delta I_{2\omega} = \frac{1}{2} |r_{pp}|^2 [J_2(\delta_0) + 2r^2 J_2(2\delta_0) \cdot 8\theta_k] \quad 3.23$$

Discussion: The equations given by Talukder [43] in the case for just the multiple

interference effect with analyzer at 0 degrees are given as:

$$I_{DC} = E_0^2 e \left[c + \cos \left(a - a \frac{\phi_t^2}{2n_0^2} \right) J_0(b_p) \cos^2(\phi_p) \right] \quad 3.24$$

$$I_{0\omega} = E_0^2 e \left[2 \sin \left(-a \frac{\phi_t^2}{2n_0^2} \right) J_1(b_p) \cos^2(\phi_p) \right] \quad 3.25$$

$$I_{02\omega} = E_0^2 e \left[2 \cos \left(a - a \frac{\phi_t^2}{2n_0^2} \right) J_2(b_p) \cos^2(\phi_p) \right] \quad 3.26$$

Where ‘a’ is twice the PEM’s unstrained path length in radians. ‘b’ is twice the modulation of the PEM’s optical path length in radians. ϕ_p is the angle of polarizer. n_0 is the refractive index (unstrained) of fused silica (1.4569 at 632.8nm).

$$e = \frac{2t_{ga}t_{ag}t_{ga}^*t_{ag}^*r^2}{(1+r^4)^2} \quad 3.27$$

$$c = \frac{(1+r^4)}{2r^2} \quad 3.28$$

$t_{ag}(t_{ga})$ is the amplitude transmission coefficient for the air-glass (glass-air) interface, r is the amplitude reflection coefficients for the glass-air interface.

And the equations given by Gemeiner et al [44] for study of multiple interferences are given by:

$$\begin{aligned} I_{2\omega} = & +[2K \sin 2(\beta - \theta) J_2(G - H) \quad 3.29 \\ & + 2Kr^2 \cos 2C \{ 2J_2(2G) \cos^2(\beta - \theta) \\ & + 2J_2(2H) \sin^2(\beta - \theta) \\ & + \sin 2(\beta - \theta) (J_2(3G - H) + J_2(3H - G)) \}] \end{aligned}$$

$$\begin{aligned}
I = K\{1 - \Delta\chi J_1(G - H)\sin\omega t & \quad 3.30 \\
+ r^2[\cos 2\delta_1(J_0(2H) + J_0(2G)) & \\
+ 2\sin 2C(J_1(2H) + J_1(2G))\sin\omega t & \\
+ 2\cos 2C(J_2(2H) + J_2(2G))\cos 2\omega t\} &
\end{aligned}$$

The equation 3.30 is the measurement for circular dichroism (CD). Where,

$$C = \frac{2\pi n_0 e_0}{\lambda} \quad 3.31$$

$$G = \frac{\pi n_0 e_0}{\lambda} \left(n_0^2 q_{11} + \frac{2\sigma}{E} \right) P_m \quad 3.32$$

$$H = \frac{\pi n_0 e_0}{\lambda} \left(n_0^2 q_{12} + \frac{2\sigma}{E} \right) P_m \quad 3.33$$

The e_0 and n_0 respectively are the thickness and the refractive index of the modulator at rest. The q_{11} and q_{12} are the photo-elastic constants of the material. Sigma σ is the Poisson coefficient, β is the analyzer angle and θ is the Kerr rotation.

The equations 3.12, 3.13, and 3.14 are consistent with Talukder's equation. Note that for the derivation of equation 3.12, 3.13, and 3.14 it is assumed that there is no offset in the phase of the PEM. So, the retardation is described by

$$\phi = \delta_1 + \delta_0 \sin(\omega t) \quad 3.34$$

With $\delta_1 = 0$. This corresponds to $a=0$ in Talukder's equation. So, for $\eta_k = 0$, $\theta_k = 0$, and $a=0$. Both equations 3.12, 3.13, and 3.14 are same as the equations 3.24, 3.25, and 3.26.

The equations given by Talukder's can be now written as (equation 3.24, 3.25, and 3.26):

$$I_{DC} = E_0^2 e \left[c + \cos \left(\delta_1 - \delta_1 \frac{\phi_t^2}{n_0^2} \right) J_0(\delta_0) \cos^2(\phi_p) \right] \quad 3.35$$

$$I_{0\omega} = E_0^2 e \left[2 \sin \left(\delta_1 - \delta_1 \frac{\phi_t^2}{2n_0^2} \right) J_1(\delta_0) \cos^2(\phi_p) \right] \quad 3.36$$

$$I_{02\omega} = E_0^2 e \left[2 \cos \left(\delta_1 - \delta_1 \frac{\phi_t^2}{2n_0^2} \right) J_2(\delta_0) \cos^2(\phi_p) \right] \quad 3.37$$

The equations 3.12, 3.13, and 3.14 are also consistent with Gemeiner's 3.29, and 3.30. As no offset in the phase is assumed $C=0$ in equations 3.29, 3.30. Note that if $\eta_k = 0$ and $C=0$ equation 3.12 is similar to 1ω of equation 3.30. If $\theta_k = 0$ and $C=0$ equation 3.13 is similar to 2ω of equation equations 3.29. So, the multiple interference effect can cause an offset in ϕ . Note that $\phi = \delta_1 + \delta_0 \sin(2\pi ft)$ where δ_1 depends on the thickness of the modulator and the refraction index of the optical head and represents the optical path length of the beam as it travels one time through the unstrained crystal.

The equations given by Gemeiner can be now written as (equation 3.29 and 3.30):

$$\begin{aligned} I_{2\omega} = & + [2K \sin 2(\theta - \theta_k) J_2(\delta_{p0} - \delta_{s0}) \quad 3.38 \\ & + 2Kr^2 \cos 2\delta_1 \{ 2J_2(2\delta_{p0}) \cos^2(\theta \\ & - \theta_k) + 2J_2(2\delta_{s0}) \sin^2(\theta - \theta_k) \\ & + \sin 2(\theta - \theta_k) (J_2(3\delta_{p0} - \delta_{s0}) \\ & + J_2(3\delta_{s0} - \delta_{p0})) \}] \end{aligned}$$

$$\begin{aligned}
I = K\{ & 1 - \Delta\chi J_1(\delta_{p0} - \delta_{s0})\sin\omega t & 3.39 \\
& + r^2 \left[\cos 2\delta_1 \left(J_0(2\delta_{s0}) + J_0(2\delta_{p0}) \right) \right. \\
& + 2\sin 2\delta_1 \left(J_1(2\delta_{s0}) + J_1(2\delta_{p0}) \right) \sin\omega t \\
& \left. + 2\cos 2\delta_1 \left(J_2(2\delta_{s0}) + J_2(2\delta_{p0}) \right) \cos 2\omega t \right] \}
\end{aligned}$$

In general, $\delta_1 \neq 0$ will cause an offset in both the 2ω but still have an offset in 1ω signals. If δ_1 is a multiple of π the offset in the 1ω signal will become zero.

Note that, the δ_1 term contributes with the same sign in the p and s component of the light while they must have the same sign in the p and s component of light while the δ_0 term has opposite sign in both the s and p component. The T_s' and T_p' component of the PEM Fresnel matrix are no longer complex conjugate of each other if $\delta_1 \neq 0$.

Comparisons of Gemeiner's approach and the MATHCAD simulation is given in an appendix section B and C respectively.

3.3 Effect of residual stress in the PEM on retardation for the case without interference effect

In this section the effect of a residual strain in the PEM on the measured signals is analyzed. The calculation does not include the interference effect. The calculation was done to better understand how 1ω and 2ω signals vary with the modulation depth of the PEM. The birefringence of the PEM is assumed to result in an additional phase shift ϕ_x for just the x-component.

$$\begin{pmatrix} E_{pr} \\ E_{sr} \end{pmatrix} = A.S.M.P. \begin{pmatrix} E_{pi} \\ E_{si} \end{pmatrix} = \frac{1}{2} \begin{bmatrix} \cos^2\theta & \cos\theta\sin\theta \\ \cos\theta\sin\theta & \sin^2\theta \end{bmatrix} \begin{bmatrix} r_{pp} & r_{ps} \\ -r_{ps} & r_{ss} \end{bmatrix} \quad 3.40$$

$$\begin{bmatrix} e^{i\phi\frac{1}{2}}(e^{i\phi_x}) & 0 \\ 0 & e^{-i\phi\frac{1}{2}} \end{bmatrix} \frac{1}{2} \begin{bmatrix} 1 & 1 \\ 1 & 1 \end{bmatrix} \begin{pmatrix} 1 \\ -i \end{pmatrix}$$

Such that,

$$\begin{aligned} I = \frac{1}{2} |r_{pp}|^2 & [\cos 2\theta \cdot 2\theta_k \cdot (\cos\phi \cdot \cos\phi_x - \sin\phi \cdot \sin\phi_x) \quad 3.41 \\ & + 2\eta_k (\sin\phi \cdot \cos\phi_x + \cos\phi \sin\phi_x) \\ & + \sin 2\theta \cdot (\cos\phi \cdot \cos\phi_x - \sin\phi \cdot \sin\phi_x)] \end{aligned}$$

The calculation approach is similar to section 2.4 but,

$$\begin{aligned} I_\omega = |r_{pp}|^2 & [-2\theta_k \cdot \cos 2\theta \cdot \sin\phi_x \cdot J_1(\delta_0) + 2\eta_k \cdot \cos\phi_x \cdot J_1(\delta_0) \quad 3.42 \\ & - \sin 2\theta \cdot \sin\phi_x \cdot J_1(\delta_0)] \end{aligned}$$

$$\begin{aligned} I_{2\omega} = |r_{pp}|^2 & [2\theta_k \cdot \cos 2\theta \cdot \cos\phi_x \cdot J_2(\delta_0) + 2\eta_k \cdot \sin\phi_x \cdot J_2(\delta_0) \quad 3.43 \\ & + \sin 2\theta \cdot \cos\phi_x \cdot J_2(\delta_0)] \end{aligned}$$

This is without the multiple interference effect. Note that now both Kerr rotation and Kerr ellipticity can end up in the 2ω or 1ω components. ϕ_x can originate from the strain in the PEM, the strain in the sample and or the strain in the analyzer or polarizer prisms. It can be believed that the latter two effects are negligible since, we can extinguish the light by crossing analyzer and polarizer. To check if there is any strain in the substrate contributing, one can try to extinguish the intensity by switching off the PEM and crossing the polarizers.

3.3 LabVIEW Programing

National Instruments LabVIEW is a graphical programming language that has its roots in automation control and data acquisition. LabVIEW 2017 was used for the automation of the MOKE setup including data acquisition. The ESP300 Motion Controller to tilt polarizer, PEM and the analyzer-detector units. Two SR830 Lock in amplifiers were used to record the 2ω intensities and two HP3457A multimeters to record the DC intensities. The drivers and manuals of the Lock-in amplifiers, motion controller and Multimeters were used to create VIs to control the instruments. A new LabVIEW VI was created to control the PEM tilt angle by computer and employs a hand-shake environment for the control of the steptomotors.

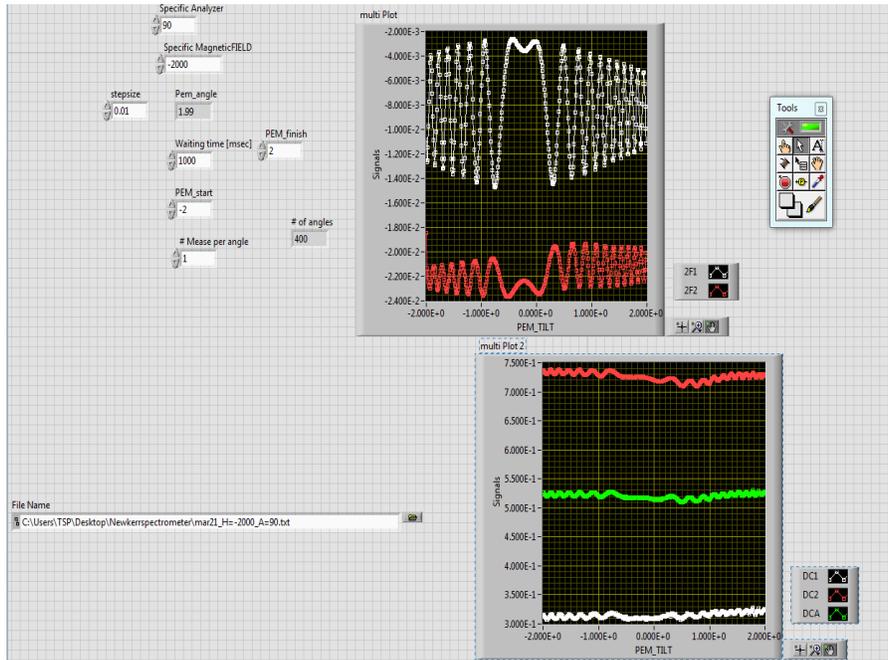


Figure 3.6 LabVIEW automation for Data Acquisition

The figure 3.6 above shows the LabVIEW graphical user-interface for the VI that is used to collect the MO data as a function of rotation of an optical component (i.e. polarizer, analyzer or PEM tilt angle).

3.4 Implementation of External Triggering

The external triggering technique is adopted to accumulate data from lock-in and multimeters at exactly the same moment in time. This is important if one wants to record the effect of the laser noise. The trigger inputs of the lock-in and multimeters are TTL type signals. The idea behind the implementation of the external triggering is the use of the internal RAM of the lock-in amplifiers and multimeters. The lock-in amplifiers and multimeters take measurements when triggered via BNC connectors applied to the rear of the instrument. The measurements values are stored in internal RAM in the instruments. The RAM then can be read by an external data processing system via a GPIB interface. Most oscilloscopes are equipped with a trigger circuit to start measuring when a certain condition occurs in the input signal. Triggering is used both for capturing unique signal events and to stabilize the display of repetitive signals. Without triggering, signals are measured and displayed at random times. The trigger circuit has several settings which are divided into instrument trigger settings and channel trigger settings.

A continuous, nonperiodic pulse train was provided to the rear EXT-TRIG terminals of the multimeters and lock-in amplifiers. All four pieces of equipment were set so each pulse would trigger the measurement of a reading that is stored in the internal memory of each instrument. More specifics can be found in appendix A.

ADigitalI/Ounit was used to create the nonperiodic TTL pulses trains that trigger the lock-in

amplifiers and multimeters. After the measurements are completed the collected data are read out from the buffer of the multimeters and lock-ins. Both the lock-in amplifiers and the multimeters are set at 300 milli second time constant. This time constant reflects the integration time of the measurements. The longer the integration time the smoother the signals.

For MOKE signals recording, SR830 Lock in Amplifiers from Stanford research and HP 3457A multimeters were used. MO signals are typically of the order of few milli-volts.

The most widely used method of measuring a low-level optical signal is to apply a modulation to the light source and then recovering the signal at the modulation frequency. The modulation frequency for PEM is the resonance frequency that oscillates the birefringent piezoelectric transducer. These are inside PEM's electronic head and the lock-in amplifier uses a modulation frequency as a frequency-selective technique. The optical signal stimulating the experiment and thus falling on the optical detector generates an electrical current which can be measured by the lock-in. For MOKE signals recording, the time constant of 300 milliseconds is used for both lock-ins and multimeters for data sampling.

3.5 Noise of Laser on the Detectors

It is true that the detector noise also effects the Kerr intensity signals recorded in lock-ins. To measure the detector noise, MO optic setup is first aligned to have the same detector intensity on both channels. The same intensity is obtained by putting the analyzer-detector unit at -4.65 degrees. The PEM is turned off during the process, as one would want no modulation of laser light falling on two detectors. Lock-in amplifier is

used to monitor the detector noise. For this process lock in was kept at 50 micro volt sensitivity and an integration time constant of 100 milliseconds. Both the detector channels have the noise of 120 Nano-volts. The difference signal, however, has a noise of 60 Nano-volts. It is to be noted that the detector intensity as seen from HP3457 multimeter was 284 milli-volts, was obtained by putting an aperture narrowed using pinhole. As the laser was blocked from entering into the detector the noise of individual channels was varying from (50-60) Nano-volts. The difference signal, however, has the noise of (35-40) Nano-volts. This later was the dark noise. The results were factor 3 more with the long cable setup. For this purpose, short cable path to Lock-ins was used.

3.6 Test Stability of PEM-100

Similar to wave plates, PEM are known to be very sensitive to temperature. A slight change in the lab temperature will result in small thickness change of its optical prism. The later has an effect on its retardation but also on the Fabry-Perot interference effect. Commercial PEMs are sometimes placed in a small furnace whose temperature is kept constant with a PID controller. For example, the PEM-ATC of Hinds instruments. Temperature variations of the PEM can result from two sources: (1) change of the lab temperature; (2) change of PEM temperature by self-heating after a change of the retardation setting of the modulator. To study the latter effect the step up and step-down responses of the PEM-100 were measured.

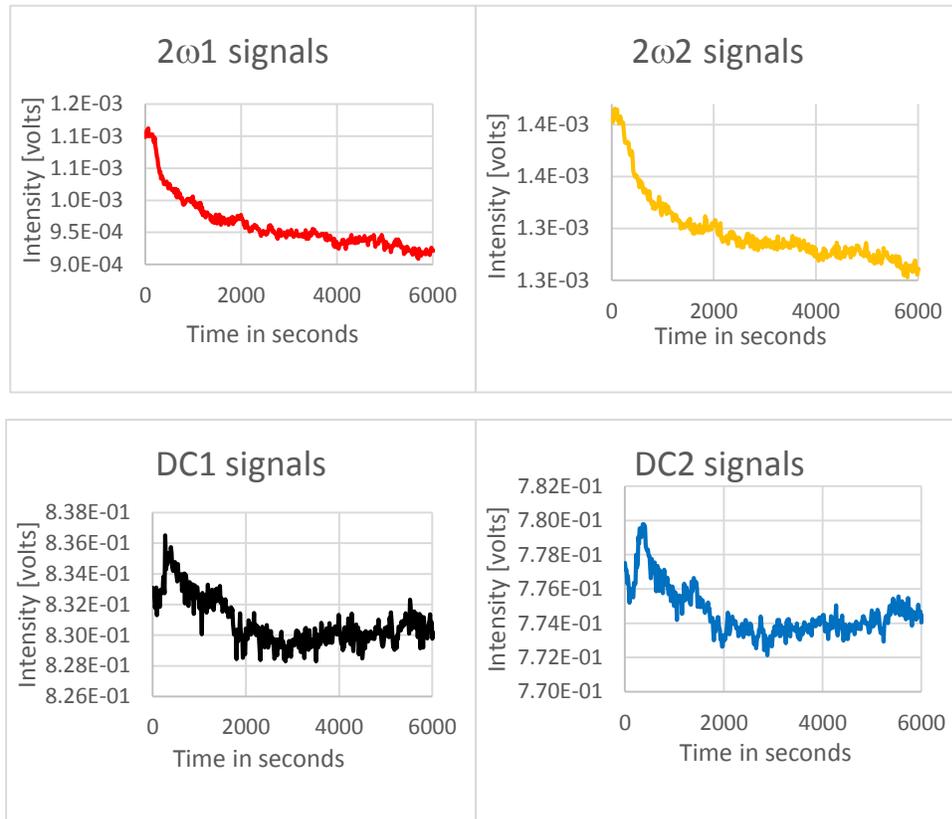


Figure 3.7 Step down response of PEM-100, Stepping down from 3.14 to 1.571 wavelength retardation, PEM tilt at 5.5 degrees, and with PDA-55 detector

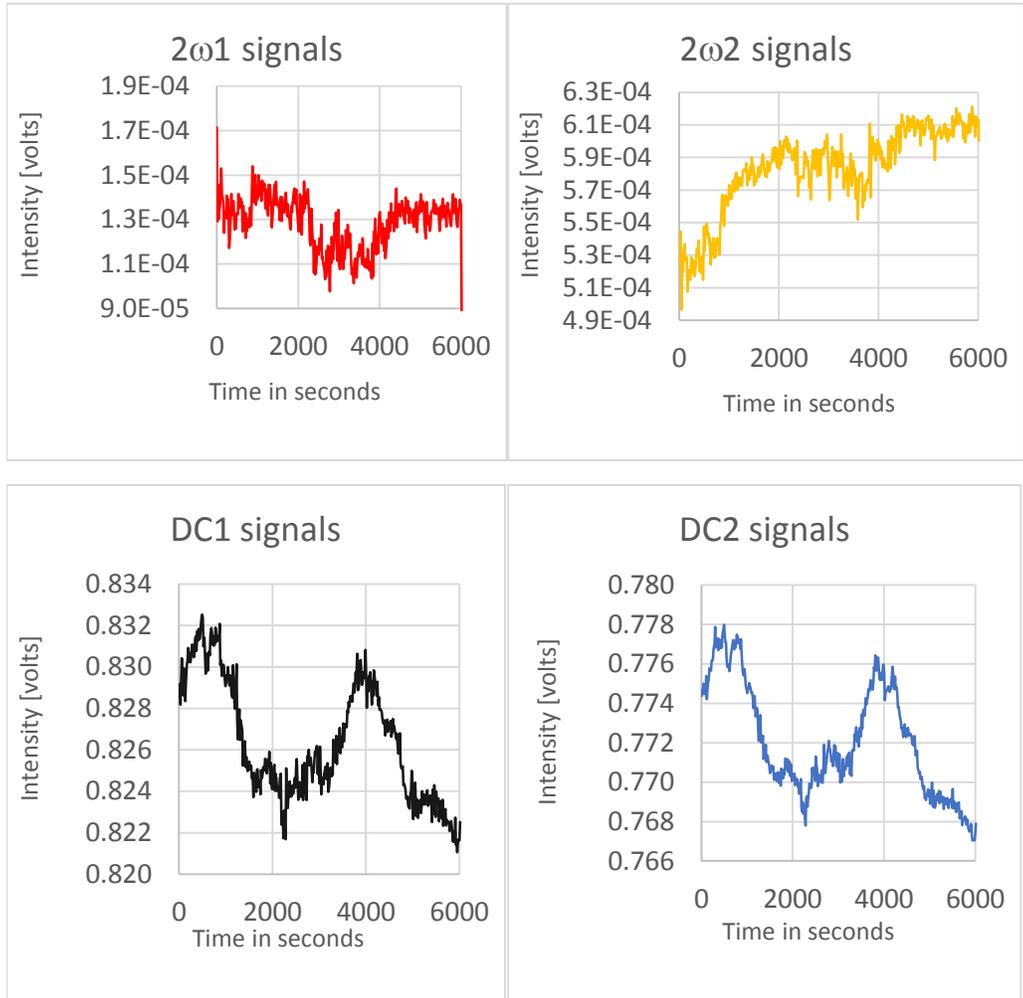


Figure 3.8 Step up response of PEM-100, Stepping down from 3.14 to 1.571 wavelength retardation, PEM tilt at 5.5 degrees, and with PDA-55 detector

At perpendicular incidence of PEM-100:

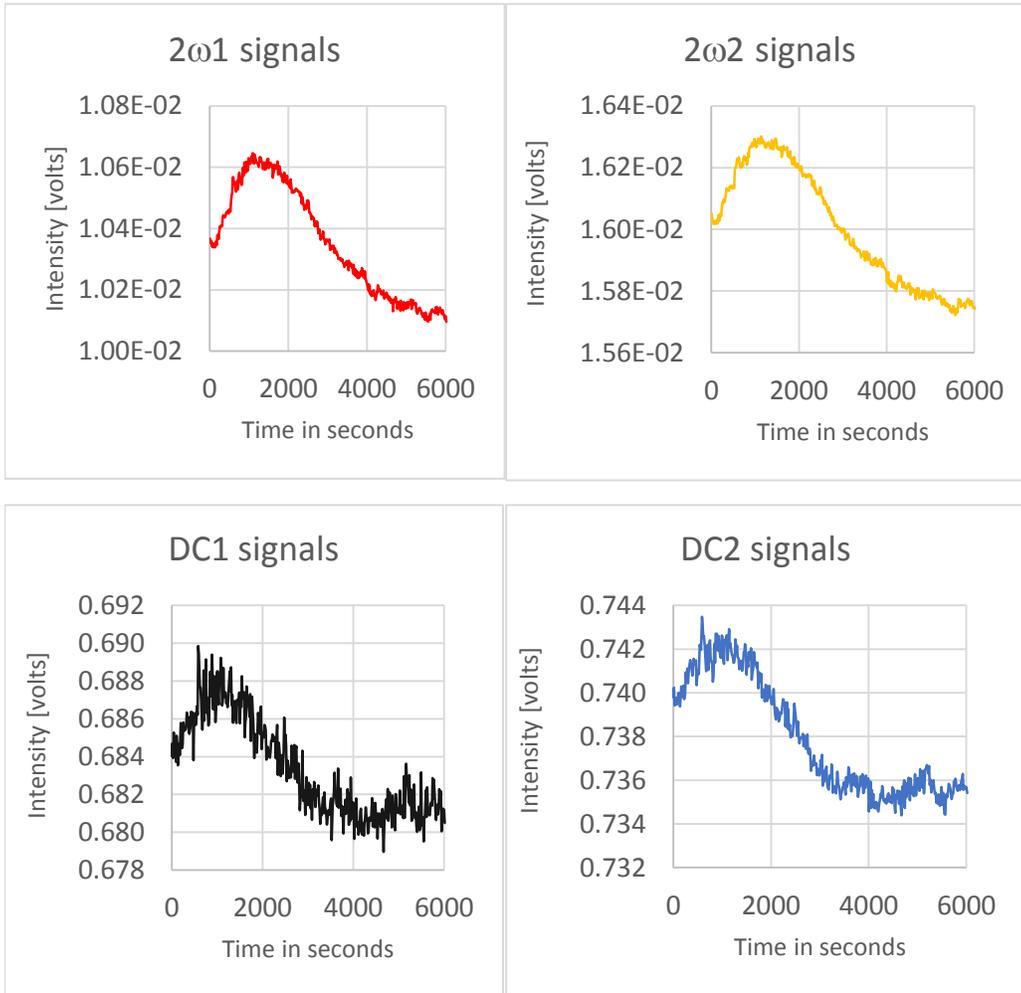


Figure 3.9 Step down response of PEM-100, Stepping down from 3.14 to 1.571 wavelength retardation, PEM tilt at 0 degrees, and with PDA-55 detector

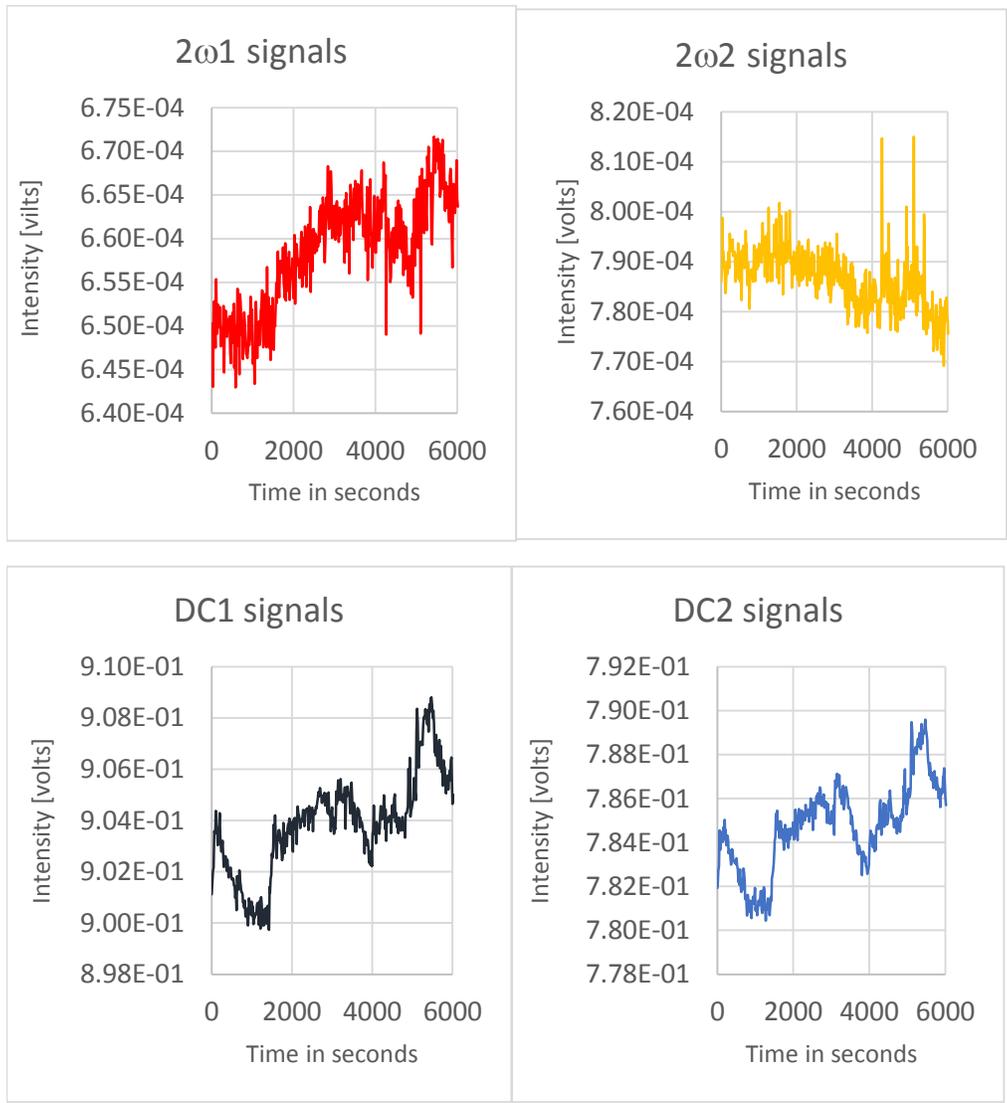


Figure 3.10 Step up response of PEM-100, Stepping down from 3.14 to 1.571 wavelength retardation, PEM tilt at 0 degrees, and with PDA-55 detector

Figure 3.7 and figure 3.8 show the step down and step up response of the measured 2ω and DC intensity for sudden change of the PEM's retardation depth from half wavelength

to quarter wavelength respectively. Measurements were done for two different PEM angles 5.5 and 0 degrees. The figures 3.7 and 3.8 shows the step down and step up response at higher PEM tilt of 5.5 degrees. The figures 3.9 and 3.10 shows the step down and step up responses of the PEM at perpendicular incidence. The 2ω as well as Dc intensity seem to decrease in time while the PEM's retardation depth step down. A decrease of 175 micro volt is observed for $2\omega_1$ channel and a decrease of 148.5 micro volts (uv) is observed for $2\omega_2$ channel. The dc intensity on both channels decrease by 2 milli volts (mv) while stepping down of PEM. Similarly, during stepping down (figure 3.7) of the PEM's retardation depth at a PEM tilt of 5.5 degrees, the $2\omega_1$ intensity decreases by 263 uv and the $2\omega_2$ increases by 88 uv. Both DC intensity decrease by 8 millivolts while stepping up at larger PEM tilt angle.

At the normal incidence of the PEM-100 the stepping down response of retardation depth causes the decrease in intensity for the 2ω signal by 20 mv and the dc intensity falls down by 4.5 mv on both channels. However, the stepping up response at normal incidence of the PEM cause a gain in 2ω intensity by 14 uv for both channels. The dc intensity increases by 2 mv on both channels while stepping up when the beam is at normal incidence to the PEM.

The gain or loss in dc and ac detector signals are related to the sudden change of the modulation voltage and the change in modulator's gradual temperature change. The observed changes are believed to originate from contributions caused by Fabry-Perot interference in the PEM's optical head. Fabry-Perot interference occurs when highly reflecting surfaces are mounted parallel to each other.

4. EXPERIMENTAL RESULTS AND DISCUSSION

This chapter will summarize the important results using the Dual Beam Modulated MO Set-Up. The tests as a function of polarizer and analyzer angles, the PEM tilt, and test as a function of retardation are presented in this section. Also, the signal to noise ratio for each result will be presented in this section. The noise was calculated from the standard deviation from 31 independent measurements. The integration time was set to 300 milliseconds (msec). The time between two consecutive measurements were at least one time constant. All the tests that are done with or without glass substrate and field of ± 3400 Oe will be presented for the dual beam modulator (DBM) MOKE set-up. The results will be compared with the single detector (SD) MOKE set up technique.

4.1 Test as a Function of Analyzer Angle

After the alignment of the detector-analyzer unit as described in the previous chapter, the 2ω and DC signals were measured as a function of the analyzer angle. During the experiment the PEM-90 was kept at normal incidence i.e. 0 degrees, the polarizer at 45 degrees and the PEM retardation depth was kept at a quarter wavelength retardation depth. Experiments were performed with the PDA-55 and the PEM-90. Variation of 2ω intensity and DC intensity as a function of the analyzer angle for each channel are presented below.

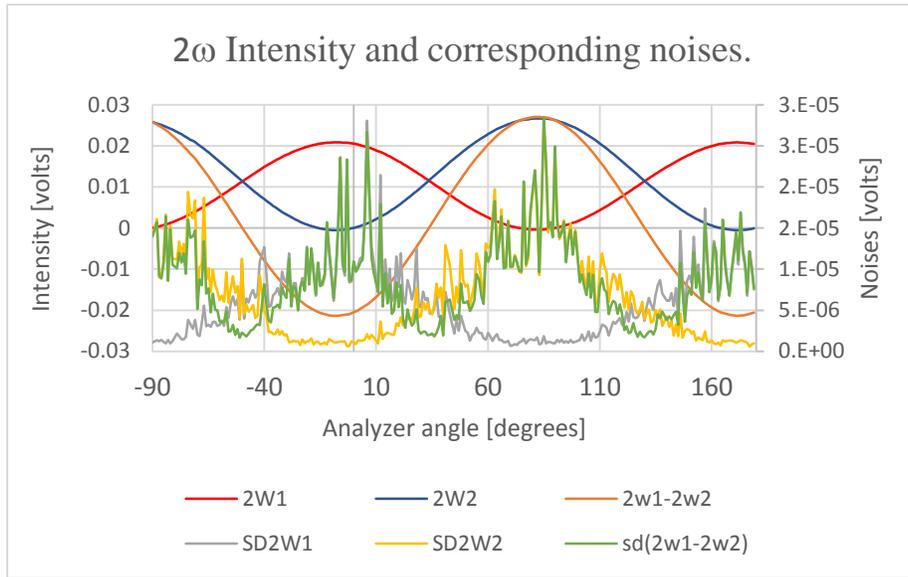


Figure 4.1 2ω intensity signals and corresponding noises as a function of analyzer angles for PEM-90, PDA-55, and quarter wave retardation

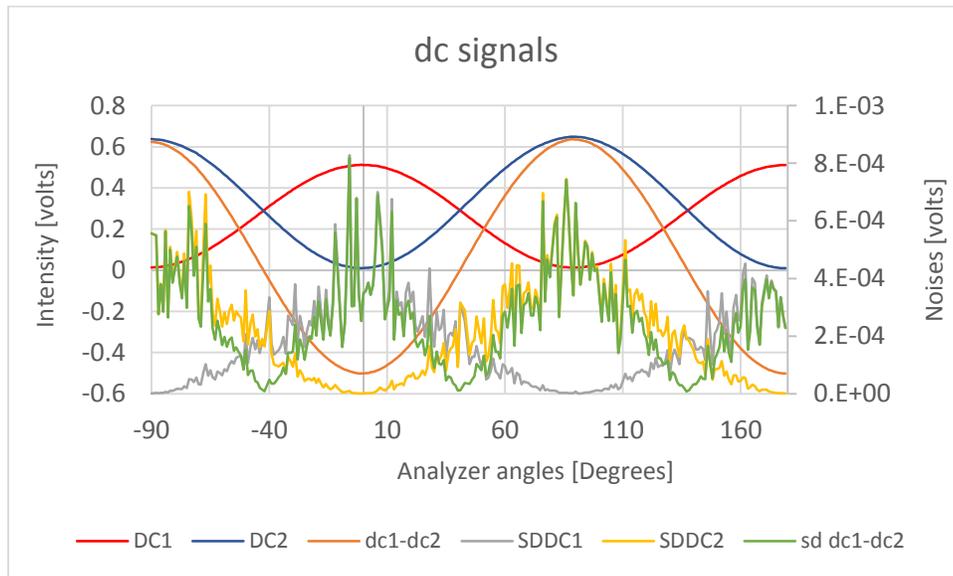


Figure 4.2 DC intensity signals and corresponding noises as a function of analyzer angles for PEM-90, PDA-55, and quarter wave retardation

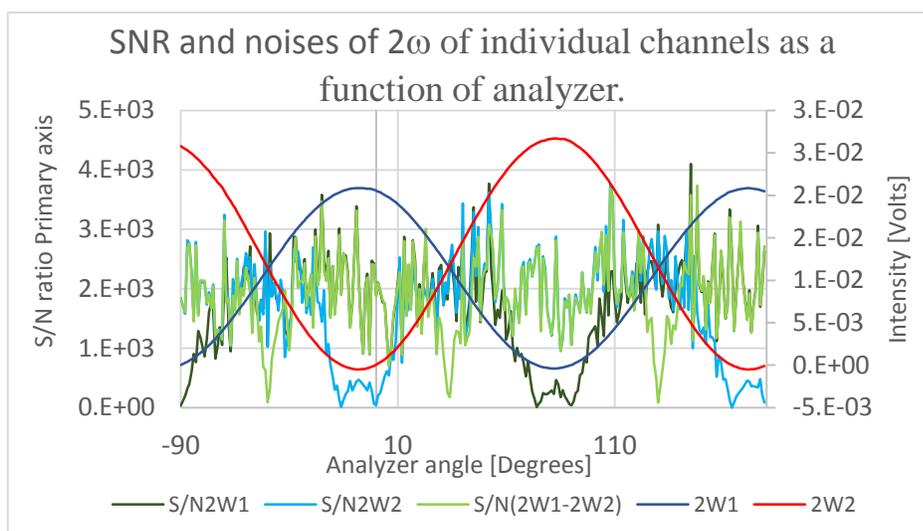


Figure 4.3 Test as a function of Analyzer with PEM-90, PDA-55 detectors

The figure 4.1, 4.2, and 4.3 above show the corresponding 2ω intensities of each channel and the noise level, DC intensity and corresponding noise level, and SNR of individual channels and difference channel. The noise level for each channel is measured from standard deviation of all the data that were read out from the RAM of the lock in and multimeters. The experiment was done without field and glass slide sample. The measured signals of both dc and 2ω follow Malus law. Both the 2ω and the DC signal vary sinusoidal with the analyzer angle and the channel 1 signals seem to be maximum when the channel 2 signal is minimum and vice versa. The maximum of the DC signal for channel 1 is exactly at 0 degrees and the maximum DC signal for channel 2 at 90 degrees. The maximum of the 2ω signal for channel 1 is at -6 degrees, so slightly shifted with respect to the DC signal. Note that the correlation between the 2ω and dc noise signals for both channels are dependent on the analyzer angle and was strongest when the signals on both channels were equal to each other. This is further illustrated in the

zoomed plots shown in Fig. 4.4. The first two terms of the multiple interference term of equation 3.38, i.e.

$$\begin{aligned}
 I_{2\omega} = & +[2K\sin 2(\theta - \theta_k)J_2(\delta_{p0} - \delta_{s0}) \\
 & + 2Kr^2\cos 2\delta_1 \{2J_2(2\delta_{p0})\cos^2(\theta - \theta_k) \\
 & + 2J_2(2\delta_{s0})\sin^2(\theta - \theta_k) \\
 & + \sin 2(\theta - \theta_k) (J_2(3\delta_{p0} - \delta_{s0}) + J_2(3\delta_{s0} - \delta_{p0}))\}]
 \end{aligned}$$

Proportional to $\cos 2C$ is the $\cos^2(\theta - \theta_k)$ and the third term is a $\sin 2(\theta - \theta_k)$ term. So, the phase depends on the magnitude of both terms. For the PEM-90, G (δ_{p0}) is less or greater than -H (δ_{s0}). So, a phase shift can be there.

The correlation between the 2ω and DC noise signals for both channels are dependent on the analyzer angle and is strongest when the signals on both channels are equal to each other. This is further illustrated in the zoomed plots shown in Fig. 4.4 below which show that the noise of the different signal is minimum for the analyzer angle where the signals in both channels are equal. This happens at 34 degrees for the 2ω signal and at 40 degrees for the dc signal.

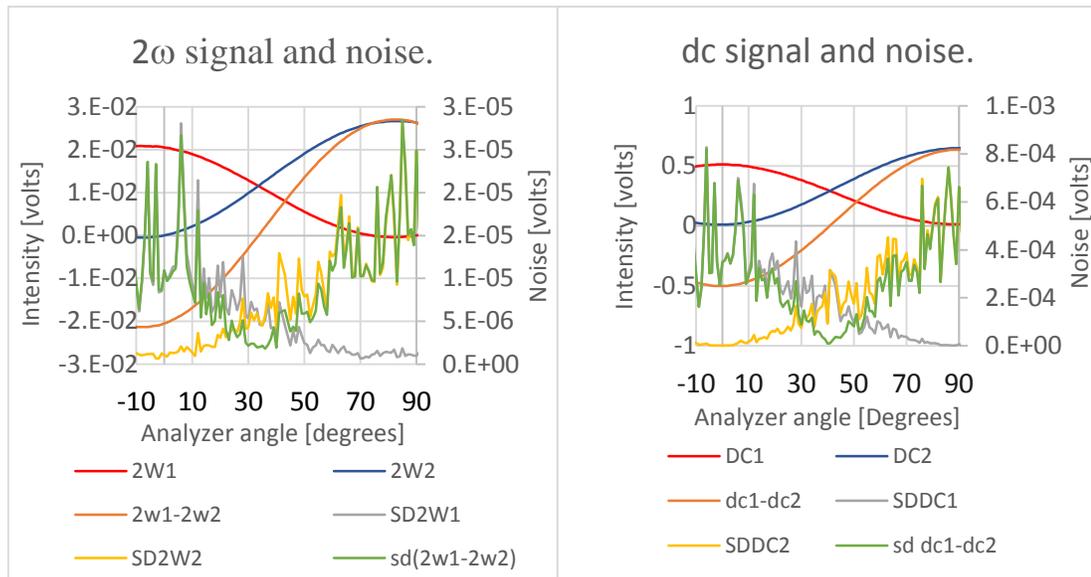


Figure 4.4 Zoomed in plots of 2ω and dc signals of each channel and their corresponding noises as a function of the analyzer angle

4.2 Test as a Function of PEM Tilt Angle

The DBM-MOKE setup was tested by changing the PEM tilt angle. The experiments were done by putting the retardation depth to a quarter wave length. The experiments were done with both the PEM-90 and PEM-100 modulators and PDA-55 and PDA-100-A2 detectors. The signal to noise ratio of the 2ω signals of each channel and of the difference of both channels were measured.

A. Test with PEM-90 and PDA-55 detector:

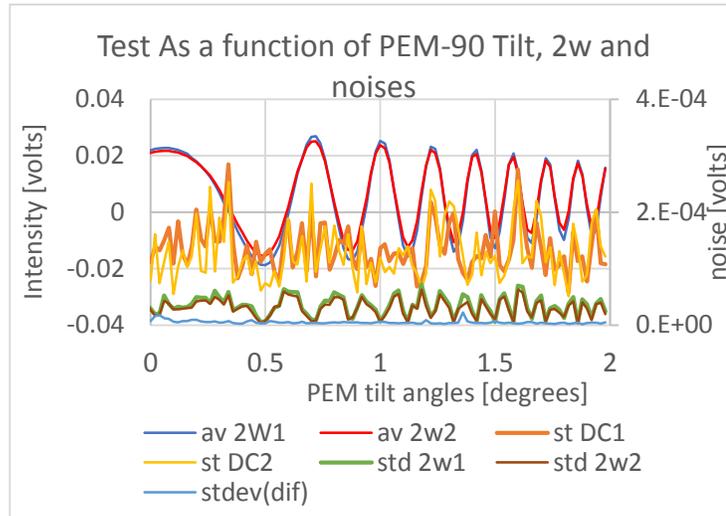


Figure 4.5 Signals as a function of PEM tilt, PEM-90, PDA-55, no glass substrate, no field, and quarter wave retardation

The above figure 4.5 shows the average 2ω signal of each channel, and the corresponding DC noise and 2ω noise. These measurements were done using a PEM-90 and the PDA-55 detectors. The experiment was performed with no field (applied from Gaussmeter) and no glass slide substrate. The 2ω noises of both channels are strongly correlated. Also, the DC noises of both channels are correlated. The 2ω noise follows the pattern that when the 2ω intensity signals have a low slope the noise is low. This suggests that or the wavelength stability or the pointing stability of the laser significantly contributes to the observed noise. The noise of the difference channel was calculated in excel after using a scaling factor to equalize the signal in both channels. The individual signals were made equal using a multiplication factor and standard deviation is also calculated using the

multiplication factor from all the data read from the RAM of the lock in amplifiers. The S/N ratio of the individual 2ω channel is found to be 29 dB. Note that it is assumed that the signal is the maximum of the 2ω intensity, and the noise is the average of standard deviation. Using the same definition as above the S/N ratio of difference 2ω channel is found to be 37 dB. A factor 5 reduction of the noise for the two channel case was measured. Note that the signal of the difference channel goes up a factor 2, resulting in a factor 10 improvement in S/N for the DB-MOKE compared to the SB-MOKE. Note that to obtain this improvement of a factor 10 the signal of both channels needed to be equalized before they are subtracted.

A similar approach was followed for the DC signal: in excel the DC signals of both channels were subtracted after equalizing them. The decrease of the noise for the difference channel was only a factor, resulting in a S/N ratio improvement of a factor 4 for the DC signal. The more noise of the difference DC signal is caused by the larger measurement bandwidth of the multimeters compared to the lock-in amplifiers. The DC intensity and the DC noise are shown in the figure 4.6 as a function of the PEM tilt angle.

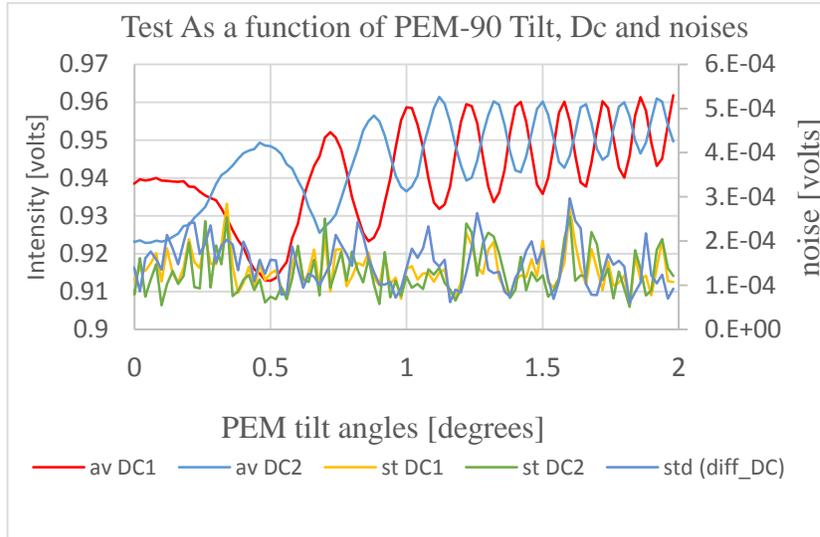


Figure 4.6 DC signals as a function of PEM tilt, PEM-90, PDA-55, no glass substrate, no field, and quarter wave retardation

The DC noise signals are very strongly correlated see figure 4.6. From the dc signals as a function of the PEM angle, the signal to noise ratio of a single channel is estimated to be 40 dB. This number is an upper limit for the noise of the laser as the DC signal is directly proportional to the laser intensity. The noise of the STP901 laser is 0.2% according to the specs. The noise measured from the data is 0.15% which is within the specs of the laser. The noise in the difference signal is slightly larger which is counter intuitive. Note that for this results the signals of both channels were no equalized. The signal to noise ratio found from the data for the difference channel is 36 dB. So, it is important to equalize the DC signals.

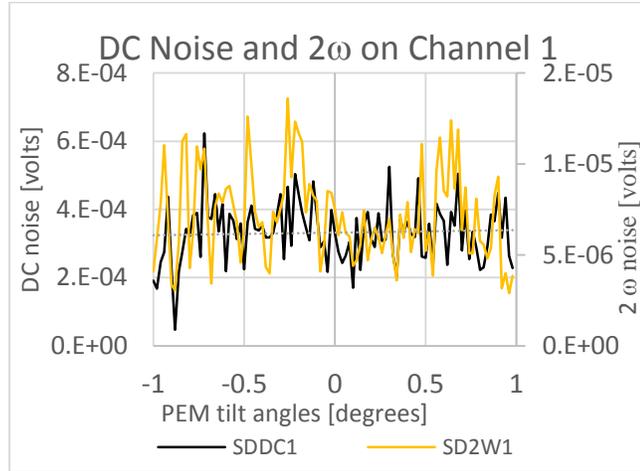


Figure 4.7. DC and 2ω noise correlation of channel 1 as a function of PEM-90 tilt, PDA-55, quarter wavelength retardation, no substrate and field

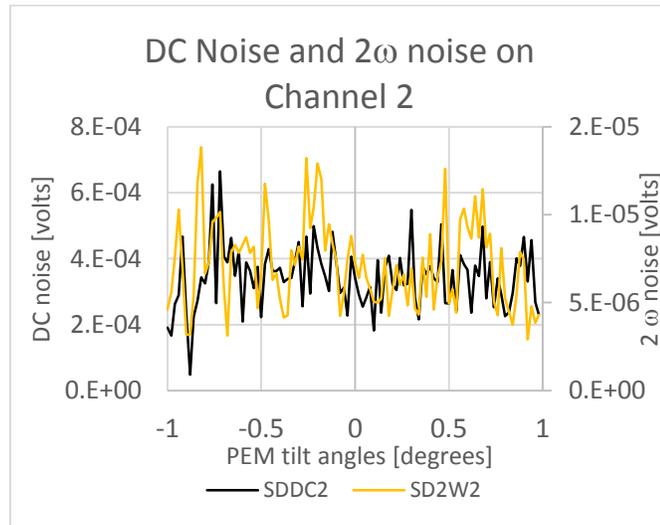


Figure 4.8 DC and 2ω noise correlation of channel 2 as a function of PEM-90 tilt, PDA-55, quarter wave retardation, no substrate and field

The above figures 4.7 and 4.8 summarize the DC and 2ω noise correlation of channel 1 and the DC and 2ω noise correlation of channel 2 as a function of PEM-90 tilt. It is found from the data that the 2ω noises are a factor 10 less than the dc noises. The dc and the 2ω

noises of each individual channel are not so strongly correlated yet they show some correlation. The correlation is quite strong for the smaller range of PEM tilt angle from -0.5 to +0.5 degrees. Note that the effect of pointing direction drifts and the fluctuations of the laser are much less for smaller angles where the derivatives are smaller.

Note that the slope of the noise of the difference signal and the slope of the DC signal are still correlated. It can be concluded from this that as the PEM angle is changed, the beam directions change and less of the beam hits the detector. So, this correlation is not caused by the noise of the laser.

B. Test with PEM-100 and PDA-100-A2 detector:

The experiments were done to analyze the effect of the field using the double axis PEM.

The experiments were carried out in the presence of a sample with field and without field.

The field values from Gaussmeter ranges from + 3400 Oersted to – 3400 Oersted.

Without field:

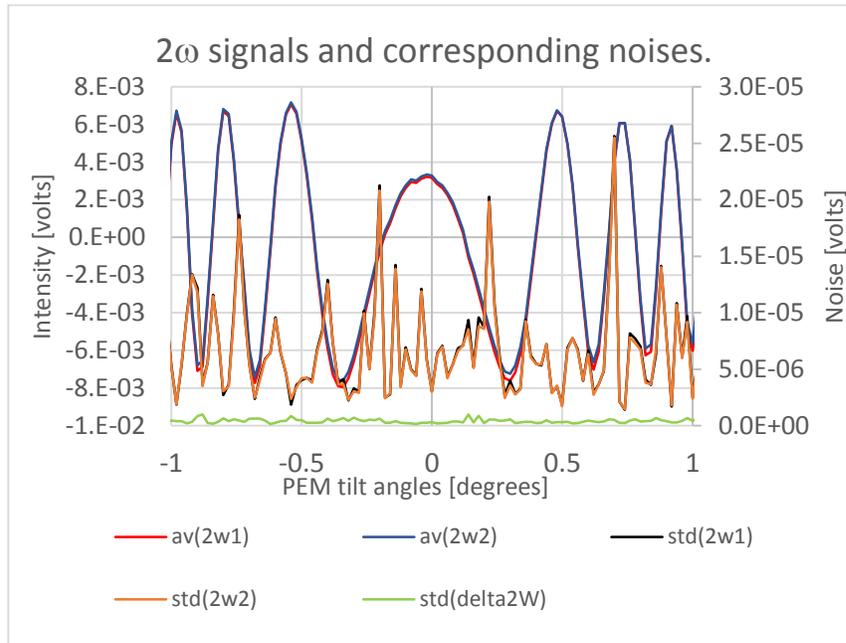


Figure 4.9 The 2ω signals and corresponding noises as a function of PEM-100 tilt angle, NiFeO sample, no field, quarter wave retardation and PDA-100-A2

The above figure 4.9 shows the 2ω signals and corresponding noises as a function of PEM-100 tilt angle. The experiment was performed on a Nickel Iron Oxide sample by keeping the polarizer at 45 degrees, the analyzer at 0 degrees, and the PEM's retardation depth was kept at a quarter wavelength. The NiFeO sample (used in this chapter 4) is RF sputtered sample at 5 sccm of oxygen flow during deposition for 55 minutes. The 2ω intensity for the PEM's tilt angle between -0.2 degrees to +0.12 degrees is a factor 2 less than the other maxima in the graph. This height of this maxima at perpendicular incidence is related to the optical path length of the unstrained crystal. The SNR is 29.6 dB for the individual channel and SNR is 41.5 dB for the difference channel. The single channel SNR is similar to the results obtained with the PEM-90. The difference channel is 4.5 dB higher than the results obtained with the PEM-90. The corresponding dc signals

and dc noises are shown in figure 4.10 below. Note that for the PEM-100 the DC components of both channels are in phase with each other. This is different from the dual beam setup that employs a PEM-90 (compare Fig. 4.10 with Fig. 4.6). It is currently not understood why.

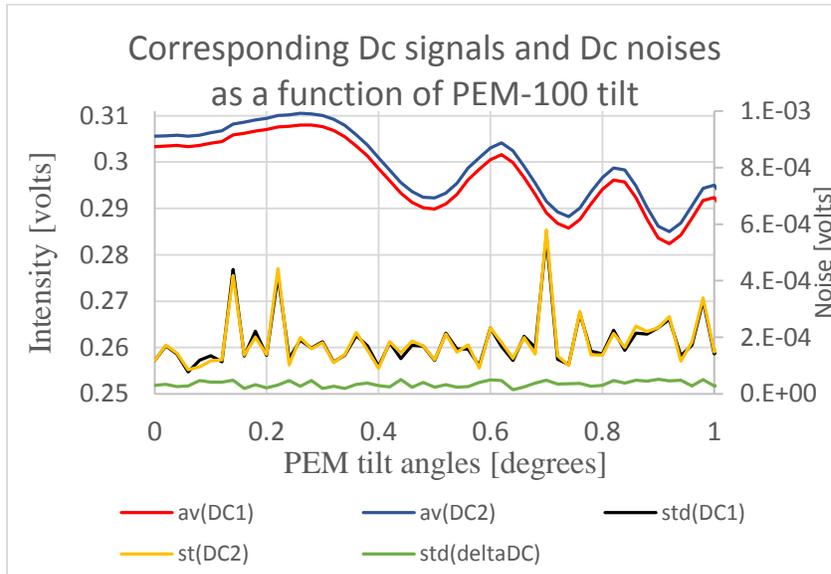


Figure 4.10 2ω signals as a function of PEM-100, PDA-100-A2, NiFeO sample, no field, and a quarter wave retardation

Figure 4.10 above shows the corresponding dc intensity signals and noises in NiFeO sample without field. The dc noises are found to be strongly correlated. From the experiment the S/N ratio of individual channel for the dc signal is found to be 31 dB and the S/N ratio of the difference channel is found to be 38 dB. Both S/N ratio are without equalizing.

With field:

The above figure 4.11 shows the variation of 2ω and corresponding 2ω noises at positive

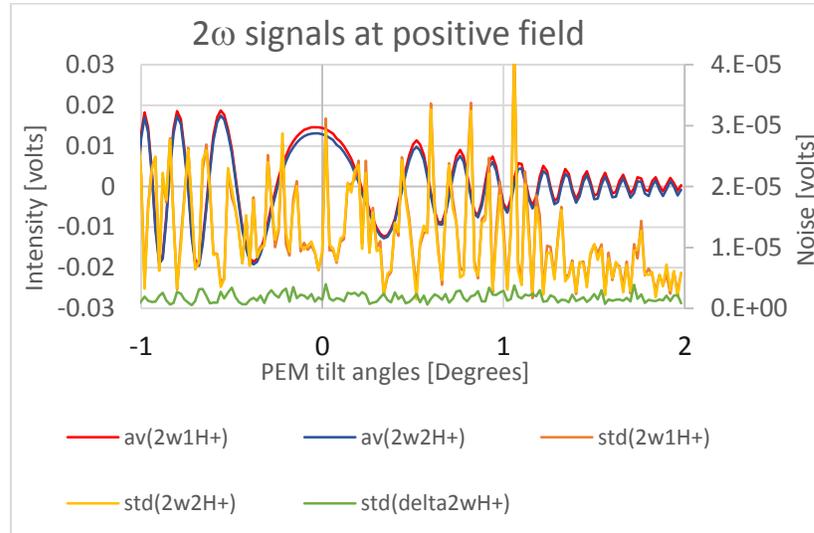


Figure 4.11 Variation of 2ω intensity and corresponding noises as a function PEM tilt, PEM-100, PDA-100-A2, NiFeO sample, and quarter wave retardation

field using the PEM-100 and PDA 100 A2 detectors with an applied field of 3.4KOe. The experiment was carried out for the same Nickel Iron oxide sample as reported on the previous section. So, the same measurement conditions as for the results presented in figure 4.9. The SNR of individual channels is 29.6 dB and that of the difference channel is 39dB. The latter is 3 dB smaller than the SNR measured without applied field. So, the noise level decreases slightly in the presence of a magnetic field. Note that the intensity of this measurement is larger than for the measurement displayed in Fig. 3.9, so the decrease in SNR ratio when applying a magnetic field is actually larger than the here observed 2.5 dB, i.e. $41.5 - 39 + 1.5 = 4$ dB. So, the presence of a sample and magnetic field causes the SNR to go down by a factor of 2. The corresponding dc signals for the same measurement are shown in figure 4.12 below.

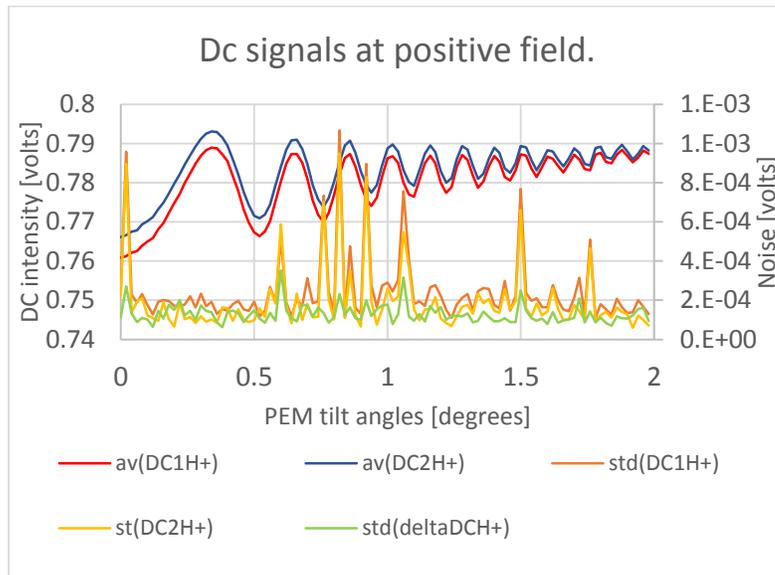


Figure 4.12 Variation of dc intensity and corresponding noises as a function PEM tilt, PEM-100, PDA-100-A2, NiFeO sample, and quarter wave retardation

The SNR of an individual dc channel is 36 dB and that of the difference channel is 39dB without correction. This is a strong improvement in the noise level of dc using the PDA-100-A2 detector in the presence of field and sample with PEM-100. The experiment as a function of PEM tilt angle using PEM-90 and PDA-55 detector for no sample has the same noise level (figure 4.6).

The signal to noise ratio for the different combination is tabulated below:

Table 2 S/N ratio for different combination of PEM and detector with field and sample as a function of PEM tilt angle.

Column1	Average 2w(volts)	Average DC (volts)	S/N DC1	S/N DC2	S/N DC diff	S/N 2ω1	S/N 2ω2	S/N 2ω diff
PEM-90 and PDA-55 Without field and without sample	0.02	0.9	39.8 dB	39.8 dB	36.8 dB	29 dB	29 dB	37 dB
PEM-100 and PDA-100-A2 Without field and with sample	0.004	0.3	31 dB	31 dB	38 dB	29.6 dB	29.6 dB	41.5 dB
PEM-100 and PDA-100-A2 With field and with sample	0.02	0.7	36 dB	36 dB	39 dB	29.6 dB	29.6 dB	39 dB

Interference effects in PEM:

For the suppression of interfered signal, MO signals of both channels i.e. the 2 ω difference intensity of each channel at positive and negative field were calculated. The subtraction of equation 4.1 and equation 4.2, i.e. $MO_{(CH1)} - MO_{(CH2)}$ is the Kerr rotation of the sample along with the interfered signals arising from multiple reflection of the laser in PEM's optic head.

The MO signals for each channel was calculated using the following equations:

$$MO_{CH1} = \frac{(2w1)at H_{positive} - (2w1)at H_{negative}}{2} \quad 4.1$$

$$MO_{CH2} = \frac{(2w2)at H_{Positive} - (2w2)at H_{negative}}{2}$$

4.2

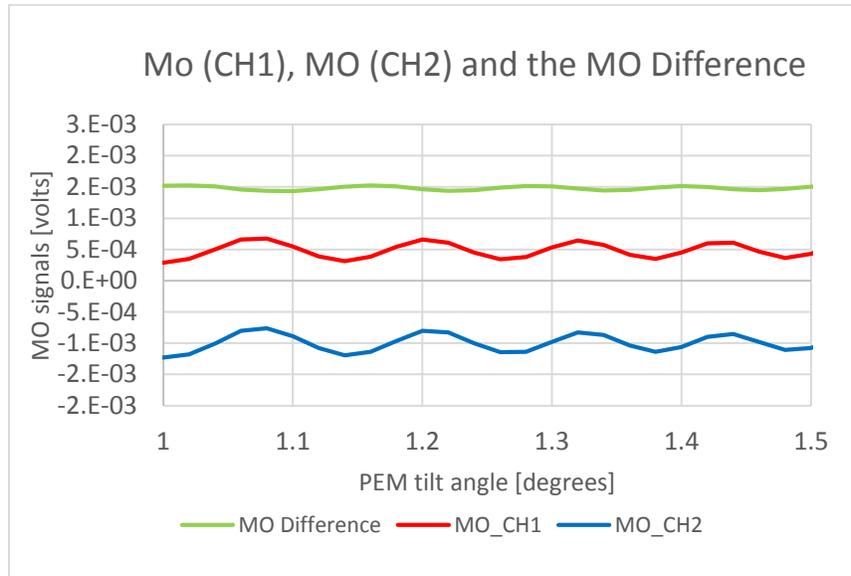


Figure 4.13 The MO signals of NiFeO sample as a function of PEM tilt angle using PEM-100, PDA-100-A2, and at quarter wave retardation

The above figure 4.13 shows the MO signals of channel 1 and 2 and their difference (MO Difference) as a function of PEM-100 tilt angle using PDA-100-A2 detectors. The experiment was performed on a Nickel Iron Oxide sample by keeping the polarizer at 45 degrees, the analyzer at 0 degrees, and the PEM's retardation depth was kept at a quarter wavelength.

The subtraction of MO signals from both channels is almost equal. Even for double axis modulators, where the PEM's optical element stretches and compresses equally in both direction and have the maximum modulation of laser light falling on the detectors,

because of the optical path difference for s and p-polarized light is different there is still a little bit of discrepancy in MO signals. The subtraction of MO signals from both channels cannot be zero as there will be an offset term in the 2ω 's because of the modulation (equation 3.23). Hence there is always a little bit of signal left because of the optical path difference for s and p-polarized light.

4.3 Test as a Function of Retardation

The dual MO setup is also tested by varying retardation depths of the PEM. The results with both PEM-90 and PEM-100 and detectors PDA-55, PDA-100-A2 are presented in this section.

For this experiment a glass substrate and a field of 3.4 KOe was used. The PEM tilt angle kept at normal incidence i.e. at 0 degree. The analyzer angle was kept at 0 degrees. The DC offsets of both channels were subtracted via LabVIEW programming before the start of the measurement.

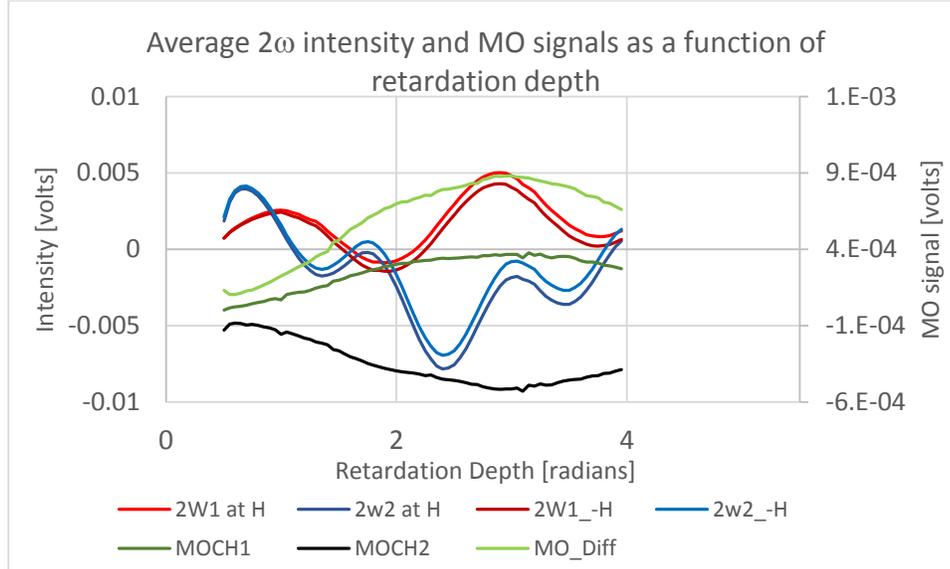


Figure 4.14 Test as a function of retardation on glass slide using PEM-90, PDA-55, and normal incidence of PEM

The above figure 4.14 shows the 2ω intensity of each channels at positive and negative field of 3400 Oersted, and the MO signals of each channel as a function of retardation depth of the PEM. For this experiment the polarizer was kept at 45 degrees and the analyzer was kept at 0 degrees. The PEM was kept at normal incidence i.e. 0 degrees. The MO_{CH1} and MO_{CH2} are calculated using equation 4.1 and 4.2. The MO_{CH1} , MO_{CH2} , and MO difference are all plotted in secondary axis and all other individual 2ω components of individual channels are plotted in primary axis.

The plot of 2ω as a function of retardation depth of the PEM-90 (single axis modulator) have different periods for channel 1 and channel 2 i.e. for P and S component of light. It also seems that those plots are the result of the superposition of two 1st order Bessel functions, both with different argument. For the single axis modulator, the optical path difference for P-component of polarized light (channel 1) and S-component of polarized

light (channel 2) are different which explains for the observed different periods for both channels. The different period for channel 1 and channel 2 can be concluded from the multiple interference effect at PEM's optic head. However, the MO signals of channel 1 and channel 2 both have 1st order Bessel function curves as a function of retardation. The 2ω intensity curve intersects at 1.300, 2.750, and 3.298 retardation depth in radians for both positive and negative field. Note that 1.571 radian is a quarter wave retardation for PEM-90. The noise level of 2ω channels, and difference 2ω channels of the same experiment is shown in figure 4.15.

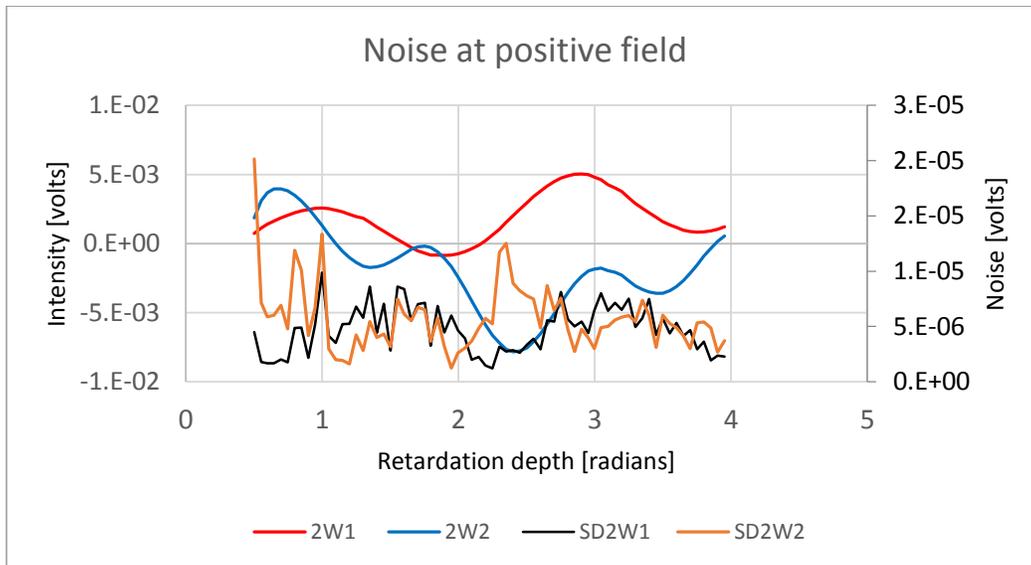


Figure 4.15 Noise of individual channel, difference channel and sum channel at positive field as a function of retardation depth, PEM-90, PDA-55, a glass slide and PEM at normal incidence

The above figure 4.15 shows the corresponding 2ω signals as well as the noise level of individual channels, sum channels and difference channels at positive field as a function of retardation depth of the PEM. The individual noise of both channels are factor 2 noisy

than the difference channel. The difference channel is less noisy when the retardation depth of the PEM is between 1.5 and 1.9 radians or between 2.6 and 2.8 radians. The noises of individual channels have less correlation outside those ranges.

The following experiment is also carried out by keeping the PEM-90 at larger tilt angle of 4.5 degrees. The other measurement parameters were kept constant.

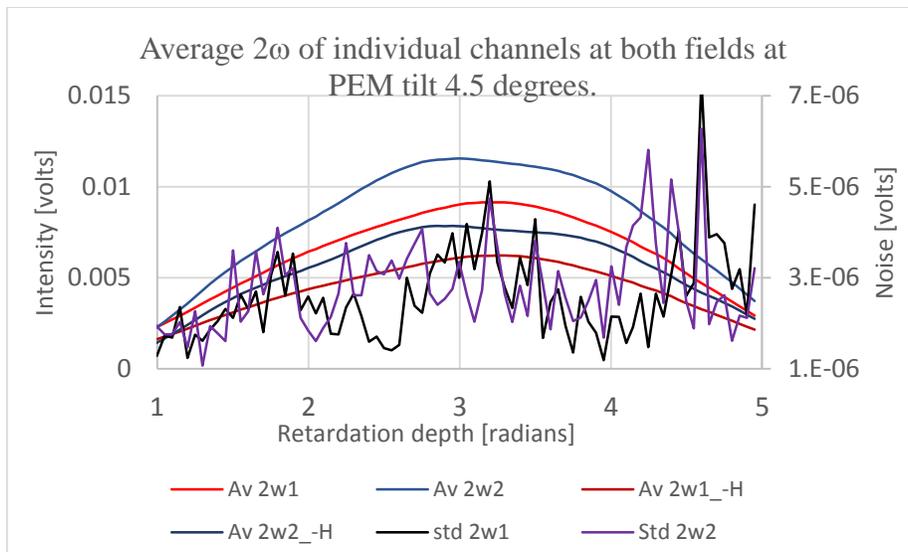


Figure 4.16 2ω intensity of each channels at positive and negative field of 3.4KOe and dc noises at positive field as a function of retardation using PEM-90, PDA-55, a glass slide, and at larger PEM tilt of 4.5 degrees

The above figure 4.16 shows the 2ω intensity of each channels and corresponding noise at positive field. The experiment was carried out at larger PEM tilt angle of 4.5 degrees. The noise of 2ω on individual channels were not strongly correlated for this experiment using PEM-90 and PDA-55 detectors. The MO signal for channel 1 and channel 2 are

shown in figure 4.17. The MO signals of channel 1 and channel 2 is almost equal and the

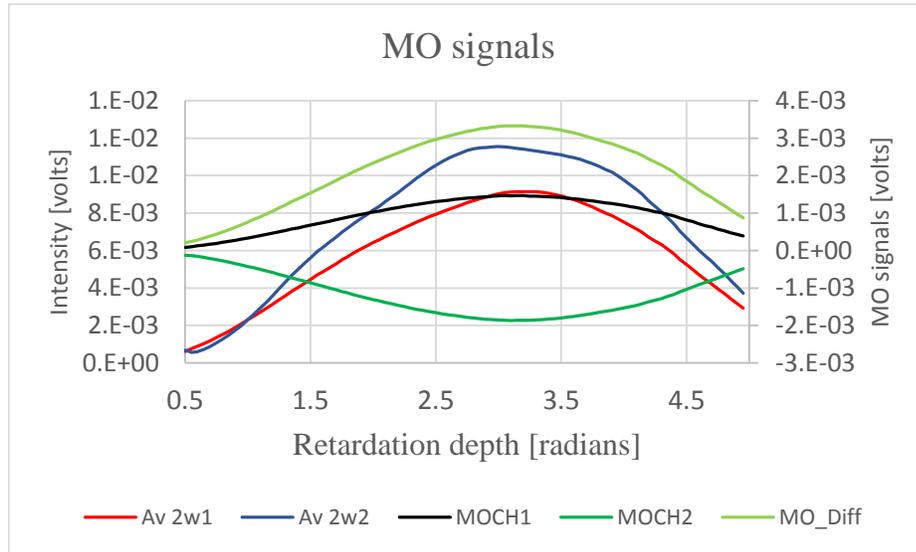


Figure 4.17 The 2ω signals at positive field and the MO signals as a function of the PEM tilt for PEM-90, PDA-55, and at larger PEM tilt of 4.5 degrees

subtraction of MO signal is almost flat at higher PEM tilt angle of 4.5 degrees. The flat MO difference signal is the meaning of suppression of multiple interference effect at higher PEM tilt angle.

The similar experiments were performed with PEM-100 (Double axis modulator), PDA-100-A2 silicon detectors with Nickel Iron Oxide sample and field of $\pm 3.4\text{KOe}$. The PEM tilt angle was kept at normal incidence i.e. at 0 degrees. The analyzer angle was kept at 0 degrees and the polarizer angle was kept at 45 degrees. Figure 4.18 below shows the 2ω intensity of individual channels, corresponding noises of each channels and difference channel at positive field and negative field. The SNR of an individual channel is 33 dB and that of difference channel is 40 dB. Also, the individual 2ω noise of individual channels shows strong correlation at both fields. From the excel calculation the

correlation of the 2ω noise was 0.989155 and that of the dc noise is 0.92054 and is same for both field values.

For the figure 4.18 Bessel function of 1st order was observed with dual axis modulator.

The δ_{p0} and δ_{s0} phase terms in the modulator Jones matrix for double axis modulator are same. The observed same periodicity can be concluded from same δ_{p0} and δ_{s0} phase terms for double axis modulator.

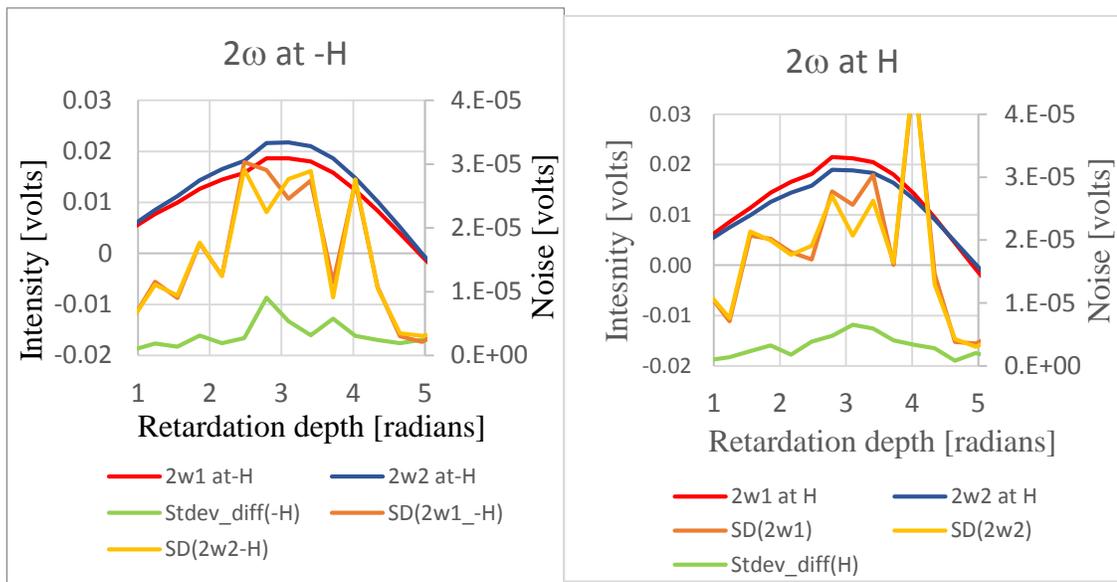


Figure 4.18 2ω intensity and corresponding noises as a function of retardation depth at positive field, PEM-100, PDA-100-A2, NiFeO sample

5. TEST OF DBM SETUP WITH NICKEL OXIDE AND NICKEL IRON OXIDE SERIES

The dual detector MOKE set-up was tested by measuring the MO properties of a series of NiO samples sputtered on 3" quartz wafers. The samples were co-sputtered using two RF guns at 200 Watt each for 20 minutes. The sputter gas flow during deposition in the chamber was 50 sccm and consisted of a mixture of argon gas and oxygen gas. The samples were sputtered by Anival Ayala and Brian Collier. Samples using sputter gas with different oxygen concentration.

Measurement condition: A LabVIEW program was developed for the measurement of the 2ω intensity as a function of the applied field. No effort was made to adjust for the remanence of the pole pieces of the electromagnet. The field as estimated from the sourced current through the Kepco power supply. The polarizer was kept at 46.18 degrees and the analyzer was kept at -0.923 degrees during the measurements. For these angles the $I_{2\omega}$ signals of both channels were minimal. The measurements were done with the PEM-100 (double axis modulator) with the retardation depth kept at a quarter wavelength and the photo-detectors used were PDA-100-A2, silicon switchable gain detectors. The PEM tilt was kept at 0 degrees for the measurement of the samples. The phase difference of both lock in with respect to the 1 omega reference signal of the PEM's electronic head were made sure to have equal magnitude before the run for each sample. Two measurements were done for each sample. The first measurement was done by letting the laser goes through an area of the quartz wafer that was covered with the NiO thin film. Then a second measurement was done with the laser beam through just the substrate

region of the wafer (measured in the deposition shade of a substrate clip).

Each measurement started with a calibration procedure where the signals of both channels were measured for two analyzer-detector unit angles, i.e. -1.4230 and -0.4230 degrees in zero field. The measured signals were converted in sensitivities using the following expressions:

$$Sens_1 = I_{2\omega 1}(-0.4230) - I_{2\omega 1}(-1.4230)$$

$$Sens_2 = I_{2\omega 2}(-0.4230) - I_{2\omega 2}(-1.4230)$$

$$Sens_{\Delta} = Sens_1 - Sens_2$$

After the calibration the $I_{2\omega}$ of both channels and the difference channel were measured as a function of the field. A linear regression was done in LabVIEW to determine the slope of the H versus $I_{2\omega}$ graphs. The calculated slopes in volt/Oe of both channels and of the difference channel were converted to degr/Oe. After this the calculated slopes for the measurements done on the substrate+film were subtracted from the calculated slopes for the measurements done on the substrate to determine the Faraday rotation of just the thin film.

The measured $I_{2\omega}$ signals for two samples (film + substrate measurement) are shown in the figure 5.1 below. At zero field the $I_{2\omega}$ has the same sign on both channels and is originating from the multiple interference effect. Then when the field is increased the $I_{2\omega}$ signal increase for channel 2 and decreases for channel 1. These changes are of MO origin. Subtracting the $I_{2\omega}$ signal in both channels shows a curve symmetric around zero.

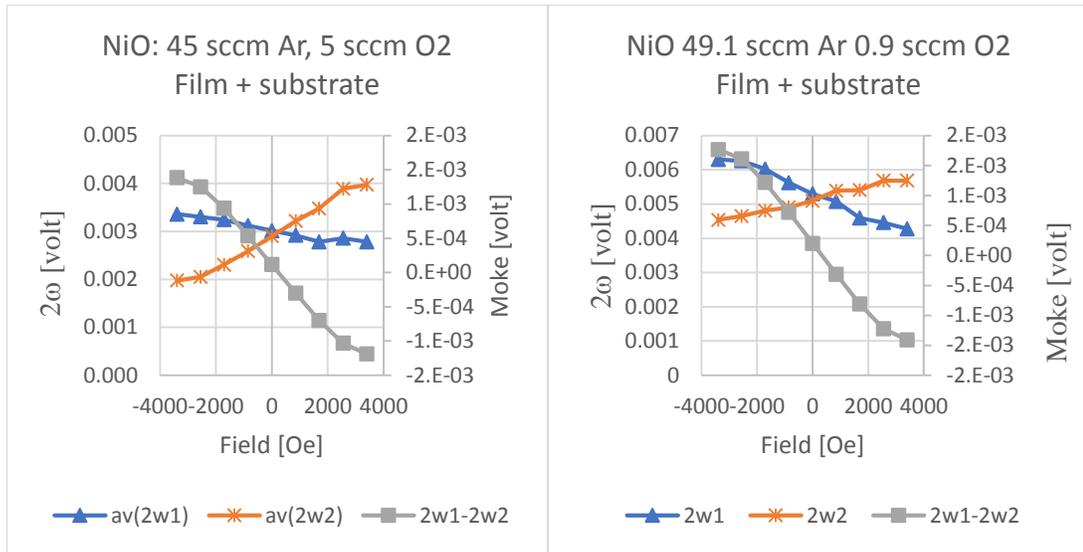


Figure 5.1 Measured 2ω intensity signals for NiO samples for different oxygen flow

These results show that indeed the multiple interference effects cancels out in dual MOKE measurement.

The figure 5.1 shows the measured 2ω intensity signals for NiO samples for 5 sccm and 0.9 sccm oxygen flow during sputtering. There is no doubt that the noise originating from the multiple interference effects in the single channel is strongly suppressed in the difference 2ω channel. Note that these measurements are taken at 1.571 radians and one can do significantly better if one measures at 2.4 radians where the sensitivity for the Kerr signal is approximately a factor 2 larger.

Note that we were not able to measure this with the single axis modulator, i.e. the PEM-90 as the multiple interference effect has opposite sign in both channels at 1.571 radians. The figure 5.2 below shows the MOKE signals in volts measured for the difference channel. The substrate has a larger slope than the sample, which implies that the Faraday rotation of thin film and substrate are opposite to each other. Note that the signal measured on all

samples is not the same which suggests that the Faraday rotation varies with the oxygen flow during deposition. The measured sensitivity for the difference channel was used to convert the graphs from Fig. 5.2 into rotation values. The results are summarized in Fig.

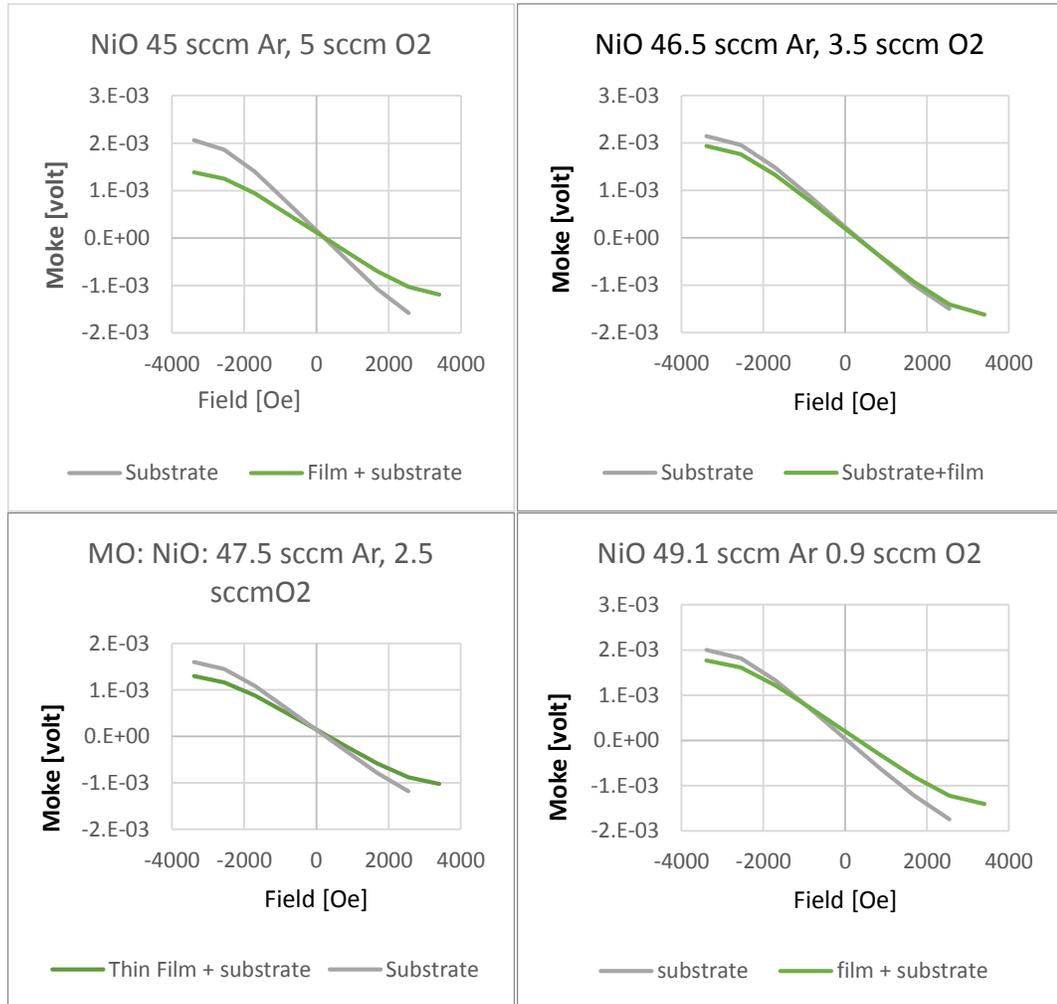


Figure 5.2 MOKE in volts for difference channel for different samples of NiO at different oxygen flow during deposition

5.3 below. Note that the effect of oxygen flow on the Faraday rotation is much smaller than on the raw $I_{2\omega}$ signals. For one of the samples the sign of the Faraday effect flips.

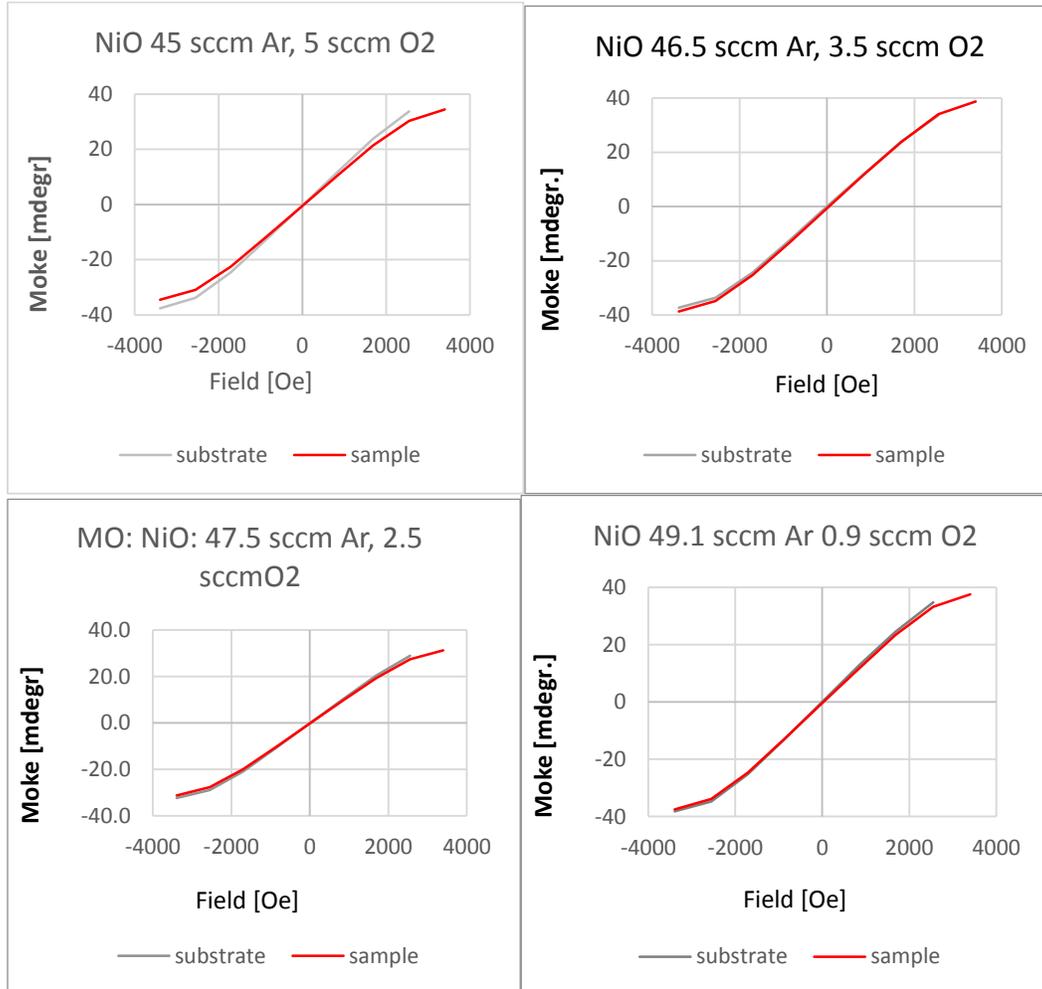


Figure 5.3 MOKE in volts for difference channel for different samples of NiO at different oxygen flow during deposition

Fig. 5.4 below shows the measured rotation per Oe as a function of the oxygen concentration in the sputter gas. The measurement bars along the y-axis are estimated from 31 consecutive measurements separated by 2 time constants (300 msec). The

uncertainty is 14 times smaller for the dual beam setup than for the single beam setup. The graph shows the measured data on four different wafers with the single beam and dual beam setup. Although the measurements were done at exactly the same locations and at exactly the same time, the data does not overlap. This suggests that except for the measurement error of the setup another error is included in the graph.

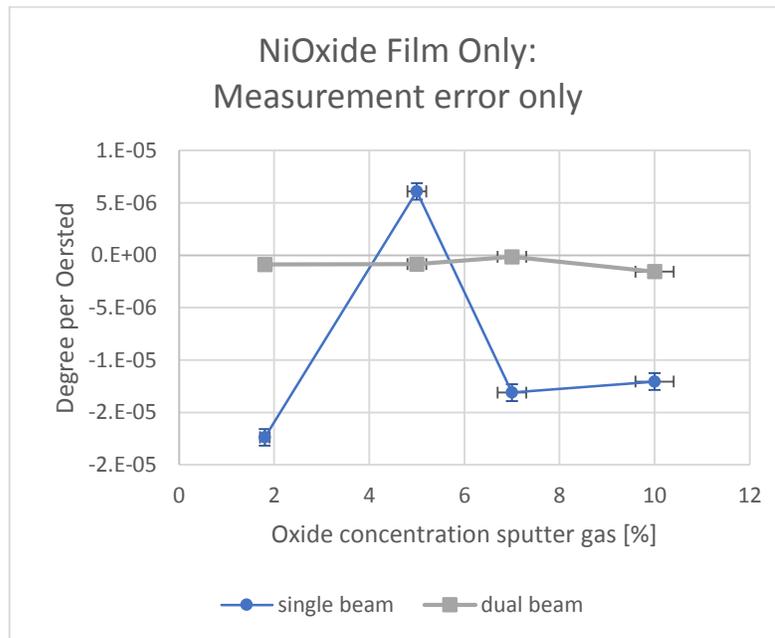


Figure 5.4 MO data of RF co-sputtered NiO thin films as a function of the oxygen concentration in the sputter gas in percentage measured using the dual beam and single beam methods. Included error bars indicate spread of the measurement results

An uncertainty not taken into account for the errors bars in the figure above is that originating from the substrate subtraction. To estimate this error the spread of the measurement results on 4 different wafers was used. The uncertainty for the dual beam setup is two times smaller than the uncertainty for the single beam setup. The new error bars are included in the graph below. Note that now the curves overlap. In order to make

meaningful conclusions on how the MO properties of NiO thin films vary with oxygen flow, one need to study thicker films and use a substrate with a smaller more consistent Faraday rotation.

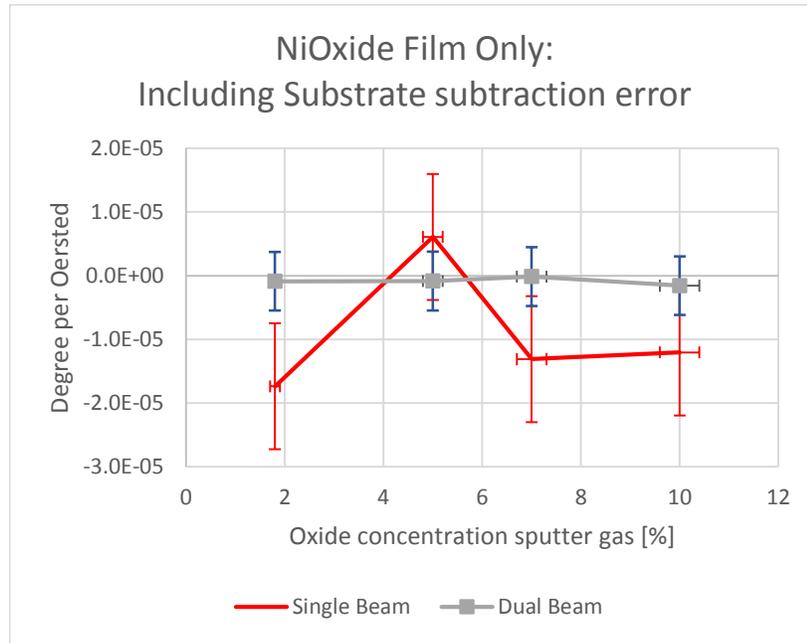


Figure 5.5 MO data for RF-sputtered NiO as a function of the oxygen flow measured by dual beam method (grey) and measured by single beam method (red) including measurement errors caused by substrate subtraction

The tabulation of measured sensitivities in degrees per oersted is reported on in an appendix D as a technical report for Nickel Oxide and Nickel Iron Oxide.

6. DISCUSSION OF RESULTS AND FURTHER RESEARCH

A dual beam MOKE setup employing a PEM was designed and constructed by replacing the analyzer of a single beam MOKE setup by a Wollaston prism and adding a second detector. The optics alignment as well as the choice of detector and the PEM are crucial for the duo detector MOKE setup.

The beam transmitted or reflected of the sample is split into two orthogonal high quality linearly polarized beams by the use of a Wollaston prism. A standard LabVIEW program was written to control the stepmotor that tilts the PEM. Existing LabVIEW drivers that control the analyzer and polarizer prisms angles were adapted to include a handshake method to increase their reliability. Modifications were made to the hardware and software for simultaneous data acquisition of both channels using external triggering through the TTL output of an HP IO switching unit. The Jones Matrix approach was used to derive the underlying physics for a single beam DC MOKE setup, a dual DC MOKE setup, a single beam modulated MOKE setup, and a dual beam modulated MOKE setup. The effect of the PEM multiple interference effect was included in the model for the modulated MOKE setups.

The MOKE signals of a glass slide were measured as a function of PEM tilt, analyzer angle and PEM retardation depth. The 2ω signals and the dc signals of both channels were measured with SR830 Lock-in amplifiers and HP 3457A multimeters.

The DC as well as 2ω noise correlation of individual channels was larger for the PEM-100 than for the PEM-90 (single axis modulator).

The MOKE signals i.e. the difference of the 2ω signals taken at positive and negative field were strongly correlated for both channels. The experimental results showed the effective suppression of the multiple interference effects using a double axis modulator. Also, an increase of the S/N ratio with a factor 6 was observed for such setup compared to a setup that uses a single axis modulator. As the PEM's optical element for double axis modulators, stretches or compresses in both directions the multiple interference contributions to both channels is the same and subtraction of the signal of both channels results in canceling out the offset term of the multiple interference effect completely at perpendicular incidence.

From observations the dual beam setup is also less sensitive for sample movements and shows promise to be used with a materials tester for monitoring of the magnetic properties while stretching the material.

The dual beam modulated MO setup was tested with a series of Nickel oxides and Nickel iron oxide RF sputtered thin films. The measurement results show that the S/N ratio of the dual beam technique is a factor 14 larger than the single beam technique for these type of materials.

APPENDIX SECTION

A. External Triggering command for LabVIEW

The following commands were adopted for the implementations of external triggering:

1. TRIG HOLD: This command blocks the triggering mechanism to temporarily prevent measurements from being taken and stored.
2. TARM AUTO: This command instructs the HP 3457A multimeter to automatically satisfy the trigger arm event whenever required.
3. MFORMAT SREAL: This command specifies that the readings are to be stored in the single real format (4 bytes per reading).
4. MSIZE XXX: This command allocates XXX bytes of memory to reading storage. This is calculated by number of readings times 4 bytes per reading.
5. MEM FIFO: This command clears any previous readings from the memory and then configures storage for first-in-first-out access.
6. NRDGS, XXX, EXT: This command makes sure that one reading will be taken per pulse present at the EXT trigger arm even until XXX readings have taken.
7. TRIG SGL: This command triggers the HP 3457A for one measurement cycle. It also makes sure, each of those pulses received at the EXT terminal initiates a measurement.

B. Comparison with the analysis of Gemeiner [44] et al

In this section the analysis presented above is compared with the analysis of Gemeiner et al for the circular birefringence case.

To describe the circular birefringence effect (Faraday rotation) Gemeiner et al. used the rotation matrix:

$$\begin{pmatrix} \cos\theta_k & -\sin\theta_k \\ \sin\theta_k & \cos\theta_k \end{pmatrix} \quad \text{B.1}$$

This Jones matrix describes a rotation of the plane of polarization over θ_k degrees. So, it is assumed by Gemeiner et al that the ellipticity of the beam is not affected. Note that for magnetic thin films both effects are expected to occur. So, the Fresnel matrix used in section 3.2 above is complex while the Jones matrix of the sample used by the Gemeiner only has real components. It can be shown that the approach of this thesis leads to a similar result if one only assumes that the sample has a Kerr rotation and its Kerr ellipticity is zero. The most general Fresnel reflection matrix for the polar Kerr effect is given by:

$$\begin{bmatrix} r_{pp} & r_{ps} \\ -r_{ps} & r_{ss} \end{bmatrix} \quad \text{B.2}$$

Dividing the above matrix by r_{pp} gives

$$\frac{1}{r_{pp}} \begin{bmatrix} 1 & \frac{r_{ps}}{r_{pp}} \\ -\frac{r_{ps}}{r_{pp}} & 1 \end{bmatrix} \quad \text{B.3}$$

Now, if there is only Kerr rotation $\frac{r_{ps}}{r_{pp}} = \theta_k + i\eta_k = \theta_k$

So the matrix changes to

$$\frac{1}{r_{pp}} \begin{bmatrix} 1 & \theta_k \\ -\theta_k & 1 \end{bmatrix} \quad \text{B.4}$$

Which is similar to the rotator matrix used by Gemeiner.

So the calculation presented in this thesis is also valid for absorbing media and can be considered an extension to the calculation done by Gemeiner et al.

Note that the calculation approach followed by Gemeiner et al. leads to a significant reduction of the calculation complexity:

$$\begin{pmatrix} E_x \\ E_y \end{pmatrix} = \begin{pmatrix} \frac{e^{i\delta_p}}{1 - r^2 e^{2i\delta_p}} \\ \frac{e^{i\delta_s}}{1 - r^2 e^{2i\delta_s}} \end{pmatrix} \quad \text{B.5}$$

The polarizer at β is the same as rotating the Jones vector over $-\beta$ degrees and then using a polarizer at 0 degrees, so

$$\begin{pmatrix} 1 & 0 \\ 0 & 0 \end{pmatrix} \begin{pmatrix} \cos\beta & \sin\beta \\ -\sin\beta & \cos\beta \end{pmatrix} \begin{pmatrix} E_x \\ E_y \end{pmatrix} = \cos\beta \cdot E_x + \sin\beta \cdot E_y \quad \text{B.6}$$

Now with faraday rotation gives:

$$\begin{pmatrix} 1 & 0 \\ 0 & 0 \end{pmatrix} \begin{pmatrix} \cos\beta & \sin\beta \\ -\sin\beta & \cos\beta \end{pmatrix} \begin{pmatrix} \cos\beta & -\sin\beta \\ \sin\beta & \cos\beta \end{pmatrix} \begin{pmatrix} E_x \\ E_y \end{pmatrix} \quad \text{B.7}$$

$$= \cos(\beta - \theta) \cdot E_x + \sin(\beta - \theta) \cdot E_y$$

C. Mathcad Simulation:

$$\omega = 2. \pi. 50000$$

$$b = \frac{\pi}{4}$$

$$A(b) = \begin{bmatrix} \cos^2 b & \cos b \sin b \\ \cos b \sin b & \sin^2 b \end{bmatrix} \text{ and } P(\text{pol}) = A(\text{pol})$$

$$r_{pp}(n, \Psi) = \frac{\cos(\Psi) - \sqrt{n^2 - (\sin(\Psi))^2}}{\cos(\Psi) + \sqrt{n^2 - (\sin(\Psi))^2}}$$

$$\text{Let, } X = (1 + r_{pp}(1.5, 0))^2 \cdot e^{1i \cdot \delta_0 \cdot \sin(\omega \cdot t)} \text{ and } Y = (1 + r_{pp}(1.5, 0))^2 \cdot e^{-1i \cdot \delta_0 \cdot \sin(\omega \cdot t)}$$

Then,

$$PEM(\delta_0, t) =$$

$$\begin{pmatrix} e^{1i \cdot \delta_0 \cdot \frac{\sin(\omega \cdot t)}{2}} \cdot X & 0 \\ 0 & e^{-1i \cdot \delta_0 \cdot \frac{\sin(\omega \cdot t)}{2}} \cdot Y \end{pmatrix}$$

$$r_{ss}(n, \Psi) = \frac{-n^2 \cdot \cos(\Psi) + \sqrt{n^2 - (\sin(\Psi))^2}}{n^2 \cdot \cos(\Psi) + \sqrt{n^2 - (\sin(\Psi))^2}}, E_i = \begin{pmatrix} 1 \\ -1i \end{pmatrix}$$

$$r_{ps}(n, \Psi) = (0.091 + 0.000 * 1i) \cdot \frac{\pi}{180} \cdot r_{ss}(n, \Psi)$$

$$R(n, \Psi) = \begin{bmatrix} r_{pp}(n, \Psi) & r_{ps}(n, \Psi) \\ -r_{ps}(n, \Psi) & r_{ss}(n, \Psi) \end{bmatrix} \text{ such that } R(1.5, 0) \\ = \begin{bmatrix} -0.2 & -3.176 \cdot 10^{-4} \\ 3.176 \cdot 10^{-4} & -0.2 \end{bmatrix}$$

$$r_{pp}(2.16 - 4.1 * 1i, 0) = -0.764 + 0.306i$$

$$R(2.16 - 4.1 * 1i, 0) = \begin{bmatrix} -0.764 + 0.306i & -0.001 + 4.86i * 10^{-4} \\ 0.001 - 4.86i * 10^{-4} & -0.764 + 0.306i \end{bmatrix}$$

$$E_o(t) = A\left(\frac{1.2}{180} \cdot \pi\right) \cdot R(2.16 - 4.1 * 1i, 0) \cdot PEM(\pi, t) \cdot P\left(\frac{\pi}{4}\right) \cdot E_i$$

$$t := 0, 0.0000001 \dots 0.00004$$

$$I(t) := \|E_o(t)_1\|^2 + \|E_o(t)_0\|^2$$

Gemeiner Approach:

$$R_{ot}(q) = \begin{bmatrix} \cos(q) & -\sin(q) \\ \sin(q) & \cos(q) \end{bmatrix}; q(n, \psi) := \frac{r_{ps}(n, \psi)}{r_{ss}(n, \psi)}, q(2.16 - 4.1 * 1i, 0) \\ = 0.002 - 9.794i * 10^{-20}$$

$$P_o := \begin{bmatrix} 1 & 0 \\ 0 & 0 \end{bmatrix}, -Re\left(\frac{r_{ps}(1.5,0)}{r_{ss}(1.5,0)}\right) R(2.16 - 4.1 * 1i, 0) = \\ \begin{bmatrix} -0.764 + 0.306i & -0.001 + 4.86i * 10^{-4} \\ 0.001 - 4.86i * 10^{-4} & -0.764 + 0.306i \end{bmatrix}$$

$$R_{ot}\left(Re\left(\frac{r_{ps}(1.5,0)}{r_{ss}(1.5,0)}\right)\right) = \begin{bmatrix} -0.764 + 0.306i & -0.001 + 4.86i * 10^{-4} \\ 0.001 - 4.86i * 10^{-4} & -0.764 + 0.306i \end{bmatrix}$$

$$E_{go}(t) = r_{pp}(2.16 - 4.1 * 1i, 0) \cdot R_{ot}\left(\frac{1.2}{180} * \pi\right) \cdot P_o \cdot R_{ot}\left(\frac{-1.2}{180} * \pi\right) \cdot R_{ot}\left(-Re\left(\frac{r_{ps}(1.5,0)}{r_{ss}(1.5,0)}\right)\right) \cdot PEM(\pi, t) \cdot P\left(\frac{\pi}{4}\right) \cdot E_i$$

$$I_g(t) = \|E_{go}(t)_1\|^2 + \|E_{go}(t)_0\|^2$$

D. Tabulation of measurement of degrees per oersted (Oe) of samples (Technical report).

Tabulation of sensitivity of channels as well as the measured degrees per oersted for samples are tabulated below.

Table 3 Corresponding θ_k in degrees per Oe. for NiO (film and substrate).

O2 concentration	$2\omega_1$ Deg/Oe	$2\omega_2$ Deg/Oe	$2\omega_1-2\omega_2$ Deg/Oe	Dc1 sensitivity (Volts)	Dc2 sensitivity (Volts)	$2\omega_1$ sensitivity (Volts)	$2\omega_2$ sensitivity (Volts)
5	5.07E-06	1.71E-05	1.11E-05	0.017917	0.016283	-0.01843	0.018878
3.5	3.47E-06	2.11E-05	1.25E-05	0.027201	0.023798	-0.022346	0.023641
2.5	0.82E-05	1.18E-05	1.00E-05	0.018806	0.015883	-0.01819	0.018974
0.9	1.57E-05	0.86E-05	1.21E-05	0.019648	0.020162	-0.021035	0.021243

Table 4 Corresponding θ_k in degrees per Oe. for NiO (substrate).

O2 concentration	$2\omega_1$ Deg/Oe	$2\omega_2$ Deg/Oe	$2\omega_1-2\omega_2$ Deg/Oe	Dc1 sensitivity (Volts)	Dc2 sensitivity (Volts)	$2\omega_1$ sensitivity (Volts)	$2\omega_2$ sensitivity (Volts)
5	1.21E-05	1.32E-05	1.27E-05	0.027868	0.021684	-0.024918	0.026141
3.5	1.11E-05	1.41E-05	1.27E-05	0.027518	0.022797	-0.025209	0.026214
2.5	4.72E-06	1.67E-05	1.09E-05	0.024899	0.020278	-0.02205	0.023367
0.9	2.60E-05	0.90E-06	1.31E-05	0.026427	0.023637	-0.024904	0.026367

Table 5 Corresponding θ_k in degrees per Oe. for NiFeO (film and substrate).

O2 concentration	$2\omega_1$ Deg/Oe	$2\omega_2$ Deg/Oe	$2\omega_1-2\omega_2$ Deg/Oe	Dc1 sensitivity (Volts)	Dc2 sensitivity (Volts)	$2\omega_1$ sensitivity (Volts)	$2\omega_2$ sensitivity (Volts)
14	2.02E-05	2.71E-06	1.14E-05	0.016054	0.015848	-0.021572	0.022142
10	0.77E-05	1.38E-05	1.08E-05	0.013281	0.018823	-0.022159	0.022898
7	4.92E-06	1.47E-05	0.98E-05	0.023104	0.019973	-0.024291	0.024772
3.5	1.73E-05	5.15E-06	1.11E-05	0.018531	0.016547	-0.018353	0.01945
1.3	0.62E-05	1.63E-05	1.14E-05	0.017599	0.017864	-0.01987	0.020656

Table 6 Corresponding θ_k in degrees per Oe. for NiFeO (substrate).

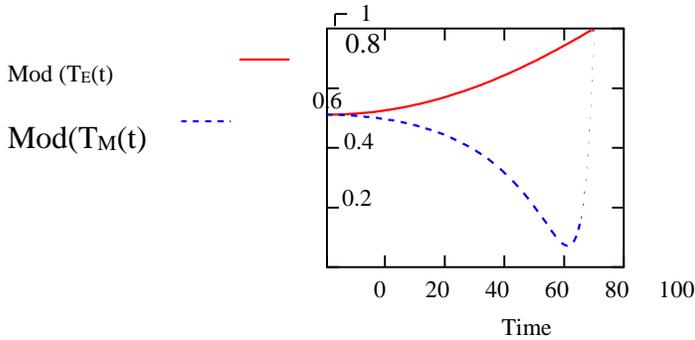
O2 concentration	$2\omega_1$ Deg/Oe	$2\omega_2$ Deg/Oe	$2\omega_1-2\omega_2$ Deg/Oe	Dc1 sensitivity (Volts)	Dc2 sensitivity (Volts)	$2\omega_1$ sensitivity (Volts)	$2\omega_2$ sensitivity (Volts)
14	1.14E-05	1.04E-05	1.08E-05	0.024779	0.020612	-0.024646	0.025502
10	0.97E-05	1.5E-05	1.24E-05	0.023442	0.023015	-0.026752	0.027407
7	0.92E-05	1.30E-05	1.11E-05	0.024443	0.021342	-0.025985	0.026596
3.5	1.55E-05	0.77E-05	1.15E-05	0.022434	0.020843	-0.022124	0.023111
1.3	0.63E-05	1.47E-05	1.06E-05	0.022631	0.020053	-0.024015	0.025285

E. Change of angle of incidence on Fresnel reflection coefficients:

N (refractive index):= 3.7 + 5.4·I (For Gallium) t := 0, 1 .. 90

Fresnel Reflection Coefficients for p and s component of light:

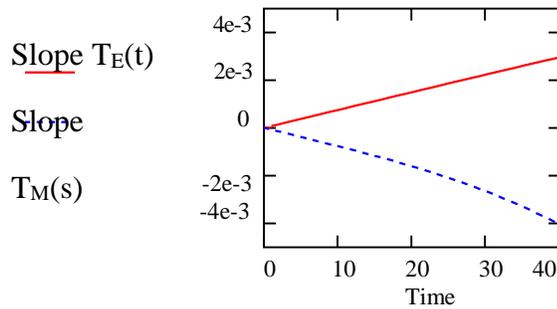
Where $T_E(t)$ and $T_M(t)$ are the Fresnel reflection coefficients for P and S components of light.



Change of reflection coefficient with angle of incidence

$$\text{Slope } T_E(t) = \frac{d}{dt} T_E(t) \quad \text{Slope } T_M(t) = \frac{d}{dt} T_M(t)$$

s:= 0, 1.. 80



It should be noted that this simulation is incomplete as only the reflection coefficients are considered as a function of change in angle of incidence of the laser. Kerr rotation are small signals in the order of few milli volts. So the sample movements are sensitive for the Kerr signals measurement.

REFERENCES

- [1] Kerr, J.J.T.L., Edinburgh,, D.P. Magazine, and J.o. Science, XLIII. On rotation of the plane of polarization by reflection from the pole of a magnet. 1877. 3(19): p. 321-343.
- [2] Brauer, B., et al., Magneto-optical Kerr effect spectroscopy--a sensitive tool for investigating the molecular orientation in organic semiconductor films. J Phys Chem B, 2009. 113(45): p. 14957-61.
- [3] Pedrotti, F.L., L.M. Pedrotti, and L.S. Pedrotti, Introduction to optics. 2017: Cambridge University Press.
- [4] Chang, J.T., J.J.F. Dillon, and U.F. Gianola, Magnetic-optical information storage unit and apparatus. 1965, Google Patents.
- [5] Sato, K.J.J.J.o.A.P., Measurement of magneto-optical Kerr effect using piezo-birefringent modulator. 1981. 20(12): p. 2403.
- [6] Frank, L., et al., Introduction to optics. 1993, Prentice-Hall International Inc., New York.
- [7] Badoz, J., et al., Sensitive Devices to Determine State and Degree of Polarization of a Light-Beam Using a Birefringence Modulator. Journal of Optics-Nouvelle Revue D Optique, 1977. 8(6): p. 373-384.
- [8] Geerts, W., et al., Biaxial Kerr magnetometry in oblique field for the study of thin films with a perpendicular anisotropy. 1994. 137(1-2): p. 224-232.

- [9] Faraday, M. and C.F. Schönbein, *The Letters of Faraday and Schoenbein, 1836-1862: With Notes, Comments and References to Contemporary Letters.* 1899: Benno Schwabe.
- [10] Parkin, S.S., N. More, and K.P. Roche, Oscillations in exchange coupling and magnetoresistance in metallic superlattice structures: Co/Ru, Co/Cr, and Fe/Cr. *Phys Rev Lett*, 1990. 64(19): p. 2304-2307.
- [11] Feil, H., *Magneto-optical Kerr Effect: The Relation Between Optical, Transport and Electronic Properties in Magnetic Compounds.* 1987, Rijksuniversiteit Groningen.
- [12] Chen, X., et al., Dual-polarity plasmonic metalens for visible light. *Nature communications*, 2012. 3: p. 1198.
- [13] Kliger, D.S. and J.W. Lewis, *Polarized light in optics and spectroscopy.* 2012: Elsevier.
- [14] Allwood, D., et al., Magneto-optical Kerr effect analysis of magnetic nanostructures. *Journal of Physics D: Applied Physics*, 2003. 36(18): p. 2175.
- [15] Oliva, E., Wedged double Wollaston, a device for single shot polarimetric measurements. *Astronomy and Astrophysics Supplement Series*, 1997. 123(3): p. 589-592.
- [16] Fan, J.-Y., H.-X. Li, and F.-Q. Wu, A study on transmitted intensity of disturbance for air-spaced Glan-type polarizing prisms. *Optics communications*, 2003. 223(1-3): p. 11-16.
- [17] Chen, X., et al., The measurement of magneto-optical Kerr effect of ultrathin films in a pulsed magnetic field. *Measurement*, 2013. 46(1): p. 52-56.

- [18] The Electric, Magnetic and Optical Characterization of Permalloy Oxide Grown by Dual Ion Beam Sputtering, Maclyn Stuart. Accessed Apr. 15, 2019. Available: <https://digital.library.txstate.edu/handle/10877/5287>
- [19] Electrical and Optical Properties of RRAM, Cui Yubo. Accessed Apr. 15, 2019. Available: <https://digital.library.txstate.edu/handle/10877/6342>
- [20] Magnetic Properties of Reactive Co-Sputtered NiFe-Oxide Samples DC Binod, AA Oliva, A Ayala, S Acharya, F Twagirayezu, JN Talbert, ...IEEE Transactions on Magnetism 55 (2), 1-5
- [21] Theoretical and Experimental Determination of Properties of NiO and Fe-doped NiO, Twagirayezu, Fidele J Accessed Apr. 15, 2019. Available: <https://digital.library.txstate.edu/handle/10877/6815>
- [22] Bohren, C.F. and D.R. Huffman, Absorption and scattering of light by small particles. 2008: John Wiley & Sons.
- [23] Huard, S., Polarization of light. Polarization of Light, by Serge Huard, pp. 348. ISBN 0-471-96536-7. Wiley-VCH, January 1997., 1997: p. 348.
- [24] Penninckx, D. and V. Morénas, Jones matrix of polarization mode dispersion. Optics Letters, 1999. 24(13): p. 875-877.
- [25] Heffner, B.L., Automated measurement of polarization mode dispersion using Jones matrix eigenanalysis. IEEE photonics technology letters, 1992. 4(9): p. 1066-1069.
- [26] Yeh, P., Extended Jones matrix method. JOSA, 1982. 72(4): p. 507-513.
- [27] Hale, P.D. and G.W. Day, Stability of birefringent linear retarders (waveplates). Applied optics, 1988. 27(24): p. 5146-5153.

- [28] Ignatov, L.Y., Y.A. Bobrov, and P.I. Lazarev, Dichroic polarizer and method for making the same. 2003, Google Patents.
- [29] Takano, K., M. Saito, and M. Miyagi, Cube polarizers by the use of metal particles in anodic alumina films. *Applied optics*, 1994. 33(16): p. 3507-3512.
- [30] Hipps, K. and G. Crosby, Applications of the photoelastic modulator to polarization spectroscopy. *Journal of Physical Chemistry*, 1979. 83(5): p. 555-562.
- [31] Barlow, A., Optical-fiber birefringence measurement using a photo-elastic modulator. *Journal of lightwave technology*, 1985. 3(1): p. 135-145.
- [32] Hansen, T.P., et al., Highly birefringent index-guiding photonic crystal fibers. *IEEE Photonics Technology Letters*, 2001. 13(6): p. 588-590.
- [33] Zeper, W.B., H.W. van Kesteren, and P.F. Carcia, Co/Pt multilayers for magneto-optical recording. *Advanced Materials*, 1991. 3(7-8): p. 397-399.
- [34] TANG, H.-j., F.-q. WU, and H.-y. DENG, Transmittance comparison of Glan-Taylor prism and Glan-Foucault prism. *Laser Technology*, 2006. 30(2): p. 215-217.
- [35] Takubo, Y., et al., Precise measurement of the extinction ratio of a polarization analyser. *Measurement Science and Technology*, 1998. 9(1): p. 20.
- [36] Wu, F., et al., Calcite/barium fluoride ultraviolet polarizing prism. *Applied optics*, 1995. 34(19): p. 3668-3670.
- [37] Bian, S., K. Xu, and J. Hong, Optical perfect shuffle using Wollaston prisms. *Applied optics*, 1991. 30(2): p. 173-174.

- [38] Hargrove, L., R.L. Fork, and M. Pollack, Locking of He–Ne laser modes induced by synchronous intracavity modulation. *Applied Physics Letters*, 1964. 5(1): p. 4-5.
- [39] Schmidt, V., *Electron spectrometry of atoms using synchrotron radiation*. Vol. 6. 2005: Cambridge University Press.
- [40] Khurshudov, A., *The Essential Guide to Computer Data Storage: From Floppy to DVD*. 2001: Prentice Hall Professional.
- [41] Oakberg, T.C., Modulated interference effects: use of photoelastic modulators with lasers. *Optical Engineering*, 1995. 34(6): p. 1545-1551.
- [42] Polnau, E. and H. Lochbihler, Origin of modulated interference effects in photoelastic modulators. *Optical Engineering*, 1996. 35(11): p. 3331-3335.
- [43] Talukder, M.A.A. and W.J. Geerts, Jones matrix description of Fabry-Perot interference in a single axis photo-elastic modulator and the consequences for the magneto-optical measurement method. *AIP Advances*, 2017. 7(8): p. 085320.
- [44] Gemeiner, P., D. Yang, and J. Canit, Multiple reflections in a photoelastic modulator: errors in polarization measurement. *Journal of Optics*, 1996. 27(5): p. 202.
- [45] Magneto-optic Kerr effect. Accessed Apr. 15, 2019. [online].
Available: https://en.wikipedia.org/wiki/Magneto-optic_Kerr_effect
- [46] Polarizing prisms. Accessed Apr. 15, 2019. [online].
Available:https://www.photonics.com/images/Web/Articles/2006/12/1/CVI_Fig3_polarizingprisms.jpg

- [47] Spectroscopic ellipsometry. Accessed Apr. 15, 2019. [online].
Available: <http://www.kristoflodewijks.be/research/theoretical-background/6-spectroscopic-ellipsometry/>
- [48] Polarization modulation with PEM for CD. Accessed Apr. 15, 2019. [online].
Available:
<http://slideplayer.com/slide/8930509/27/images/1/Polarization+Modulation+with+PEM+for+CD.jpg>
- [49] Glan-Taylor prism. Accessed Apr. 15, 2019. [online].
Available: https://en.wikipedia.org/wiki/Glan%E2%80%93Taylor_prism
- [50] Wollaston prism. Accessed Apr. 15, 2019. [online].
Available:https://www.thorlabs.com/newgrouppage9.cfm?objectgroup_id=917